NONLINEAR AND NETWORK CHARACTERIZATION OF BRAIN FUNCTION USING FUNCTIONAL MRI DATA

A Thesis
Presented to
The Academic Faculty

by

Gopikrishna Deshpande

In Partial Fulfillment
of the Requirements for the Degree
Doctor of Philosophy in the
School of Biomedical Engineering

Georgia Institute of Technology
August 2007

NONLINEAR AND NETWORK CHARACTERIZATION OF BRAIN FUNCTION USING FUNCTIONAL MRI DATA

Approved by:

Dr. Xiaoping P. Hu, Ph.D, Advisor
School of Biomedical Engineering
Georgia Institute of Technology
School of Medicine
Emory University

Dr. Marijn Brummer, Ph.D
School of Biomedical Engineering
Georgia Institute of Technology
School of Medicine
Emory University

Dr. Robert J. Butera, Ph.D
School of Biomedical Engineering
Georgia Institute of Technology
School of Electrical and Computer Engineering
Georgia Institute of Technology

Dr. Krish Sathian, M.D, Ph.D
Departments of Neurology, Psychology and Rehabilitation medicine
Emory University
Rehabilitation R&D Center for Excellence
Atlanta Veterans Affairs Medical Center

Dr. John N. Oshinski, Ph.D
School of Biomedical Engineering
Georgia Institute of Technology
School of Medicine
Emory University

Date Approved: June 20, 2007

This thesis is dedicated to my first mentors Sriranga and Vijayalakshmi, parents Narayana Dutt and Katyayini and brother Rangaprakash, all of whom have been great sources of inspiration and support in my life

ACKNOWLEDGEMENTS

I wish to express my appreciation and gratitude for many people who have helped me in the successful completion of my thesis. Firstly, I thank my advisor Dr. Xiaoping Hu for his constant guidance and encouragement throughout the course of my thesis work. I feel honored to have worked with such an exceptional scientist of the highest caliber. I will always appreciate his innate quality to inspire me to reach for goals far beyond my comprehension. I am grateful to him for his support, guidance and understanding.

I thank Dr. Stephen LaConte for the numerous discussions, practical inputs and personal encouragement whenever I encountered challenges during my research. I also thank Dr. Scott Peltier who guided me on many occasions for learning data acquisition and fMRI literature. I am very thankful to my thesis reading committee members Dr. Robert Butera, Dr. Krish Sathian, Dr. John Oshinski and Dr. Marijn Brummer for being flexible and accommodative during this entire process. I also greatly appreciate their comments, suggestions, and advisement.

I wish to express my appreciation to my colleagues Dr. Andy James, Zhi Yang, Chris Gliemi, Nader Metwalli, Roger Nana, Jaemin Shin, Dr. Tiejun Zhao, Dr. Omar Zurkiya, Dr. Dmitriy Niyazov and Randall Stilla for extending their support to my research efforts. In the same spirit, I thank Ms. Katrina Gourdet and Mr. Christopher Ruffin for their relentless help with all the administrative issues. I would also like to thank collaborators Dr. Liu, Dr. Yue and Dr. Sahgal of the Cleveland Clinic Foundation, Cleveland, OH and Dr. Kerssens, Dr. Hamman, Dr. Sebel and Dr. Byas-Smith of Emory

University. My special thanks to Dr. Krish Sathian for encouraging collaborative work and for useful insights into the world of neuroscience.

My first mentors Sriranga and Vijayalakshmi have been the greatest source of unrelenting motivation and drive to reach higher echelons in my life and I wish to express immense gratitude for that. There are no words that can describe my eternal gratitude to my parents, Dr. Narayana Dutt and Katyayini. The person I am today is because of their selfless and committed efforts to raise me in the true spirit of life. I owe every success of mine to the innumerable sacrifices that my parents have made. My brother Rangaprakash always shared the spirit of enquiry within me and provided a sense of camaraderie all along. I am highly thankful to my cousin brothers and relatives who supported my endeavors and helped me with moral encouragement during the course of my work. There are many others who have been a source of inspiration, influence, or just been there when I needed them. I wish to share this space to humbly thank them. Thank you.

This study was supported by the National Institutes of Health (NIH) grants RO1-EB002009 and Georgia Research Alliance. I also thank Whitaker Foundation for the partial support during the initial years.

TABLE OF CONTENTS

LIST OF TABLES

LIST OF FIGURES

LIST OF SYMBOLS

T	Tesla
S	Finite symbol sequence
s_n	n^{th} string
$c(n)$	Un-normalized complexity measure
$b(n)$	Asymptotic behavior of c(n) for a random string
$C(n)$	Normalized complexity measure
φ	Time delay vectors
d	Embedding dimension
τ	Embedding lag
$\vec{s}$	Position vector of a voxel
$P(n)$	Jacobians computed along phase space trajectories
β	Eigen values of phase space matrix
ε_k	Coupling parameters of CML
I	Spatial locations in a CML
$A(n)$	Prediction coefficients of MVAR
p	Order of prediction in MVAR
$E(t)$	Residual error vector
δ_{ij}	Dirac-delta function
k	Total number of ROIs in MVAR
$H(f)$	Transfer matrix of MVAR
V	Variance of the frequency domain error matrix
$S(f)$	Cross spectra
$M_{ij}(f)$	Minor obtained by removing the i^{th} row and j^{th} column from the matrix $S(f)$

$\eta_{ij}(f)$	Partial coherence
G	Sparse matrix of a graph
v	Vertex of a graph
C_{in}	Cluster-in coefficient
C_{out}	Cluster-out coefficient
$E(v)$	Eccentricity of vertex v in G
Φ, Ψ	Radial basis functions
$\{\boldsymbol{w}\}$	Prediction matrix for nonlinear Granger causality
D	Directionality Index
α	Significance value
L_o	Global distance measure in PSC calculation

LIST OF ABBREVIATIONS

fMRI	Functional magnetic resonance imaging
BOLD	Blood oxygenation level dependent
EEG	Electroencephalogram
MEG	Magnetoencephalography
ECG	Electrocardiogram
ROI	Region of interest
NMR	Nuclear magnetic resonance
MED	Minimum embedding dimension
PSC	Patterns of singularity in the complex plane
LZ	Lempel-Ziv complexity
TR	Repetition time
TE	Echo time
FOV	Field of view
T_1	Longitudinal relaxation constant
FA	Flip angle
MPRAGE	Magnetization prepared rapid gradient echo
CSF	Cerebrospinal fluid
GM	Gray matter
WM	White matter
SPM	Statistical parametric mapping
EPI	Echo planar imaging
CBF	Cerebral blood flow
CBO	Cerebral blood oxygenation

NADH	Nicotinamide adenine dinucleotide
HBO_2	Oxyhemoglobin
BNC	Bivariate nonlinear connectivity index
LM	Left motor
RM	Right motor
SMA	Supplementary motor area
F	Frontal
LC	Linear correlation
FC	Functional connectivity
ReHo	Regional homogeneity
KCC	Kendall's coefficient of concordance
ILC	Integrated linear correlation
SLLE	Spatial largest Lyapunov exponent
2D	Two dimensional
3D	Three dimensional
MNI	Montreal neurological institute
ICA	Independent component analysis
PCC	Posterior cingulate cortex
dACC	Dorsal anterior cingulate cortex
IPC	Inferior parietal cortex
FC	Frontal cortex
LPFC	Lateral prefrontal cortex
MPFC	Medial prefrontal cortex
CML	Coupled map lattice
BC	Before correcting for physiological noise

AC	After correcting for physiological noise
RBF	Radial basis function
MVC	Maximal voluntary contraction
ITI	Inter-trial interval
M1	Primary motor cortex
S1	Primary sensory cortex
PM	Premotor cortex
C	Cerebellum
P	Parietal cortex
MVAR	Multivariate autoregressive model
DTF	Directed transfer function
dDTF	Direct DTF
ANOVA	Analysis of variance

SUMMARY

Functional magnetic resonance imaging (fMRI) has emerged as the method of choice to non-invasively investigate brain function in humans. Though brain is known to act as a nonlinear system, there has not been much effort to explore the applicability of nonlinear analysis techniques to fMRI data. Also, recent trends have suggested that functional localization as a model of brain function is incomplete and efforts are being made to develop models based on networks of regions to understand brain function. Therefore this thesis attempts to introduce the twin concepts of nonlinear dynamics and network analysis into a broad spectrum of fMRI data analysis techniques.

Initially, the importance of low dimensional determinism in resting state fMRI fluctuations is explored using principles such as embedding drawn from nonlinear dynamics. The results suggest tissue-specific differences in the nonlinear determinism of gray matter and white matter. We establish that previously perceived higher random fluctuation in the gray matter can be attributed to the deterministic nonlinearity. We also show that this is not a result of higher noise level in the gray matter or the differential effect of physiological fluctuations in these tissues.

Subsequently, the concept of embedding is extended to multivariate analysis to characterize nonlinear functional connectivity in *distributed* brain networks during resting state and continuous movement. A new measure, bivariate nonlinear connectivity index, is introduced and shown to have higher sensitivity to the gray matter signal as compared to linear correlation and hence more robust to artifacts. The utility of dynamical analysis is shown in the context of investigating evolving neuronal changes.

Next, we expand the scope of functional connectivity to include directional interactions in the brain, which is termed effective connectivity. We investigate both linear and nonlinear Granger models of effective connectivity. First, we demonstrate the utility of an integrated approach involving multivariate linear Ganger causality, coarse temporal scale analysis and graph theoretic concepts to investigate the temporal dynamics of causal brain networks. Application of this approach to motor fatigue data reinforced the notion of fatigue induced reduction in network connectivity. Finally we show that the results obtained from nonlinear Granger models were akin to the linear ones. However, the nonlinear model was more robust to artifacts such as baseline drifts as compared to the linear model.

Finally, functional connectivity in *local* networks is investigated. We introduce the measure of integrated local correlation (ILC) for assessing local coherence in the brain and characterize the measure in terms of reproducibility, the effect of physiological noise, effect of neighborhood size and the dependence on image resolution. We show that ILC is independent of these parameters and hence a robust linear measure for studying local coherence in the brain. As an illustration of its neuroscientific value, we demonstrate its utility with application to anesthesia and show the importance of the default mode network, particularly the frontal areas, in mediating anesthesia-induced neural effects. In addition, ILC is shown to be higher in the default mode network at rest which decreases significantly during a task. Finally, the linear ILC approach is complemented by the nonlinear approach and we show that the concept of embedding could also be used to study connectivity in local networks.

CHAPTER 1

INTRODUCTION

In the past several decades, it has been recognized that we need very sophisticated techniques for understanding the working of a complex system such as the human brain. Advances in various disciplines such as physics, mathematics, computers and neuroscience have helped in making a substantial progress in this direction. Functional neuroimaging is an example of a successful confluence of these disciplines that has made a great impact on our understanding of the brain by drawing from physics for image acquisition, mathematics for image processing, computers for handling large amounts of data and efficient computation and finally serving the purpose of neuroscience in answering certain fundamental questions about the functional organization of the human brain.

Motivation

Among various imaging modalities, functional magnetic resonance imaging (fMRI) is becoming the method of choice owing to several advantages it offers. In fMRI, the brain is imaged over time with an MRI sequence sensitive to blood flow parameters to monitor the vascular hemodynamic response to neuronal metabolic activity (Bandettini *et al*, 1992; Kwong *et al*, 1992). The nature of the fMRI signal and its noise characteristics are not well understood and still under active research. In the past decade since its inception, research in fMRI has concentrated on characterizing event-related blood oxygenation level dependent (BOLD) response using static linear methods to

spatially localize neural substrates of brain functions (Ogawa *et al*, 1992). However, brain is a dynamically evolving system which is inherently nonlinear. Also, many functions of the brain are an emergent property of interacting functional networks and cannot be attributed wholly to discrete anatomical substrates. Hence, there is a need to develop methods that capture the nonlinearity and dynamics of evolving neuronal networks. Accordingly, this thesis will introduce novel ways of characterizing brain function in terms of nonlinear dynamics and network characteristics derived from the spatiotemporal fMRI data.

Background and Literature Review

Nonlinear Dynamics

Linear methods interpret all regular structure in a signal such as dominant frequencies and linear correlations. This underlies the assumption that the intrinsic dynamics are governed by the linear paradigm that small causes lead to small effects. However, recent advances (Sprott, 2003) have brought to light the fact that nonlinear systems can produce very complex data with purely deterministic governing equations. Therefore evidence of nonlinear dynamical determinism in a signal is an indication towards the possibility of such an underlying regime.

In practical situations, we do not have the knowledge of the governing equations of a system. In the specific case of fMRI, we only have the time evolution of observables (fMRI time series) obtained from the brain. The first problem, therefore, is to characterize the system only from observables. The second problem is that we do not know whether

the observables correspond to a single system or multiple interacting sub-systems. Even though both problems seem incredibly complicated and insurmountable, we can at least partially address those using dynamical systems theory. Chapter-2 addresses the first problem using univariate embedding and chapters 3, 4 and 5 tackle the second problem by employing multivariate embedding.

According to dynamical systems theory (Katok *et al*, 1996), the state of a system at every instant is controlled by its state variables. Thus it is important to establish a state space (or a phase space) for the system from the state variables such that specifying a point in this space specifies the state of the system and vice versa. Then we can study the dynamics of the system by studying the dynamics of the corresponding phase space points. However, what we observe in an fMRI experiment are not state variables, but only evolving scalar measurements which are the projections of the actual state variables on a lower dimensional space. The problem of converting the observations into state vectors is referred to as phase-space reconstruction and is solved using Taken's embedding theorem (Takens, 1980). Thus, it is possible to study the nonlinear dynamics of biological systems from time series derived from the system. This aspect has been exploited by researchers in deriving useful insights about biological systems by analyzing the dynamics of EEG (Pritchard *et al*, 1992; Elbert *et al*, 1995), ECG (Kobayashi *et al*, 1982; Narayanan *et al*, 1998; Fojt *et al*, 1998), heart rate variability (Guzzetti *et al*, 1996) and neuronal potentials (Butera *et al*, 1998).

In case of fMRI, it has been predominantly modeled as a linear stochastic process (Friston *et al*, 1995). However, arguments based on brain physiology indicate that the brain is likely to act as a nonlinear system that is not completely stochastic (Babloyantz,

1986; Goldberger *et al*, 1990; Elbert *et al*, 1994; Freeman, 1994). Despite the likely nonlinear nature of sources of signal fluctuations, existing methods work to a certain extent because a linear system can always approximate the behavior of a nonlinear system. Nonetheless, nonlinear approaches may be more pertinent and sensitive, and may reveal additional insights into the fMRI data. Therefore, nonlinear methods for the analysis of fMRI data have been proposed here. There have been several efforts to study the nonlinearity of BOLD response using Bayesian estimates (Friston, 2002), Volterra models (Friston *et al*, 1998), polynomial models (Birn *et al*, 2001) and Laplacian estimation (Vazquez *et al*, 1998). The nonlinear interactions between the neuronal, metabolic and hemodynamic factors giving rise to the BOLD response have also been investigated (Seth *et al*, 2004). Some nonlinear methods have been used to study activation data as well. These include delay vector variance (Gautama *et al*, 2004), multivariate nonlinear autoregressive models (Harrison *et al*, 2003), nonlinear principal component analysis (Friston *et al*, 2000) and nonlinear regression (Kruggel *et al*, 2000). However, it appears that no concerted effort has been made towards the study of nonlinear dynamics of resting-state fMRI data. Resting state time series is more complex as compared to activation time series and hence relatively difficult to characterize. Preliminary evidence suggests that nonlinear determinism in a bivariate phase space obtained from an fMRI experiment can be used as a measure of resting-state functional connectivity (LaConte *et al*, 2004). We build on this preliminary data and adopt the concept of embedding to demonstrate the utility of nonlinear methods.

Functional Connectivity

Distributed Networks

There exists a dichotomy in the organization of the human brain. On one hand, there is the modularity, which corresponds to the functional specialization of different brain regions; the investigation of this specialization has been the major focus of neurophysiological studies and functional mapping studies. A great deal of progress has been made in this regard. On the other hand, networks of regions also act together to accomplish various brain functions. Along with the rapid growth of methods and applications of functional brain mapping for localizing regions with specialized functions, there has been a great deal of interest and progress made in studying brain connectivity. In particular, neuroimaging data can be used to infer functional connectivity (Lee *et al*, 2003), which permits a systematic understanding of brain activity and allows the establishment and validation of network models of various brain functions. Thus, when studying the function of the brain, it is of great importance to examine brain connectivity, either for understanding the interplay between regions or interpreting activation patterns, and characterization of connectivity is becoming an integral part of studies of brain function.

One approach for examining connectivity, that has gained a great deal of interest, is based on the temporal correlations in functional neuroimaging data (Friston *et al*, 1993). In this vein, functional connectivity has been defined as "temporal correlations between remote neurophysiological events," while effective connectivity has been defined as reflecting "the influence one neuronal system exerts over another" (Friston *et al*, 1993). In the present work we will be examining connectivity based on the similarity

of the nonlinear dynamics of different regions of the brain. This paradigm would definitely include temporal correlations and may also provide some additional insights. Therefore an apt description of the proposed connectivity measures would be 'nonlinear dynamical connectivity'. As this is inclusive of temporal correlations, we would continue to use the term 'functional connectivity' for convenience.

Functional connectivity based on data obtained during brain activation was introduced a decade ago (Friston *et al*, 1993) and has been used to examine interaction between different areas during brain activity (Bodke *et al*, 2001; Li *et al*, 2004). These studies illustrate that examination of functional connectivity plays an important role in understanding brain imaging data and how the brain works as a concerted network.

With fMRI data acquired during resting state, low-frequency time course fluctuations were found to be temporally correlated between functionally related areas. These low frequency oscillations (<0.08 Hz) seem to be a general property of symmetric cortices and/or relevant regions and they have been shown to exist in a number of brain networks (Hampson *et al*, 2002; Biswal *et al* l, 1995, 97; Lowe *et al*, 1998; Cordes *et al*, 2000). Low frequency oscillations in vast networks have been detected with data-driven analysis approaches (Cordes *et al*, 2002; Peltier *et al*, 2003). These fluctuations agree with the concept of functional connectivity defined by Friston *et al*. While the mechanism of interregional correlation in resting state fluctuations is not well understood, this correlation may be due to strengthened synaptic connections between areas with synchronized electrical activity, in accordance with Hebb's theory (Hebb, 1949). Several recent studies have shown decreased low frequency correlations for patients in pathological states, including cocaine use (Li *et al*, 2000), cerebral lesions (Quigley *et al*,

2001), Tourette syndrome (Biswal *et al*, 1998), multiple sclerosis (Lowe *et al*, 2002) and Alzheimer's disease (Li *et al*, 2002). Thus, low frequency functional connectivity provides an important characterization of the brain.

To date, functional connectivity has been mostly characterized by linear correlations, which may not provide a complete description of the temporal properties of fMRI data. In addition, the linear correlation approach is very sensitive to variations unrelated to functional connectivity, including subject motion, baseline drifts, respiration and heart beat, and paradigm driven modulations. For an alternative, and perhaps complementary, approach, we resort to nonlinear dynamics. The intuitive appeal of the applicability of nonlinear dynamics, its success in characterizing various biological time series and the literature related to attempts by researchers to model the nonlinearity in BOLD response and activation data have been elaborated in the previous section. The literature on the application of nonlinear dynamics to measure connectivity is scanty. Preliminary evidence regarding the possibility of using determinism in a bivariate phase space reconstructed from fMRI time series as a marker of functional connectivity has been reported recently (LaConte *et al*, 2003). However, it appears that there has not been an attempt to fully utilize the potential of nonlinear dynamics to study connectivity using fMRI data. We attempt to unravel this potential in the current study using multivariate embedding for assessing nonlinear functional connectivity. This concept has been successfully applied to model multivariate meteorological data (Stewart, 1996). In the biological context, the idea of multivariate embedding was mooted a decade ago for application to EEG (Babloyantz, 1989; Freeman, 1989; Abraham, 1993). Complexity and predictability indices calculated from a multivariate embedding of cardio-respiratory data

have been used to infer nonlinear couplings between cardiac and respiratory rhythms (Hoyer *et al*, 1998ab). Given the success of the multivariate embedding concept in other contexts, it is encouraging to explore its applicability in the emerging field of fMRI functional connectivity.

Local Networks

While most of the functional connectivity studies focus on distributed networks in the brain, we also investigate local networks in addition to distributed networks. Coherence in local functional networks arises due to coordination among neighboring neuronal units and is dependent on the local anatomic structure and homogeneity of neuronal processes. This is a fairly new concept in the field of functional neuroimaging introduced recently by Zang *et al* (Zang *et al*, 2004) in the context of activation data. However, the methodology adopted by them to measure local coherence using Kendall's coefficient of concordance has limited applicability due to its dependence on imaging parameters and the size of the neighborhood in which the coherence is computed. In this work, we investigate these aspects and introduce a novel approach based on the spatial correlation function to overcome the above limitations. Also, the method is extended to the nonlinear case using multivariate spatial embedding in the local neighborhood for characterizing nonlinear local coherence.

Effective Connectivity

Functional connectivity only provides information about correlations in fluctuations, but is not informative about the directions of influence between interacting

regions of a neural network. Effective connectivity, defined as the influence one neuronal system exerts over another (Friston *et al*, 1993), attempts to bridge this gap by defining explicit models of directed interactions. Structural equation modeling (Buchel *et al*, 1997; McIntosh *et al*, 1994), nonlinear system identification techniques (Friston *et al*, 2000), Bayesian estimation of deterministic state-space models (dynamic causal models) (Friston *et al*, 2003) have been used to infer effective connectivity. Although these models have their advantages and disadvantages, none of them incorporate information on temporal precedence (the assignment of cause and effect), which is central to the concept of causality. Also, these techniques require an *a priori* specification of an anatomical network model and are therefore best suited to making inferences on a limited number of possible networks. Recently an exploratory structural equation model approach was described (Zhuang *et al*, 2005) that does not require prior specification of a model. However with increasing number of regions of interest, its computational complexity becomes intractable and the numerical procedure becomes less stable. These disadvantages can largely be circumvented by methods such as Granger's causality which are based on the cross-prediction between two time series (Granger, 1969). It is based on the assumption that a causal relation between two time series improves the prediction of one time series from the other. Such a formulation was supported by Weiner (Weiner, 1956). Weiner's proposal was formalized in the context of linear regression models of stochastic processes by Granger (Granger, 1969).

However, adoption of Granger causality to fMRI data is not straightforward. The spatial variability of the sluggish hemodynamic response has the potential to confound the results. Also, interpreting a large number of directed interactions obtained from a

neural network involving a large number of ROIs is challenging. These issues are addressed in this work and an integrated framework combining multivariate Granger causality analysis, temporal down-sampling of fMRI time series and graph theoretic concepts is proposed in chapter 4.

Conceptually, the extension of Granger causality to the nonlinear case could be accomplished by performing nonlinear prediction instead of linear prediction. Nonlinear prediction in the multidimensional embedded space using locally linear models (Chen *et al*, 2004) and radial basis functions (Ancona *et al*, 2004) have been validated using numerical simulations. In this work, we have adopted the radial basis function approach since it is more robust for short and noisy time series such as fMRI.

The Approach

From the previous section, it is evident that since its inception a decade ago, functional neuroimaging has mostly been limited to linear functional mapping studies to localize brain function to distinct anatomical substrates. We also reasoned out that based on preliminary evidence and intuitive arguments, nonlinear dynamic and network models of brain function are more appropriate. Accordingly, our approach will be to synthesize nonlinear dynamics and network analysis to develop novel models of brain function. We begin with a purely univariate nonlinear dynamic analysis of resting state fMRI data in healthy humans. Subsequently, both linear and nonlinear multivariate functional connectivity is investigated in undirected distributed networks in the cortex following which, directed causal network models are derived based on linear and nonlinear Granger causality. Finally, connectivity is investigated in local networks. This progression covers

a broad spectrum of analysis techniques currently employed by researchers to infer brain function based on fMRI as shown in Fig.1.1.

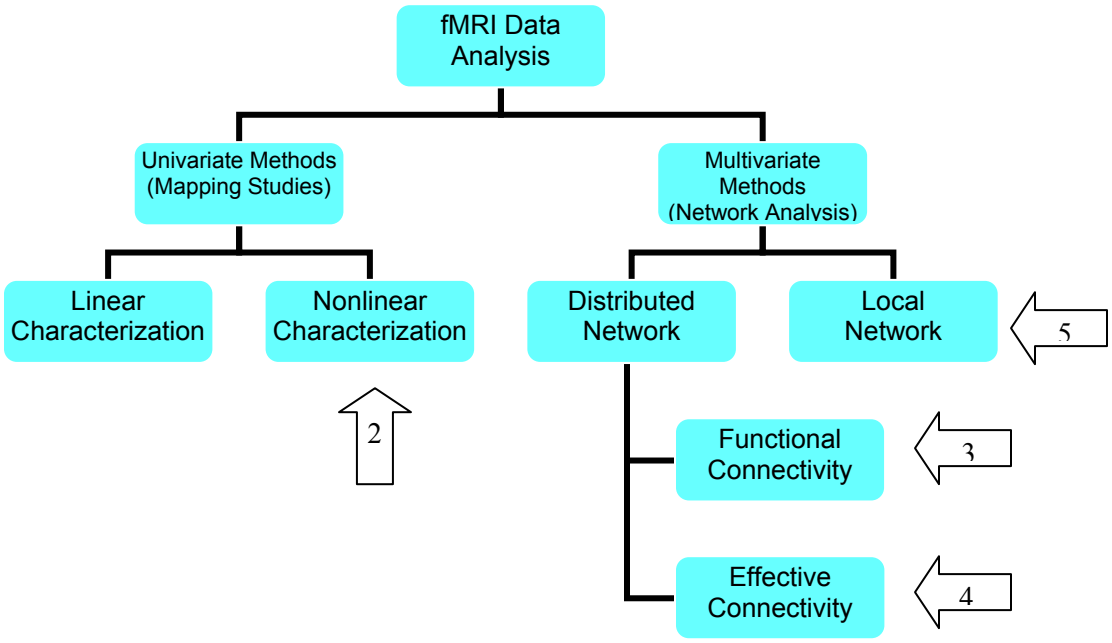

Figure 1.1 The spectrum of fMRI data analysis techniques covered in this thesis. The arrows 2 to 5 indicate the four topics covered in chapters 2 to 5

Thesis Organization

This thesis is organized based on the twin themes of nonlinear dynamics and network analysis and resembles the actual progression of research during the course of this investigation. These themes are reflected in all the chapters but occur in different contexts for characterizing brain function. The basis for this organization is to cover a broad spectrum of analysis techniques prevalent in neuroimaging, further complementing and improving the existing methods by infusing the concepts of nonlinear dynamics and network analysis. Various types of fMRI data sets have been used in different chapters to illustrate the utility of the methods. The objective is to illustrate the methods using

examples and the results reveal interesting neuroscientific findings which are also discussed briefly in the corresponding chapters.

With this framework, the thesis is organized into four main chapters. The second chapter introduces the basic concepts of nonlinear dynamics in the context of univariate analysis to investigate the origin of tissue specific differences in resting state fluctuations in fMRI data. This chapter dwells on the importance of low dimensional determinism in the data as inferred through the concepts of embedding and information theory.

Chapters 3, 4 and 5 describe a synthesis of network analysis and nonlinear dynamics to investigate different types of brain networks. While we compare and contrast the linear and nonlinear approaches, we also introduce novel concepts and significant improvements into the prevalent linear methodology. Though the concept of embedding is introduced in the univariate context in the second chapter, it is extended to the bivariate context to investigate nonlinear functional connectivity in *distributed* brain networks in the third chapter. In addition, we investigate the sensitivity of the nonlinear approach to the desired gray matter signal as compared to the linear approach.

In the fourth chapter we address the question of effective connectivity in distributed brain networks. This is the state of the art as far as network analysis is concerned because it enables us to construct models of directed interactions between brain regions in contrast to functional connectivity where the direction cannot be inferred. An integrated linear approach is introduced which combines the concepts of multivariate Granger causality, coarse temporal analysis and graph theory to investigate brain networks and their dynamics. Application of this concept to motor fatigue is discussed and the viability of existing hypotheses about fatigue is examined. Subsequently, the

Granger model is extended to the nonlinear case using the concept of embedding. The nonlinear model is compared with the linear one and is shown to be more robust in the presence of artifacts such as baseline drifts.

In the fifth chapter we investigate connectivity in *local* brain networks. This is an area that has received less attention in the literature as compared to distributed networks. We introduce a very robust technique to measure local coherence in the brain using the linear spatial correlation function. As an illustration, we demonstrate its utility with application to anesthesia and show the importance of the default mode network, particularly the frontal areas, in mediating anesthesia-induced loss and recovery of consciousness. The concept of embedding which is utilized in the third chapter for investigating distributed networks is modified so as to investigate local networks in the fifth chapter. This provides a complementary approach to the robust linear measure introduced earlier in the chapter. Finally, the sixth chapter concludes the findings of this thesis.

Scope of the Thesis

It is presumed that the reader is familiar with the physical principles of fMRI data acquisition as well as basic concepts of signal and image processing concerning fMRI data analysis. Also, we have assumed preliminary knowledge of neuroscience while describing the neuroscientific findings in this thesis. An effort has been made to present the findings as concisely as possible.

CHAPTER 2

TISSUE SPECIFICITY OF NONLINEAR DYNAMICS IN BASELINE fMRI

Introduction

It is very well understood that fluctuations in fMRI data cannot be fully attributed to NMR noise (Kruger *et al*, 2001) and that the noise structure of the fMRI data may provide insights into the brain. In particular, fluctuations at very low frequencies (<0.1 Hz) in fMRI data are spatially correlated within networks corresponding to related brain functions. This low frequency correlation has been utilized in the study of functional connectivity (Biswal *et al*, 1995; Lowe *et al*, 1998) and has been shown to reflect pathological and/or physiological alterations (Quigley *et al*, 2001; Li *et al*, 2002). The resting state (absence of explicit brain activation) is important because it conveys valuable information on basal neural activity. In addition, while we do not focus on a specific brain network here, these data have received increased attention with respect to diagnostic utility (Quigley *et al*, 2001; Li *et al*, 2002) and with proposed theories of the default mode of brain function (Raichle *et al*, 2001).

The neuroscience community has learned a lot about the spatio-temporal nature of brain function through functional connectivity studies using various statistical approaches, including linear correlations between spatial regions (Biswal *et al*, 1995; Lowe *et al*, 1998, Peltier *et al*, 2002), and data driven techniques such as principal component analysis (Strother *et al*, 1995) and self organizing maps (Peltier *et al*, 2003). However, there is still great potential for building this knowledge base with alternative approaches. Linear statistical methods make an underlying assumption that the signals are

produced by a linear stochastic system. Arguments based on brain physiology, however, suggest that the brain is likely to act as a nonlinear system that is not completely stochastic (Elbert *et al*, 1994; Schiff *et al*, 1994; Babloyantz *et al*, 1986; Freeman *et al*, 1994) and the processes generating fMRI data are expected to be nonlinear. Although existing linear methods work to a certain extent because a linear system can always approximate the behavior of a nonlinear system, nonlinear approaches may be more pertinent and sensitive, revealing additional insights into the fMRI data. Therefore, nonlinear methods for the analysis of fMRI data have been investigated in this work. Even though there has been an effort to study the nonlinearity of the BOLD response to explicit tasks (Vazquez *et al*, 1998; Friston *et al*, 1998; Birn *et al*, 2001), very little work has been done in applying methods of nonlinear dynamics to fMRI, particularly during the resting state. Building upon our preliminary study (LaConte *et al*, 2003, 2004) we focus here on a systematic study of the tissue specific properties of nonlinear dynamics in fMRI resting state data.

In addition to possibly revealing interesting patterns in the resting state brain dynamics, nonlinear analysis may allow us to better characterize biological sources of noise in the MRI signal. Kruger *et al* reported higher random fluctuations in the gray matter (Kruger *et al*, 2001); this may be due to deterministic nonlinearity of the signal produced by an underlying finite dimensional system. If the driving sources of these fluctuations are of nonlinear origin, they should also be revealed with nonlinear analysis techniques. Further, an enhanced ability to characterize the biological noise may allow us to reduce its effect on activation detection.

As described in the following sections, the present work examines several aspects of nonlinear dynamics. We start by reconstructing the state space of the system and finding a finite minimum embedding dimension (MED) of the underlying system. The nonlinearity arising from the finite dimensional dynamics are then characterized using patterns of singularities in the complex plane (PSC). However, the nonlinearity may arise either due to stochastic or deterministic dynamics. We thus evaluate the determinism in the dynamics to make this distinction. A finite embedding dimension is a measure of the determinism of the system, which can be quantified using information theoretic measures like Lempel-Ziv complexity. It is widely recognized by many that physiological noise due to respiration and cardiac pulsation can be a significant contribution to the signal fluctuation in fMRI (Kruger *et al*, 2001, Hu *et al*, 1995). Therefore, it is also of interest to study their contribution to the nonlinear dynamics in the fMRI signal. A minor aspect of the present work looks at this effect by applying the nonlinear analysis to data before and after physiological noise correction. Our approach, then, is to obtain a comprehensive understanding of resting state fMRI by estimating the appropriate embedding dimension and subsequently characterizing the system dynamics using nonlinearity and determinism.

Theory

Linear methods can capture structures in a signal such as dominant frequencies and linear correlations. This relies on the assumption that the intrinsic dynamics are governed by the linear paradigm that small causes lead to small effects. Since the possible solutions of linear equations are either exponential or periodic oscillation, the

irregular structure in the signal has to be attributed to some random external input to the system producing the signal. However, recent advances in chaos theory have brought to light the fact that a random input is not the only possible source of irregularity in a system's output. Nonlinear chaotic systems can produce very irregular data with purely deterministic governing equations. One way to evaluate whether a system is deterministic or random is to estimate the minimum embedding dimension (MED) (Grassberger *et al*, 1983; Broomhead *et al*, 1986; Mees *et al*, 1987; Theiler *et al*, 1987; Kennel *et al*, 1992; Tsonis *et al*, 1992; Cao, 1997), which is the number of independent state variables contributing to the irregular dynamics of a signal like fMRI time series (please refer Appendix A for details about calculation of MED). Once the finite dimensionality of a system has been established through MED, it is possible to characterize the nonlinearity and determinism using methods described below.

Pattern of singularities in the complex plane (PSC) algorithm

It has been found that the distribution of singularities in the complex plane is critical for determining the behavior of a dynamical system at any arbitrary time. From numerical investigations of the Lorenz equations (Tabor *et al*, 1981), it was demonstrated that when the system is in a periodic regime (limit cycle) the arrangement of singularities (poles) reflects the corresponding periodicity of the real-time solution. As the dynamical regime transitions toward the chaotic one, the corresponding arrangement of singularities becomes very irregular. From these results, Di Garbo and colleagues (Di Garbo *et al*, 1998) suggested an algorithm (the PSC algorithm) to evaluate the nonlinear structure in a time series. The method determines a measure of significance, using a null hypothesis

that the time series under investigation arises from a linear process. The null hypothesis is rejected if the value of this significance is greater than a threshold (say, 95% confidence level). The significance value can be further used as a quantifier to assess deviation from linearity. The larger its value the more nonlinear is the time series (please refer Appendix B for details of PSC algorithm).

Since the PSC algorithm looks for only the nonlinear signal structure, it cannot be concluded from this measure alone whether the nonlinearity is due to deterministic dynamics or stochastic dynamics. To answer this question, Lempel-Ziv complexity measure is considered.

Lempel-Ziv complexity measure algorithm

The Lempel-Ziv complexity measure (LZ) is a unique way of looking at the structure of the signal (Zhang *et al*, 1999). The signal must first be transformed into a finite symbol sequence *S.* If we have a string $s_1,s_2,\ldots,s_n$, then *c(n),* which is the number of different sub-strings of $s_1,s_2,\ldots,s_n$, is the measure of complexity. It reflects the rate of new patterns arising with increasing sequence length, *n*. Thus by simple operations of comparison and accumulation, the computation of *c(n)* is achieved. In this work, we have used the normalized complexity measure *C(n)* which is the ratio of *c(n)* to *b(n)*, where *b(n)* gives the asymptotic behavior of *c(n)* for a random string. LZ is zero for a fully deterministic signal and one for a totally random signal. Hence LZ indicates the degree of determinism in the signal. (Please refer Appendix C for details of LZ algorithm).

Methods

MRI Data Acquisition and Analysis

Data acquisition consisted of imaging three normal, healthy human subjects in resting state using a single-shot BOLD-contrast gradient EPI sequence at 3T Siemens Trio (repetition time (TR)=750 ms, echo time (TE)=34 ms, flip angle=50 deg and field of view (FOV)=22cm, with 5 contiguous axial slices covering the region from the top of the head to the top of the corpus collosum, 5mm slice thickness, 1120 volumes (time points) per slice and 64 phase and frequency encoding steps). Two additional volunteers were scanned using the same parameters as above, but with 10 saggital (rather than axial) slices containing the ventricles. High resolution (512×512) T_1-weighted axial anatomical images were acquired in the first scanning session. In the second session, anatomical images with 1 mm isotropic resolution were acquired using a magnetization prepared rapid gradient echo (MPRAGE) sequence (Mugler *et al*, 1990) (TR/TE/FA of 2600 ms/3.93 ms/8 deg).

For the anatomical data from the first session, the images were segmented using a procedure involving manual removal of the extra-cranial signal and segmentation of gray and white matter based on their intensity. The resulting segmented images were down-sampled by a factor of 8 to obtain a 64×64 mask of gray matter and white matter. The MPRAGE images in the second experiment were segmented into gray matter, white matter and cerebrospinal fluid (CSF) using SPM2 (Wellcome Department of Cognitive Neurology, London, UK; http://www.fil.ion.ucl.ac.uk). Since SPM2 segments the images in the normalized space, the resulting masks were transformed back into the original

image space, resliced to match the location of the EPI data and thresholded to obtain binary masks of the three tissue types. The resulting masks were similarly down sampled to the resolution of the EPI images.

A physiological monitoring unit consisting of a pulse-oximeter and nasal respiratory canula was used during data acquisition to record cardiac and respiratory pulsations, respectively. These physiological fluctuations were corrected for in the functional data retrospectively (Hu *et al*, 1995). Both physiologically corrected and uncorrected data were analyzed and compared.

Nonlinear Dynamical Analysis

The strategy employed for the application of the nonlinear dynamical methods is outlined below. A MATLAB program was developed and utilized for all the analysis described below. The MED of baseline fMRI was first calculated using the modified false nearest neighbor approach (Cao, 1997). A low finite value of MED was obtained, which provided a justification for the characterization of nonlinearity using PSC. A high value of nonlinearity in resting-state fMRI prompted us to investigate the source of this nonlinearity (deterministic or stochastic) by employing the information-theoretic measure, LZ. The PSC and LZ values were calculated for each voxel in all the axial slices for subjects 1, 2 and 3 and all saggital slices for subjects 4 and 5. The mean values of the nonlinear measures for each tissue type were obtained and tabulated. Since the resultant parameters for each tissue type was not normally distributed, the statistical significance of the tissue difference of each measure was assessed using the nonparametric Wilcoxon rank sum test (Wilcoxon, 1945). Also, PSC and LZ values were used to generate

summary images for visualization. These strategies enabled us to characterize baseline fMRI dynamics using deterministic nonlinearity.

Results and Discussion

The MED values were calculated by reconstructing the attractor for each voxel time series in all the slices as outlined in the previous section. The mean MED for gray matter, white matter and CSF was found to be 10.55 ± 0.97, 10.89 ± 0.96 and 9.6 ± 1.12 respectively, which indicated that the difference in means was not significant and hence the embedding dimension was not tissue-specific. Since MED is an integer number, we rounded off the value to 10. The MED results suggest that a finite number of state variables describe the baseline fMRI dynamics and thus provide a justification for the quantification of nonlinearity using the PSC measure. We have calculated the PSC measure from simulated signals and various biological time series - cardiac and respiratory data obtained from the physiological monitoring unit during our fMRI data acquisition, EEG signal obtained from MIT-BIH data base, and the fMRI data from the present study. Normally distributed random numbers were generated to emulate signals of a linear stochastic process and a sinusoidal signal was used as an example of a deterministic signal. Both types of signal had the same number of time points as the experimental time series (1120 points). Table 2.1 lists the PSC for the various types of signals described above with and without the addition of 10 dB Gaussian noise. The high value of PSC for fMRI data confirms the nonlinear structure in the signal. The results also indicate that PSC is fairly robust to random noise.

Table 2.1 Typical values of the PSC nonlinearity index for simulated and commonly occurring physiological signals

Type of signal		Typical PSC Nonlinearity Score	
		Without Noise	With Noise
Linear Stochastic Process		2	5
Deterministic function		6	8
Respiration		26-60	30-70
EKG		10-30	17-35
EEG	Background	175	182
	Alpha activity	1500	1549
Baseline fMRI		400-2000	420-2017

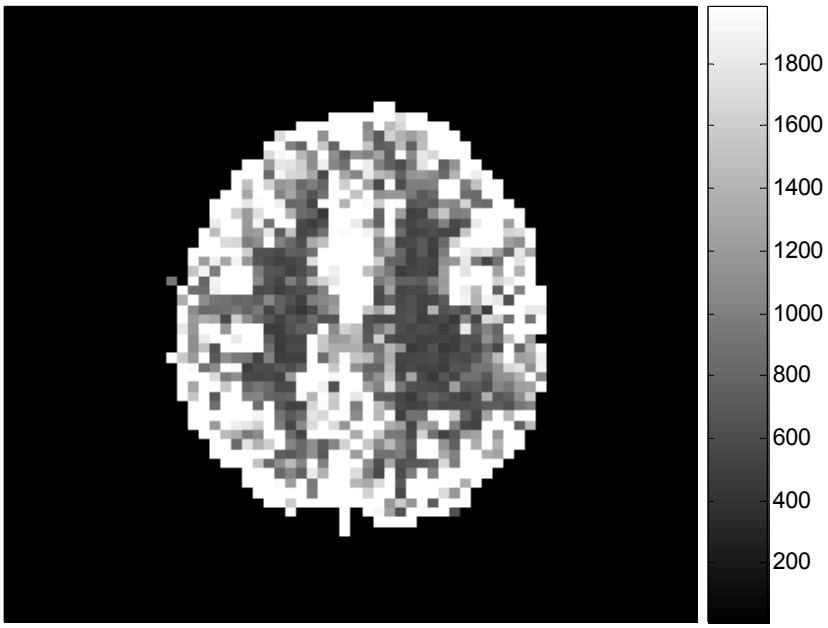

Figure 2.1 PSC map for an axial slice from subject 3

Fig. 2.1 above shows the PSC map of an axial slice of the human cortex for subject 3. It may be observed from the figure that there is more nonlinearity in gray matter than white matter. This conclusion is quantitatively validated by the mean PSC values given for white, gray matter and CSF in Table 2.2. Statistically there is a highly significant difference in the PSC values between the three tissue types with gray matter showing significantly higher nonlinearity than white matter and CSF. As previously mentioned, the study by Kruger *et al* (Kruger *et al*, 2001) has shown that gray matter exhibits more random fluctuations compared to white matter. Our PSC results indicate nonlinear signal structure, but do not reveal whether the nonlinearity arises from deterministic dynamics or stochastic dynamics. The LZ results can be used to answer this question. Fig. 2.2 shows the LZ map for an axial slice from subject 3. Table 2.3 shows the mean values of LZ for all three tissues types. Since the values of LZ are less than one, there is evidence of determinism. Lower values for gray matter indicate higher determinism compared to white matter and CSF. Even though there is heterogeneity of PSC and LZ within a tissue type, the p-values from Wilcoxon sum rank test showed that their distributions are significantly different for the three tissues.

Table 2.2 PSC values for gray matter, white matter and CSF

PSC	Gray Matter	White Matter	CSF	Wilcoxon Sum Rank Test: p-value		
				GM-WM	GM-CSF	WM-CSF
Subject 1	765	457	-	8.68×10^{-12}	-	-
Subject 2	1065	634	-	2.39×10^{-12}	-	-
Subject 3	1080	645	-	0	-	-
Subject 4	962	716	841	6.9×10^{-5}	1.5×10^{-5}	4.8×10^{-4}
Subject 5	940	771	618	3.1×10^{-5}	3.2×10^{-4}	3.1×10^{-5}

Figure 2.2 1-LZ map for an axial slice from subject 3

Table 2.3 LZ values for gray matter, white matter and CSF

LZ	Gray Matter	White Matter	CSF	Wilcoxon Sum Rank Test: p-value		
				GM-WM	GM-CSF	WM-CSF
Subject 1	0.82	0.91	-	2.28×10^{-12}	-	-
Subject 2	0.60	0.72	-	3.05×10^{-7}	-	-
Subject 3	0.64	0.82	-	3.89×10^{-25}	-	-
Subject 4	0.56	0.69	0.75	2.5×10^{-6}	8.9×10^{-4}	8.5×10^{-7}
Subject 5	0.65	0.70	0.73	3.7×10^{-4}	2.2×10^{-3}	5.3×10^{-5}

The inter-subject variability in the values can be attributed to the fact that the 'resting state' or 'baseline' is not a well-defined state and can be highly variable from subject to subject. Also, we can see from Tables 2.2 and 2.3 that gray matter exhibits higher nonlinear determinism than white matter at a statistically significant level. This

tissue specificity can be attributed both to the differences in fMRI physiology and neural processing. The BOLD contrast in fMRI is a result of interactions between cerebral blood flow (CBF) and cerebral blood oxygenation (CBO). It has been shown that CBF fluctuations result in CBO fluctuations (Obrig *et al*, 2000). There are several arguments for and against blood pressure (Giller *et al*, 1999) and vasomotion (Hudetz *et al*, 1998) as being the source of fluctuations in CBF. Native fluctuations in CBF arising from fluctuations in nicotinamide adenine dinucleotide (NADH) and oxyhemoglobin (HBO_2) can be attributed to such fluctuations in cortical metabolism and neuronal activity (Elwell et al, 1999). These give rise to a complex interplay of various factors that result in baseline fMRI signal fluctuations. The regional differences in the interplay between these factors are likely to give rise to the differences in fMRI signal fluctuations from different tissues structures. These signal differences have been characterized numerically in this study using nonlinear analysis. This complements previous studies that have indicated that there is non-uniform determinism across activities (Dhamala *et al*, 2002) in the brain. Interestingly, our results seem to indicate that there is non-uniform determinism across different regions of the brain as well.

An important fact to consider is the effect of removal of physiological noise on the results. To investigate the spatial extent of the effect of correction, we plotted the difference images (original - corrected) of the PSC and LZ parameters. Fig. 2.3(a) and Fig. 2.3(b) show the PSC and LZ difference images, respectively, for an axial slice. For comparison, Fig. 2.3(c) illustrates the percentage reduction in signal variance after correction in the same axial slice. It can be seen that a greater amount of noise is removed in gray matter and CSF than in white matter, indicating higher physiological noise in

them. This observation is consistent with higher noise in gray matter compared to white matter reported by Kruger *et al* (Kruger *et al*, 2001), attributed to possible differences in blood volume and perfusion in those tissues. By carrying out the analysis on physiological noise-corrected data, we have accounted for the differences in fMRI noise characteristics arising from cardiac and respiratory pulsations. The similarity between Fig. 2.3(a), Fig. 2.3(b) and Fig. 2.3(c) indicates that the nonlinearity and determinism contributed by the physiological rhythms is mostly removed by retrospective correction.

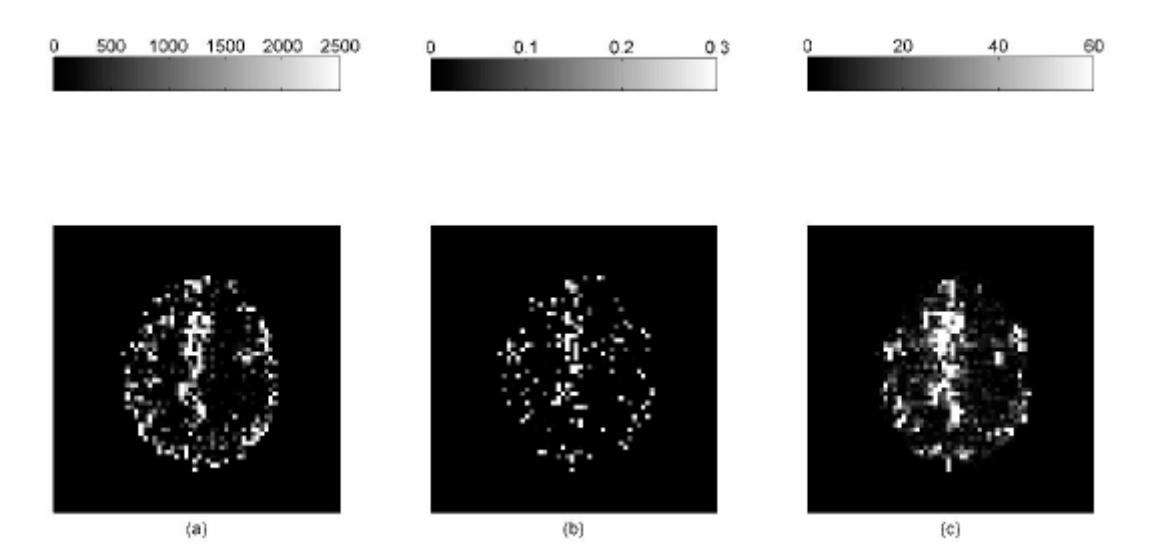

Figure 2.3(a) PSC difference map (original value- corrected value) for an axial slice. **(b)** LZ difference map for the same slice. **(c)** Percentage reduction in fMRI time course variance after physiological correction for the same slice

To test if the difference in noise level between gray matter and white matter as reported by Kruger (Kruger *et al*, 2001) is a major cause of the observed gray-white difference in nonlinear determinism, Gaussian random noise was added to white matter time courses to match their standard deviation to that of gray matter time series, and PSC

and LZ were calculated on these synthetic white matter time courses. From the results shown in Table 2.4, the PSC for the synthetic white matter time courses, although slightly increased, is still much less than that of gray matter shown in Table 2.2. This is consistent with the notion that Gaussian noise is a linear process and is not expected to increase the nonlinearity significantly. In Table 2.4, the noise addition slightly increases the LZ, as expected since the addition of random noise decreases determinism (and hence increases LZ), moving the LZ of synthetic white matter time courses further away from that of gray matter. Given these observations, it is unlikely that the increased noise level in gray matter is a major cause for the tissue specificity of deterministic nonlinearity.

Table 2.4 White matter PSC and LZ obtained before and after the addition of white Gaussian noise to match the noise variance of gray matter time courses.

Sub	Before Noise Addition		After Noise Addition	
	PSC	LZ	PSC	LZ
1	457	0.91	481	0.98
2	634	0.72	684	0.90
3	645	0.82	676	0.98
4	716	0.69	737	0.82
5	771	0.70	789	0.84

To ascertain the nonlinear determinism of the CSF, we carried out a similar analysis on saggital slices, including an ROI on ventricles. Fig. 2.4(a), Fig. 2.4(b) and Fig. 2.4(c) illustrate the PSC and LZ difference images and percentage reduction in fMRI signal variance due to correction, respectively, for a representative saggital slice containing the ventricles. It is well known that CSF has higher physiological noise compared to gray matter and white matter (Kruger *et al*, 2001). This notion is confirmed in Fig. 2.4(c) which shows greater noise reduction in the ventricles compared to the

cortical gray/white matter, leading to greater differences in PSC and LZ values of CSF before and after correction. In particular, we found that the raw CSF pulsation, which contains the B-waves (Auer *et al*, 1983), is highly nonlinear. Retrospective correction substantially decreased the variance in CSF time courses as well its nonlinearity and determinism. In contrast, the decrease in nonlinearity and determinism in gray and white matter after correction was insignificant compared to that of CSF. It is worth noting that physiological correction only scaled down the nonlinearity and determinism, preserving its tissue specificity. Therefore, the tissue specificity of deterministic nonlinearity we report is unlikely to arise solely from cardiac and respiration effects. Rather, fMRI physiology and the nature of neural processing (reflected by the native fluctuations) vary across tissues, giving rise to the tissue-specific nature of the baseline signal.

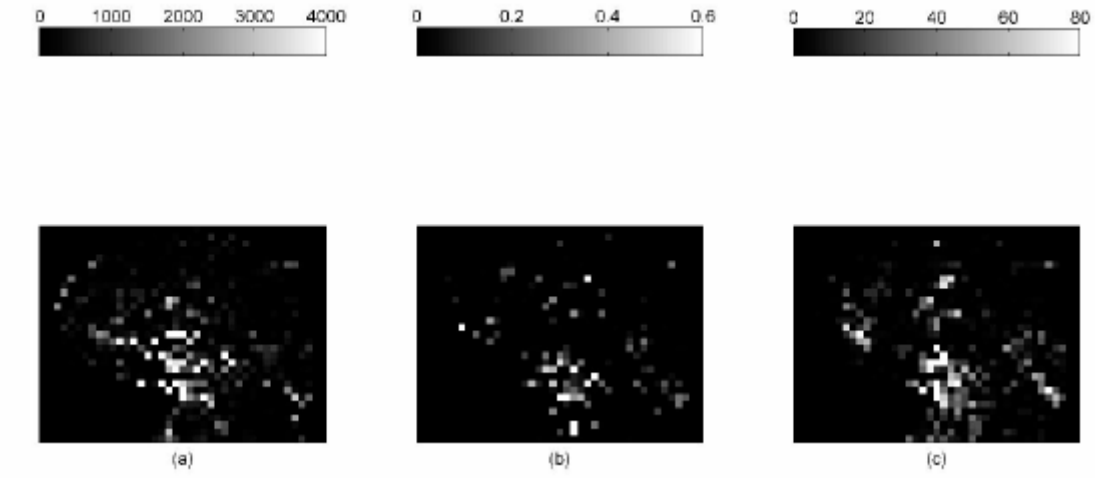

Figure 2.4(a) PSC difference map (original value- corrected value) for a saggital slice. **(b)** LZ difference map for the same slice. **(c)** Percentage reduction in fMRI time course variance after physiological correction for the same slice

Conclusions

This study approaches the processing of fMRI data from a nonlinear dynamical perspective. We have shown that fMRI time courses are not produced by a purely

stochastic system, and hence have used various nonlinear techniques to obtain a new perspective into the underlying system dynamics. The results from the above techniques show that brain dynamics can be neither characterized by a purely stochastic nor a fully deterministic system. On the contrary, the underlying dynamics seems to be deterministic, produced by a system having roughly 10 state variables, exhibiting non-uniform determinism among the different regions of the brain, with gray matter showing more determinism than white matter and CSF. What was previously perceived as higher random fluctuation in the gray matter is actually due to the deterministic nonlinearity of the signal produced by an underlying nonlinear dynamical system. We found that the nonlinearity exhibits tissue specificity even after the removal of physiological fluctuations. The possibility of higher noise level in gray matter as a main reason for tissue-specificity of deterministic nonlinearity was examined and ruled out. Therefore, higher nonlinear determinism in gray matter is not due to cardiac/respiratory effects or noise intensity differences, but can potentially be attributed to local differences in fMRI physiology and neural processing.

CHAPTER 3

FUNCTIONAL CONNECTIVITY IN DISTRIBUTED NETWORKS

Introduction

Primarily, functional connectivity has been characterized by linear models, which may not provide a complete description of its temporal properties. In this work, we broaden the measure of functional connectivity to study not only linear correlations, but also more general deterministic coupling arising from both linear and non-linear dynamics. It is encouraging to note that the field of nonlinear dynamics has been successfully applied to characterize many biological signals such as EEG, ECG, and respiratory movement (Pritchard *et al*, 1992; Narayanan *et al*, 1998; Fojt *et al*, 1998; Elbert *et al*, 1995; Kobayashi *et al*, 1982; Hoyer *et al*, 1998a). These studies investigate low dimensional chaotic behavior in distinction from a stochastic model. This is achieved by characterizing the system in terms of predictability or invariant features (e.g., correlation dimension) (Kaplan, 1994). These methods reconstruct the dynamics of the system from observables acquired from the system (such as time series). In the context of fMRI, which is relatively short and noisy time series, such approaches are particularly challenging. Furthermore, the computational load of these studies, the number of algorithmic free parameters and the large quantity of spatial locations make the application of traditional measures such as correlation dimension extremely challenging.

In this chapter we introduce a simpler and intuitively appealing nonlinear dynamical technique to characterize functional connectivity using short and noisy fMRI data. We do so by adapting the concept of multivariate phase space reconstruction (also

referred to as multivariate embedding) as proposed by Cao (Cao *et al*, 1998). This method relies on reconstructing the joint dynamics of two different time series and comparing the resulting joint embedding dimension with that of individual embedding dimensions. Accordingly, if the time course of a candidate voxel provides additional information concerning the time evolution of a reference voxel time series, the joint dimension will be lesser than the sum of the individual dimensions.

As an illustration, we have applied our method to both resting-state and continuous motor task data. Resting-state functional networks have been an area of extensive research of late considering the fact that several such networks in the brain have been identified (Hampson *et al*, 2002; Biswal *et al*, 1995, 97; Lowe *et al*, 1998; Cordes *et al*, 2000). Also, these networks are altered during pathological states (Li *et al*, 2000, 2002; Quigley *et al*, 2001; Biswal *et al*, 1998; Lowe *et al*, 2002), hinting at the importance of these networks. Interestingly, there seems to be a concordance between connectivity identified from baseline data and that identified from data acquired during a continuous task (Hampson *et al*, 2002). Therefore it is believed that the task only modulates a common underlying network which is also identified during resting state (Morgan *et al*, 2004).

A major confound in ascertaining functional connectivity is the presence of systematic noise in the fMRI signal, which can obscure the detection of the spatio-temporal patterns in functional imaging data. Possible sources include (but are not limited to) signal drifts (Bandettini *et al*, 1993), physiological noise due to the respiratory and cardiac rhythms (Hu *et al*, 1995, Biswal *et al*, 1996), statistical outliers in the time courses of the k-space data (Fitzgerald, 1996) and subject head motion (Lauzon *et al*,

1993; Hajnal *et al*, 1994; Eddy *et al*, 1996; Maas *et al*, 1997; Woods *et al*, 1998). Eliminating the effects of these noise sources is an important step in investigating functional connectivity. In detecting functional connectivity from baseline data, although some have used a repetition rate (TR) above 2 s (Lowe *et al*, 1998), most studies have employed sub-second TRs in order to permit the removal of cardiac and physiological noise via filtering, thus severely hampering the coverage of the whole brain. By regression to respiration and cardiac pulsations, studies (Rambouts *et al*, 2003) have shown that the effect of physiological noise can be significant in functional connectivity analysis. Their attempt to remove the physiological noise was limited by the use of a simple regression and by working in the image domain. However, the effects of physiological noise are better characterized and removed in the k-space based on retrospective fitting, prediction and subtraction of physiological perturbation (Hu *et al*, 1995). In this work, we have performed the above procedure before functional connectivity analysis.

Methods

According to dynamical systems theory (Katok *et al*, 1996), the state of a system at every instant is controlled by its state variables, and the vector space of its state variables specifies the dynamics of the system. Therefore, the dynamics of a system can be studied by studying the dynamics of its phase space. However, the data measured in an fMRI experiment are not state variables, but only evolving scalar measurements which are the projections of the actual state variables on a lower dimensional space. The problem of converting the observations into state variables is referred to as phase-space

reconstruction (embedding) and is solved using Taken's embedding theorem (Takens, 1980). The general form of multivariate embedding is given by the equation

$$y^n = (\phi_1^n, \phi_2^n, \cdots, \phi_j^n) \tag{3.1}$$

where $\varphi^n_j = \{x_j(t), x_j(t-\tau), x_j(t-2\tau), \ldots, x_j(t-(n-1)\tau)\}$ are time delay vectors formed from the fMRI time series $x_j(t)$, j is the number of fMRI time series used, n is the embedding dimension (Cao *et al*, 1998), and τ is the embedding lag. The embedding dimension is basically an estimate of the number of independent and orthogonal parameters required to describe the dynamic evolution of the system. The choice of the time series, embedding dimensions and embedding lag have to be made based on a justifiable criterion. In the present work, the choice of these parameters is made by using the idea of minimizing a cost function which reflects the prediction error in the embedded state space (Cao *et al*, 1998). The cost function is given by-

$$(d_1, d_2, \ldots, d_M) = \arg\min\left\{ E(d_1, d_2, \ldots, d_M) : (d_1, d_2, \ldots, d_M) \in Z^M, \sum_{i=1}^{M} d_i \neq 0 \right\} \tag{3.2}$$

$$E(d_1, d_2, \ldots, d_M) = \frac{1}{N - J_o + 1} \sum_{n \neq J_o}^{N} \left| x_{1,n+1} - x_{1,\eta(n)+1} \right|, J_o = \max_{1 \le i \le M} (d_i - 1)\tau_i + 1 \tag{3.3}$$

where d_i's are the embedding dimensions, $x_{i,j}$ are points in the state space, τ_i are the embedding lags, Z is the set of all non-negative integers and Z^M is the M-dimensional vector space corresponding to the scalar set Z. $d=d_1+d_2+\ldots+d_M$ represents the multivariate embedding dimension of all the time series taken together.

We introduce the bivariate nonlinear connectivity index (BNC), which is based on the bivariate and univariate embedding dimensions, to measure nonlinear functional connectivity between any two regions of interests (ROI) in the brain. Let d_1 and d_2 be the univariate embedding dimensions of fMRI time-series 1 and 2 obtained from respective ROIs. Let d be the bivariate embedding dimension of the two time series embedded together (as a special case of the more general multivariate embedding formulation described above). Then, we define

$$BNC = 1 - \frac{|d - d_1| + |d - d_2|}{d_1 + d_2} \tag{3.4}$$

When the two time series are fully connected, the bivariate dimension does not provide any extra information and $d=d_1=d_2$ and $BNC=1$. When the two time series are fully independent, $d=d_1+d_2$ and $BNC=0$. Therefore, higher values of BNC are associated with higher connectivity. Since this method makes no assumption of linearity, both linear and nonlinear couplings are accounted for.

Data Acquisition and Analysis

Resting State Paradigm

Two runs of echo-planar imaging (EPI) data were acquired, one during resting state and one during performance of a block design finger tapping paradigm, on 3 human subjects using a 3T Siemens Trio. Scan parameters were: repetition time (TR) =750 ms, echo time (TE) =34 ms, flip angle (FA)=50 deg and field of view (FOV)=22cm, with 5 axial slices, 5mm slice thickness, 1120 images and 64 phase and frequency encoding

steps. A physiological monitoring unit consisting of a pulse-oximeter and nasal respiratory cannula was used during data acquisition to record cardiac and respiratory signals, respectively. These physiological fluctuations were corrected in the functional data retrospectively (Hu *et al*, 1995).

Subsequent to motion correction and removal of signal drifts, four regions of interests (ROI) - left motor (LM), right motor (RM), frontal (F) and supplementary motor (SMA) -were identified based on the activation maps obtained from the finger tapping data. A mean time course was calculated for each ROI. BNC was calculated between the time course of LM and that from each of the other ROIs. A Kolmogorov-Smirnov test, based on the null hypothesis that the BNC values are purely attributed to noise, was performed to test the significance.

The slice with the most motor activation pattern (obtained from the block design paradigm) was examined with both the BNC method and correlation analysis, using a seed voxel in the left primary motor cortex identified from the activation data. For both methods, a threshold was chosen to select the top 10% of connected brain voxels and corresponding maps were obtained for comparison.

Continuous Motor Paradigm

EPI data was acquired in three healthy volunteers while they performed a continuous self-paced bimanual tapping of the thumb with the index, middle, ring and little fingers (in that order). Scan parameters were: TR= 750 ms, TE= 34 ms, FA= 50°, FOV=22 cm, 1120 volumes and 10 slices spanning the corpus callosum to the top of the head. Activated voxels were identified using independent component analysis (McKeown

et al, 1998) and a reference region was defined in bilateral motor cortex. The mean time course of the reference region was chosen as the seed for further analysis. Linear functional connectivity was estimated as the cross-correlation between the seed voxel and all other voxels (candidates) in slices containing the motor cortex whereas BNC was calculated as a measure of nonlinear functional connectivity between the seed and other voxels. Functional connectivity was calculated using three non-overlapping time windows, each containing 373 volumes. The significance of the changes in functional connectivity was ascertained using the Wilcoxon rank sum test.

Results and Discussion

Resting State Paradigm

Table.1 lists the BNC and linear correlation (LC) values for resting state fMRI data. LM↔RM and LM↔SMA exhibit strong connectivity, in agreement with results reported earlier (Biswal *et al*, 1995).

Table 3.1 Significant FC and EC for resting-state fMRI data for two representative subjects

	Network	Linear Connectivity (LC)	Nonlinear Connectivity (BNC)
Subject 1	LM↔SMA	0.76	0.52
	LM↔RM	0.73	0.89
	LM↔F	0.22	0.15
Subject 2	LM↔SMA	0.49	0.63
	LM↔RM	0.57	0.76
	LM↔F	0.45	0.54

The thresholded connectivity maps are shown in Fig.3.1. The BNC approach was able to identify a connection between a seed in the left motor area (yellow arrow) and right motor area, SMA, and a medial frontal region (blue arrow) in the third subject (Fig.3.1). Although there are similarities between the connectivity identified with the BNC approach and that by the correlation analysis with the same seed, significant differences are present indicating that the embedding approach is likely to capture nonlinear correlations that may not be detected using linear correlation. In addition, the region indicated by the green arrow is a spurious correlation near a draining vein. Note that this region was not identified by the BNC method, suggesting that the nonlinear technique has enhanced specificity to the desired gray matter signal.

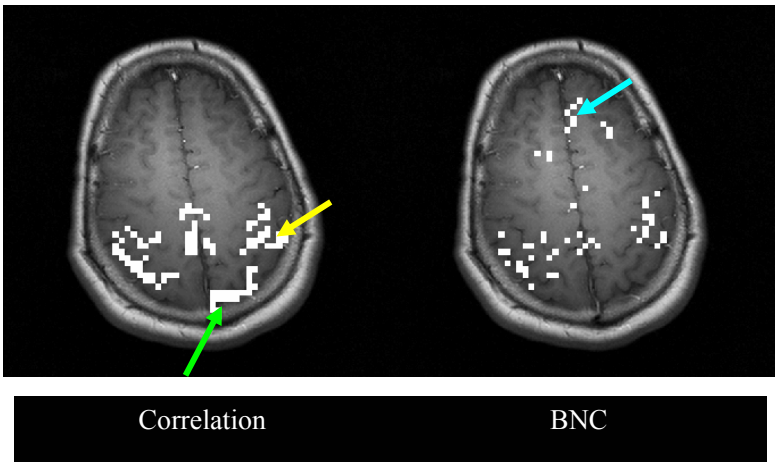

Figure 3.1 Baseline data connectivity maps derived using linear correlation and BNC

Continuous Motor Paradigm

The change in the magnitude of functional connectivity with the progression of time was not significant, though it showed an increasing trend. However, the number of

significantly connected voxels ($p<0.05$) increased with time (Table.3.2). Also, nonlinear functional connectivity was seen in additional areas besides the voxels which exhibited linear functional connectivity (Fig.3.2). Previously, a progressive decrease in the magnitude of functional correlation has been reported in a unimanual event-related fatigue motor task, though it was shown that activation volume increased (Liu *et al*, 2005). Our study reveals that in the absence of fatigue, additional resources, which closely coordinate with each other, might be recruited by the motor system in learning the task.

Table 3.2 Dynamic changes in the number of connected significant voxels using linear correlation and BNC

Sub	FC	Window-1	Window-2	Window-3
1	LC	115	439	629
	BNC	393	938	1457
2	LC	500	702	1001
	BNC	970	1087	1456
3	LC	89	453	1085
	BNC	647	1023	1654

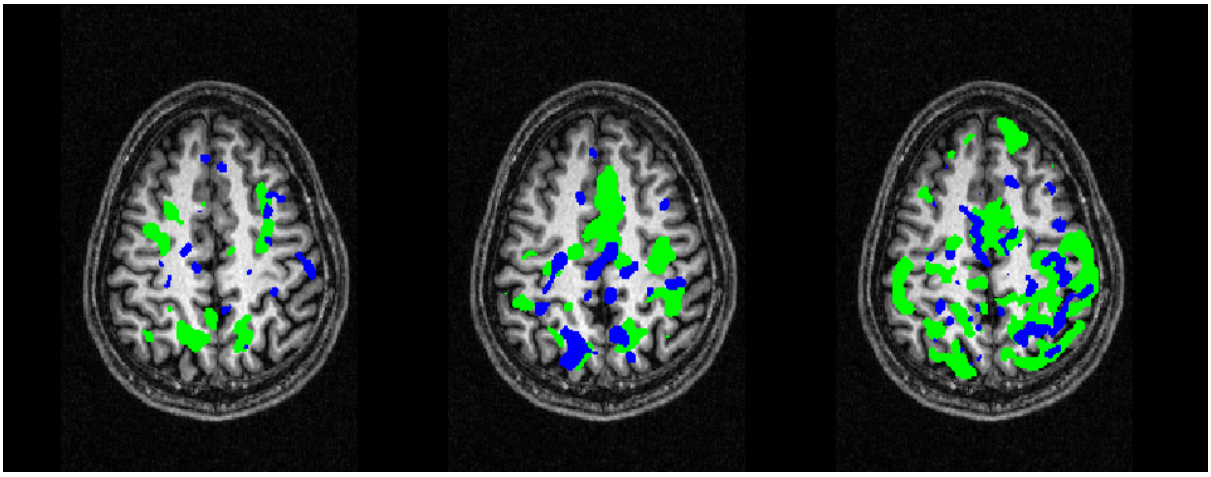

Figure 3.2 Linear and nonlinear connectivity maps overlaid on the T1-weighted anatomical image for initial (left), middle (center) and final (right) time windows. Significance threshold $p=0.05$. Green: Both significant correlation and BNC, Blue: Only significant BNC

Conclusions

In this work we have presented the functional connectivity analysis of distributed brain networks using fMRI data obtained from the human brain under resting state and continuous bimanual movement. We have introduced nonlinear techniques to infer functional connectivity using the concept of embedding and demonstrated its advantages with respect to linear methods in terms of its sensitivities to nonlinear couplings and insensitivities to confounds introduced by draining veins. The utility of dynamical analysis is shown in the context of investigating temporally evolving neuronal changes. In conclusion, we have made a strong case for nonlinear and dynamical connectivity analysis of neuroimaging data.

CHAPTER 4

EFFECTIVE CONNECTIVITY IN DISTRIBUTED NETWORKS

Introduction

In functional neuroimaging, brain networks are primarily studied in terms of functional connectivity (defined as temporal correlations between remote neurophysiologic events) and effective connectivity (defined as the causal influence one neuronal system exerts over another) (Friston *et al*, 1995). Though the two prominent approaches to characterizing effective connectivity - structural equation modeling (McIntosh *et al*, 1994) and dynamic causal modeling (Friston *et al*, 2003) - have their advantages and disadvantages, neither of them incorporate information on temporal precedence (the assignment of cause and effect), which is central to the concept of causality. Also, these techniques require an a priori specification of an anatomical network model and are therefore best suited to making inferences on a limited number of possible networks. Recently an exploratory structural equation model approach that does not require prior specification of a model was described (Zhuang *et al*, 2005). However with increasing number of regions of interest, its computational complexity becomes intractable and the numerical procedure becomes unstable. These disadvantages can largely be circumvented by methods such as Granger's causality which are based on the cross-prediction between two time series (Granger, 1969).

With fMRI data, recent studies have applied Granger causality analysis between a target region of interest (ROI) and all other voxels in the brain to derive Granger causality maps (Roebroeck *et al*, 2005; Abler *et al*, 2006). A major limitation of applying

the target ROI based approach to neuroimaging data is that it is a bivariate method and ignores interactions between other ROIs in the underlying neuronal network leading to an oversimplification of the multivariate neuronal relationships that exist during the majority of cognitive tasks. Simulations by Kus *et al* (Kus *et al*, 2004) have shown that a complete set of observations from a process have to be used to obtain causal relationships between them and that pair-wise estimates may yield incorrect results. To date, multivariate measures of Granger causality have been largely limited to electrophysiological data (Ding *et al*, 2000; Kaminski *et al*, 2001; Kus *et al*, 2004; Blinowska *et al*, 2004). For fMRI, we have recently presented early forms of the full study described in this chapter (Deshpande *et al*, 2006a; 2006b).

A critical consideration for fMRI data is the limitations imposed by the hemodynamic response. The fMRI response is dictated by the sluggish hemodynamic response which is believed to be spatially dependent (Aguirre *et al*, 1998; Silva *et al*, 2002; Handwerker *et al*, 2004). Given that the hemodynamic response takes 6-10 seconds, Granger causality analysis applied to the measured raw time series sampled with a TR on the order of a second may be contaminated by regional differences in the hemodynamic response. We alleviate the effect of spatially varying hemodynamic delay by focusing on the causal relationships at a temporal scale much coarser than the hemodynamic response. Neuronal processes such as fatigue, learning and habituation evolve slower than the hemodynamic response and are amenable to a coarse temporal scale causal analysis.

Another consideration is that multivariate causality relationships can be difficult to interpret and to compare across data sets. With several anatomical regions included in

a network, the possible number of interconnections between them increases exponentially. The complexity of the problem is further increased by our desire to characterize the temporal evolution of these network interactions. Graph theoretic concepts are well suited to represent the information present in these networks. Graphical representations for fMRI-derived causal neuronal networks were introduced recently in the context of studying unmeasured latent variables in effective connectivity analysis (Eichler, 2005). The utility of graphical models in characterizing the topology of large networks has been demonstrated in the case of anatomical networks in macaques (McIntosh *et al*, 2006), and functional networks obtained from MEG (Stam, 2004) and EEG (Fallani *et al*, 2006; Sakkalis *et al*, 2006). In the present study, we have used the graphical representation for effective characterization of the network topology. In addition to utilizing concepts such as clustering (Stam, 2004; Fallani *et al*, 2006; Sakkalis *et al*, 2006), we introduce the application of eccentricity analysis to determine the ROIs having a major influence on the network.

In this work, we have adapted the directed transfer function (DTF) which was recently introduced as a causal multivariate measure for EEG (Kus *et al*, 2004). The DTF is based on Granger causality, but is rendered in a multivariate formulation (Blinowska *et al*, 2004) and hence is effective in modeling the inherent multivariate nature of neuronal networks. For our application, we used the product of the non-normalized DTF and partial coherence to emphasize the direct connections and de-emphasize mediated influences. Using an extended period of fMRI data collected during a fatigue experiment (Peltier *et al*, 2005a), we extracted the area under each epoch to form a summary time series which captures the epoch-to-epoch variation. The rationale was that this is more

likely to reflect the physiological process of fatigue and also alleviates the effect of the spatially varying hemodynamic delay. Further, we investigated the changes in the dynamics of the networks as the subjects progressively fatigued, demonstrating the utility of this approach.

As we have seen in the previous chapter, nonlinear approaches either provide some additional information or are insensitive to artifacts or provide a complimentary approach to the linear methods. Therefore we further explore the nonlinear granger causality approach in this work. The basic idea behind nonlinear Granger causality is to perform nonlinear prediction in phase space as compared the linear prediction in scalar space performed by linear Granger causality. A nonlinear Granger model in embedded space was recently proposed and validated using numerical simulations (Chen *et al*, 2004), which was subsequently extended using the radial basis function (RBF) approach (Ancona *et al*, 2004). In this study, we adopt the RBF approach for application to fMRI data acquired during a continuous motor task as it is more suitable for short and noisy time series such as fMRI. The adoption of the continuous motor task is another way of circumventing the spatial variability of the hemodynamic response apart from the summary time series approach used in the linear study. Here we focus on comparing the nonlinear model with the linear model for which bivariate maps are obtained. It is to be noted that a bivariate nonlinear model is used for the simplicity of comparison with the linear model but could however be extended to the multivariate model as in the linear case.

Methods

Linear Granger Causality

Data Acquisition and Pre-processing

Ten healthy right-handed male subjects performed a prolonged motor task while they were scanned in a 3T Siemens Trio. Informed consent was obtained prior to scanning and the procedure was approved by the internal review board at Emory University. The subjects performed repetitive right-hand contractions at 50% maximal voluntary contraction (MVC) level by gripping a bottle-like device (Liu *et al*, 2002). Online measurement of handgrip force was accomplished by a pressure transducer connected to the device through a nylon tube filled with distilled water. For each subject, the target level of 50% MVC was calculated based on the maximal grip force measured at the beginning of the experiment. Visual cues (a rectangular pulse whose profile matched the amplitude and duration of the handgrip contraction) were generated by a waveform generator and projected onto the screen above the subject's eye in the magnet to guide the subjects in performing the contractions. Each contraction lasted 3.5 seconds, followed by a 6.5 second inter-trial interval (ITI). The total fatigue task comprised of 120 contractions lasting 20 minutes. After the completion of the task, the level of muscle fatigue was determined by measuring the MVC handgrip force. The choice of 50% MVC level was made so as to fatigue the muscles in approximately 10-15 minutes for the given length of contraction and ITI. Echo planar imaging (EPI) data was obtained with the following scan parameters: Thirty 4-millimeter slices (no gap) covering from the top of the cerebrum to the bottom of the cerebellum, 600 volumes, repetition time (TR) of 2 s, echo

time (TE) of 30 ms, a flip angle (FA) of 90°, and an in-plane resolution of 3.44×3.44 mm^2.

The data analysis for activation detection was carried out using Brainvoyager™ 2000 (Ver 4.9 © Rainer Goebel and Max Planck Society, Maastricht, The Netherlands. www.brainvoyager.com). Two subjects were excluded from the analysis due to excessive head motion. Subsequent to motion and slice scan time correction, a reference waveform derived based on the activation paradigm (Fig. 4.1) was correlated with each voxel time series to produce activation maps (Fig. 4.2). The correspondence of the activation paradigm with a time series from the primary motor area is illustrated in Fig. 4.1. As shown in Fig. 4.2, six ROIs – contralateral (left) primary motor (M1) cortex, primary sensory cortex (S1), pre-motor area (PM), ipsilateral (right) cerebellum (C), supplementary motor area (SMA), and medial parietal area (P) - were identified from the activation maps, and ROI specific average time courses were obtained. Due to the overlap of activations in M1 and S1, these areas were delineated based on the location of central sulcus (Yousry *et al*, 1997) by assigning the activations in the pre-central gyrus as M1 and that in the post-central gyrus as S1. SMA activation was taken to be medial and the parietal activation included both medial and contra-lateral activations in the posterior parietal cortex.

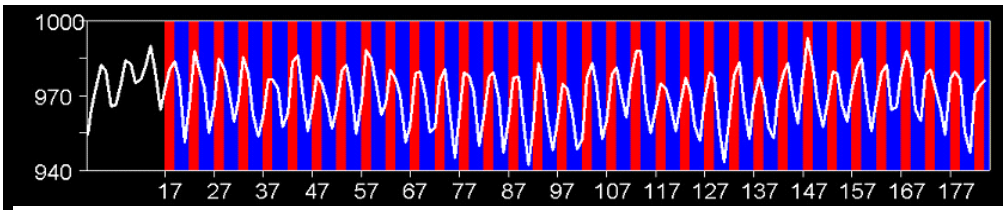

Figure 4.1 A time series from M1 overlaid on the activation paradigm. Red: 3.5 sec contraction. Blue: 6.5 sec inter trial interval

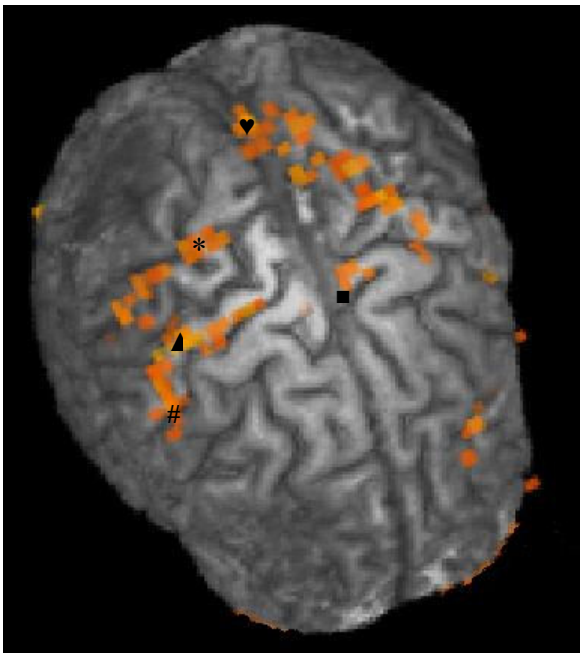

Figure 4.2 A sample activation map obtained from the fatigue motor task showing the regions of interest. ■ SMA, ▲M1, * S1, ♥ P, # PM

To investigate fatigue induced causal influences, the area under the time course of each epoch was calculated as a summary measure and a corresponding summary time series was derived from the mean time series for each ROI (Fig. 4.3).

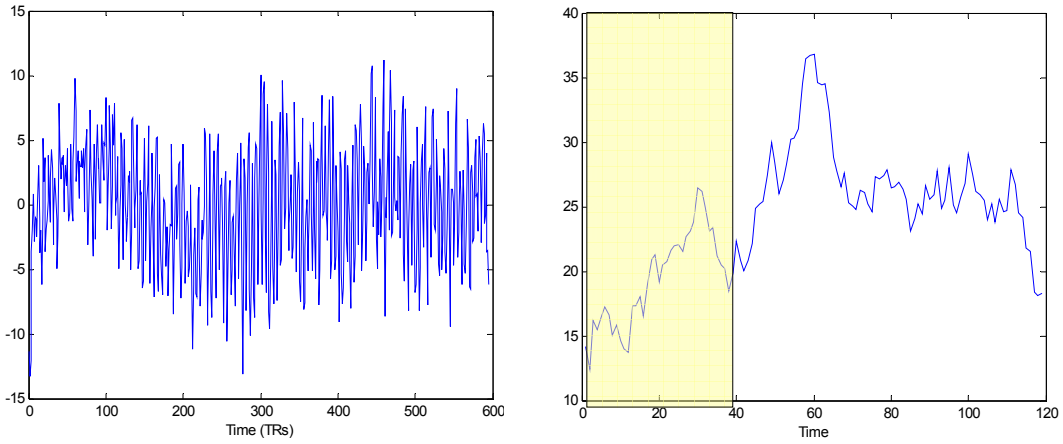

Figure 4.3 Left: Original fMRI time series. Right: Summary time series (yellow patch shows the first time window).

Three non-overlapping segments from this time series, each containing 40 points, was input into the multivariate Granger causality analysis. The use of these windows allowed us to investigate the temporal dynamics of the network.

Multivariate Granger Causality Analysis

The principle of Granger causality is based on the concept of cross prediction. Accordingly, if incorporating the past values of time series X improves the future prediction of time series Y, then X is said to have a causal influence on Y (Granger, 1969). In the case of any two time series X and Y, the efficacy of cross-prediction could be inferred either through the residual error after prediction (Roebroeck *et al*, 2005) or through the magnitude of the predictor coefficients (Blinowska *et al*, 2004). As shown by earlier reports (Kaminski *et al*, 2001), given multivariate time series, residual error could not be used to derive the simultaneous causal relationships between all of them; instead the predictor coefficients had to be used as the basis for multivariate Granger causality. In this section, we describe the multivariate model of Granger causality used in this study.

The causality analysis was accomplished using software written in MATLAB (The MathWorks Inc, Massachusetts). A multivariate autoregressive (MVAR) model was constructed from the summary time series of the ROIs. In the following, an italic capital letter represents a matrix with components corresponding to the ROIs and the variable in the parenthesis indicates either time or temporal frequency. Let $\boldsymbol{X}(t) = (x_1(t), x_2(t) \ldots x_k(t))$ be the data matrix and x_k correspond to the time series obtained from the k^{th} ROI. The MVAR model with model parameters $\boldsymbol{A}(n)$ of order p is given by

$$\boldsymbol{X}(t) = \sum_{n=1}^{p} \boldsymbol{A}(n)\boldsymbol{X}(t-n) + \boldsymbol{E}(t) \tag{4.1}$$

where ***E(t)*** is the vector corresponding to the residual error. Akaike information criterion was used to determine the model order (Akaike, 1974). Eq. 4.1 was transformed to the frequency domain resulting in

$$X(f) = A^{-1}(f)E(f) = H(f)E(f) \tag{4.2}$$

where $$a_{ij}(f) = \delta_{ij} - \sum_{n=1}^{p} a_{ij}(n)\, e^{-i2\pi f n} \;\; and \;\; H(f) = A^{-1}(f) \tag{4.3}$$

δ_{ij} is the Dirac-delta function which is one when $i = j$ and zero elsewhere. Also, $i = 1 \cdots k$, $j = 1 \cdots k$ where k is the total number of ROIs. The transfer matrix of the model, *H(f)*, contains all the information about the interactions between the time series and $h_{ij}(f)$, the element in the i^{th} row and j^{th} column of the transfer matrix, is referred to as the non-normalized DTF (Kus *et al*, 2004) corresponding to the influence of ROI *j* onto ROI *i*. In order to emphasize direct connections and de-emphasize mediated influences, $H_{ij}(f)$ was multiplied by the partial coherence between ROIs *i* and *j* to obtain direct DTF (dDTF) (Kus *et al*, 2004). In order to calculate the partial coherence, we first computed the cross-spectra using

$$S(f) = H(f).V.H^{*}(f) \tag{4.4}$$

where V is the variance of the matrix $E(f)$ and the asterisk denotes transposition and complex conjugate. The partial coherence between ROIs i and j is then given by

$$\eta_{ij}(f) = \frac{M_{ij}^2(f)}{M_{ii}(f)M_{jj}(f)} \tag{4.5}$$

where $M_{ij}(f)$ is the minor obtained by removing the i^{th} row and j^{th} column from the matrix S. The partial coherence between a pair of ROIs indicates the association between them when the statistical influence of all other ROIs is discounted. It lies in the range [0, 1] where a value of zero indicates no direct association between the ROIs. The direct DTF (dDTF) was obtained as the sum of all frequency components of the product of the non-normalized DTF and partial coherence as given in the equation below.

$$dDTF_{ij} = \sum_f H_{ij}(f)\eta_{ij}(f) \tag{4.6}$$

dDTF as defined above emphasizes the direct connections between ROIs. It is to be noted that unlike previously reported studies (Kaminski *et al*, 2001; Kus *et al*, 2004; Blinowska *et al*, 2004), we avoided normalizing DTF so as to allow direct comparison between the absolute values of the strengths of influence. Normalization of DTF with respect to inflows into any ROI as in Kus *et al* (Kus *et al*, 2004) would make such a comparison untenable. As described in the previous sub-section, the calculation of dDTF was carried out using the summary time series in three non-overlapping windows so as to investigate the temporal dynamics of the network.

Statistical Significance Testing

Analytical distributions of multivariate Granger causality are not established since they are said to have a highly nonlinear relationship with the time series data (Kaminski *et al*, 2001). Therefore, to assess the significance of the causality reflected by dDTF, we employed surrogate data (Theiler *et al*, 1992; Kaminski *et al*, 2001; Kus *et al*, 2004) to obtain an empirical null distribution. The original time series was transformed into the frequency domain and their phase was randomized so as to be uniformly distributed over $(-\pi, \pi)$ (Kus *et al*, 2004). Subsequently, the signal was transformed back to the time domain to generate the surrogate data. This procedure ensured that the surrogate data possessed the same spectrum as the original data but with the causal phase relations destroyed. dDTF was calculated between the surrogate data time series representing each ROI. Null distributions were derived for all possible connections between the ROIs, in each time window and for every subject, by repeating the above procedure 2500 times. Therefore, corresponding to six ROIs (we had 30 possible links between the ROIs) and three time windows, a total of 90 null distributions were generated per subject. In order to obtain a group significance threshold, we combined the null distributions obtained from the 8 subjects using the consensus inference method (Hansen *et al*, 2001). This approach involved histogram equalization of all distributions into a common scale and averaging the equalized histograms. The position of the mean dDTF value of every connection in the corresponding null group distribution was ascertained. In order to estimate the p-value for the mean dDTF, the fractional area of the null group distribution for this position was calculated. Subsequent to obtaining the p-values for all the connections in

the three temporal windows, a one way ANOVA was carried out with the variation of dDTF across subjects being tested for significance.

Analysis using Graph Theory

The causal influences between the ROIs in a network could in principle be represented as a weighted directed graph, whose weights are represented by the dDTF value for the corresponding link between the ROIs, the direction of the link being the direction of causal influence and the ROIs themselves representing the vertices (or nodes) of the network. As mentioned in the introduction, this type of representation has been used to characterize network topology of causal functional networks obtained from MEG data (Stam, 2004) and EEG (Fallani *et al*, 2006; Sakkalis *et al*, 2006). In this study, we focus on clustering and eccentricity. While clustering has been used previously (Stam, 2004; Fallani *et al*, 2006; Sakkalis *et al*, 2006), we have adopted the concept of eccentricity from graph theory (Edwards, 2000) and have shown its relevance in interpreting the resultant networks.

Mathematical Representation of a Graph

A graph G is mathematically represented in the form of a sparse matrix called the adjacency matrix (Skiena, 1990). The adjacency matrix of the directed graph is a matrix with rows and columns labeled by graph vertices (v), with the dDTF value corresponding to the influence from v_j to v_i in the position (v_i,v_j).

Clustering Coefficient

One of the most important aspects of the topology of a network is the role of the nodes as either drivers of other nodes or being driven by other nodes. This is assessed by the total strength of causal influence that is emanating from or incident on the node. Correspondingly, cluster-in and cluster-out coefficients (Watts *et al*, 1998) for node *i* are defined as,

$$C_{in} = \sum_{j=1}^{p} G(v_i, v_j) \tag{4.7}$$

$$C_{out} = \sum_{i=1}^{p} G(v_i, v_j) \tag{4.8}$$

where *p* (in this case equal to 6) is the number of nodes in the network. While calculating clustering coefficients from the fatigue data, the mean dDTF averaged over the subjects were used as entries in the matrix *G*. Also, the analysis was carried out separately for each of the three temporal windows.

Eccentricity

The eccentricity *E(v)* of a graph vertex *v* in a connected graph *G* is the maximum geodesic distance between *v* and any other vertex *u* of *G*. The geodesic distance between two vertices in a weighted graph is the sum of the causal influences along the shortest path connecting them. We used the Floyd-Warshall algorithm for solving the all-pairs shortest path problem (Cormen *et al*, 2001) to the find the shortest path between any pairs of nodes. Given that graph distance is measured in terms of the strength of causal

influence, the shortest path between two nodes indicates the path along which maximum causal influence is exerted. Eccentricity is related to the individual influence of a vertex on the overall network performance (Skiena, 1990). A vertex *v* is said to have a major influence on the network performance if it has the maximum *E(v)* among all vertices in the graph. Such a vertex, termed the major node, wields maximum influence on network behavior. The major nodes in each time window were ascertained to infer the changing roles of brain regions.

Nonlinear Granger Causality

Data Acquisition

EPI data was acquired in a 3T Siemens Trio scanner from three healthy volunteers while they performed continuous bimanual tapping of the thumb with the index, middle, ring and little fingers (in that order), respectively. The subjects were provided visual feedback where in the numericals from one to four were displayed at a constant rate so that the subjects could synchronize their tapping of the fingers with the rate of display. This procedure ensured that the subjects tapped their fingers at a constant rate so that the results were not contaminated with effects of the pace of tapping. Scan parameters were: TR= 750 ms, TE= 34 ms, FA= 50°, FOV=22 cm and 1120 volumes.

Nonlinear Granger causality model

For any given two time series *x(t)* and *y(t)*, the bivariate linear model is given by

$$x(t) = \sum_{i=1}^{p} v_{11}(i)\, x(t-i) + \sum_{i=1}^{p} v_{12}(i)\, y(t-i) + e_{xy}(t) \qquad (4.9)$$

$$y(t) = \sum_{i=1}^{p} v_{21}(i)\, x(t-i) + \sum_{i=1}^{p} v_{22}(i)\, y(t-i) + e_{yx}(t) \tag{4.10}$$

where $V = \begin{bmatrix} v_{11} & v_{12} \\ v_{21} & v_{22} \end{bmatrix}$ are the predictor co-efficients, p is the model order and e_{xy} and e_{yx} are the residual errors. Instead of predicting the future of the time series based on its past scalar values, the prediction can be based on the past vector values in the embedded space (Chen *et al*, 2004). This renders the prediction scheme nonlinear. Let $\boldsymbol{x}(t)$ and $\boldsymbol{y}(t)$ represent the embedding as shown below.

$$\boldsymbol{x}(t) = (x(t-\tau\ ), x(t-2\tau\ )\quad \cdots \quad x(t-(n-1)\tau\ )) \tag{4.11}$$

$$\boldsymbol{y}(t) = (y(t-\tau\ ), y(t-2\tau\ )\quad \cdots \quad y(t-(n-1)\tau\ )) \tag{4.12}$$

where n is the embedding dimension and τ is the embedding lag. Then, prediction in the phase space is represented as

$$\boldsymbol{x}(t) = \sum_{i=1}^{p} \boldsymbol{v}_{11}(i)\, \boldsymbol{x}(t-i) + \sum_{i=1}^{p} \boldsymbol{v}_{12}(i)\, \boldsymbol{y}(t-i) + \boldsymbol{e}_{xy}(t) \tag{4.13}$$

$$\boldsymbol{y}(t) = \sum_{i=1}^{p} \boldsymbol{v}_{21}(i)\, \boldsymbol{x}(t-i) + \sum_{i=1}^{p} \boldsymbol{v}_{22}(i)\, \boldsymbol{y}(t-i) + \boldsymbol{e}_{yx}(t) \tag{4.14}$$

where the bold faced letters are the corresponding phase space vector equivalents of the scalar values in Eq. 4.9 and Eq. 4.10. According to Ancona *et al* (2004), any prediction scheme should satisfy the following property: *if* $\boldsymbol{y}$ *is statistically independent of* $\boldsymbol{x}$, *then*

$\boldsymbol{e_x}$= $\boldsymbol{e_{xy}}$; *if* $\boldsymbol{x}$ *is statistically independent of* $\boldsymbol{y}$, *then* $\boldsymbol{e_y}$= $\boldsymbol{e_{yx}}$. They also contend that the approach by Chen *et al* (2004) corresponding to Eq. 4.13 and Eq. 4.14 satisfies the above property only if the point density in the phase space is high enough. This leads to the condition that the time series be long and less noisy. These conditions are hard to satisfy in the case of fMRI where we have short and noisy time series. Therefore we adopt RBFs to model the past values of the embedded time series vectors (Ancona *et al*, 2004) as given below

$$\boldsymbol{x}(t) = \sum_{i=1}^{n} \boldsymbol{w}_{11}(i)\Phi_s(x) + \sum_{i=1}^{n} \boldsymbol{w}_{12}(i)\Psi_s(y) + \boldsymbol{e}_{xy}(t) \tag{4.15}$$

$$\boldsymbol{y}(t) = \sum_{i=1}^{n} \boldsymbol{w}_{21}(i)\Phi_s(x) + \sum_{i=1}^{n} \boldsymbol{w}_{22}(i)\Psi_s(y) + \boldsymbol{e}_{yx}(t) \tag{4.16}$$

where $\{\boldsymbol{w}\}$ are four n-dimensional real vectors, $\Phi=(\varphi_1 \ldots \varphi_n)$ are n given RBFs to represent x's past, and $\Psi=(\psi_1 \ldots \psi_n)$ are n other RBFs to represent y's past. Φ and Ψ represent RBFs centered at the locations s. n such locations were determined by fussy c-means clustering (Cannon *et al*, 1986) in the n-dimensional embedded space reconstructed using $n-1$ past values of x and y, respectively. The value of n was chosen so as to minimize the model error. Similar models were constructed for self prediction of x using x's past and y using y's past only as shown below

$$\boldsymbol{x}(t) = \sum_{i=1}^{n} \boldsymbol{w}_{11}(i)\Phi_s(x) + \boldsymbol{e}_x(t) \tag{4.17}$$

$$\boldsymbol{y}(t) = \sum_{i=1}^{n} \boldsymbol{w}_{22}(i)\Psi_s(y) + \boldsymbol{e}_y(t) \tag{4.18}$$

Let the resulting model residuals be $\boldsymbol{e_x}$ and $\boldsymbol{e_y}$ respectively. Then the directionality index (D) is defined as given below

$$D = \frac{c_2 - c_1}{c_2 + c_1} \tag{4.19}$$

where $$c_1 = \boldsymbol{e_x} - \boldsymbol{e_{xy}} \quad and \quad c_2 = \boldsymbol{e_y} - \boldsymbol{e_{yx}} \tag{4.20}$$

D=-1 for unidirectional influence from y to x and D=1 for x to y. However D=0 may either indicate that the influence is fully bidirectional or that there is no influence i.e. it indicates the lack of net drive in any direction. This is one of the disadvantages of directional maps obtained from a bivariate model in contrast to the multivariate model described in the previous section. However, it offers the advantage of pictorial representation using maps. It is to be noted that in a bivariate model, residual errors could be used to ascertain the magnitude and direction of influence while in the multivariate case, predictor coefficients have to be employed.

Data Analysis

Subsequent to motion correction, activated voxels were identified using independent component analysis (Mckeown *et al*, 1998). The mean voxel time series from SMA was chosen as the seed voxel and was input into the nonlinear Granger model along with every other voxel in the brain slice (candidate voxels) to obtain causal maps of the directionality index. In addition, linear Granger maps were obtained using the same seed

for comparison with the nonlinear model. To investigate the effect of artifacts, the maps were obtained both with and without the removal of baseline drift.

Results

Linear Granger Causality

Behavioral Data and Pre-processing

There was a significant decrease ($p<0.002$) in hand grip force measured after the motor task as compared to before the task, indicating that significant muscle fatigue had occurred. Of the eight subjects selected for analysis, behavioral data was not available for two subjects due to technical difficulties. In the rest of the six subjects, the decrease in hand grip force was 29 ±11 % (Peltier *et al*, 2005a). Fig. 4.2 shows a sample activation map obtained by correlating the fMRI time series with the reference waveform and the ROIs selected for further analysis. A representative summary and original time series are shown in Fig. 4.3 (Figs. 4.2 and 4.3 were shown earlier). It can be seen that the summary time series captures the slow epoch-to-epoch variation.

Multivariate Granger Causality

A model order of one was assigned based on the Akaike information criterion (Akaike, 1974). Since a single time point in the summary time series corresponds to the area under the corresponding epoch, the resulting MVAR model represents epoch-to-epoch prediction. The temporal variation of the significance values α (α=1-p) for connections between all pairs of ROIs is shown in Fig. 4.4. The links that passed the

significance threshold of α=0.95 are represented by the bars in red while the connections that did not pass the threshold are shown as green bars. A one-way ANOVA showed that the dDTF variation across subjects was not significant (p>0.05), indicating that the results were consistent across subjects. The network representation of the results in Fig. 4.4 is shown in Fig. 4.5, where the significant connections are shown as solid lines with their width reflecting the statistical significance of the influence. It is to be noted that the absence of a connection does not necessarily imply that there is no causal influence between the corresponding ROIs. A more lenient threshold or additional statistical power might render an insignificant connection significant.

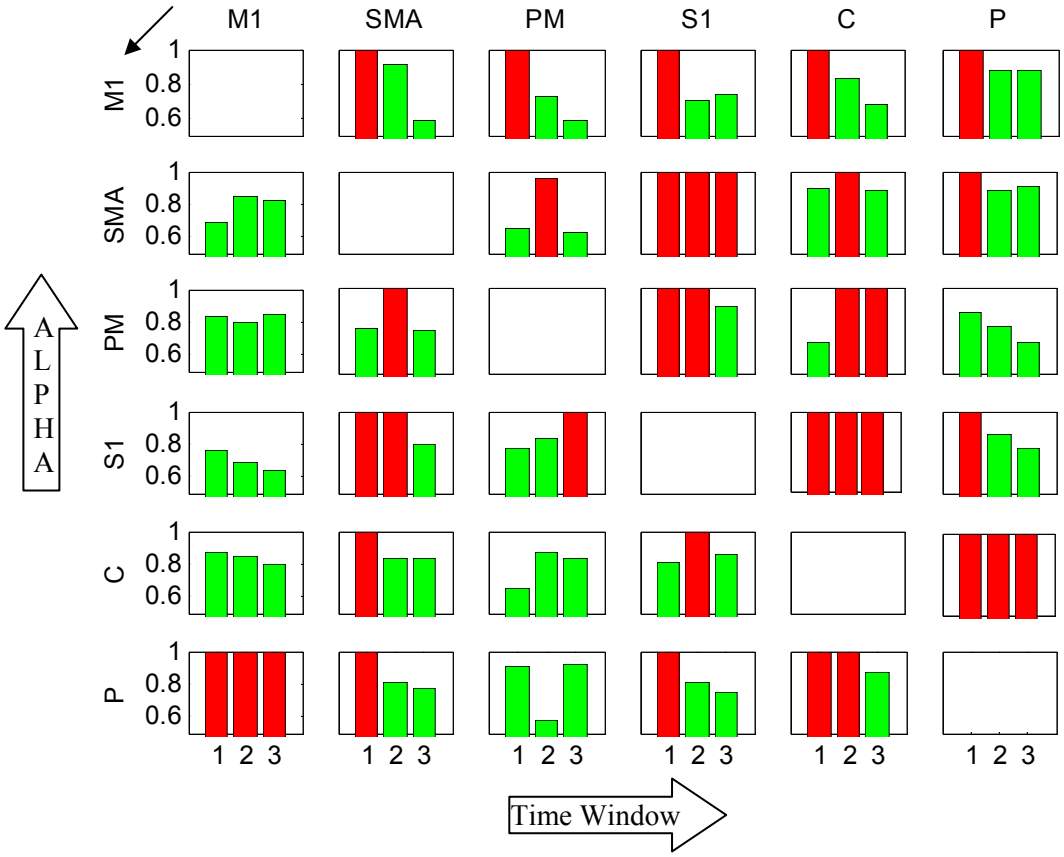

Figure 4.4 The temporal variation of significance value α (α=1-p) for all possible connections between the ROIs. The direction of influence, as indicated by the black arrow, is from the columns to the rows. The red bars indicate the connections that passed the significance threshold of α=0.95 and the green ones that did not

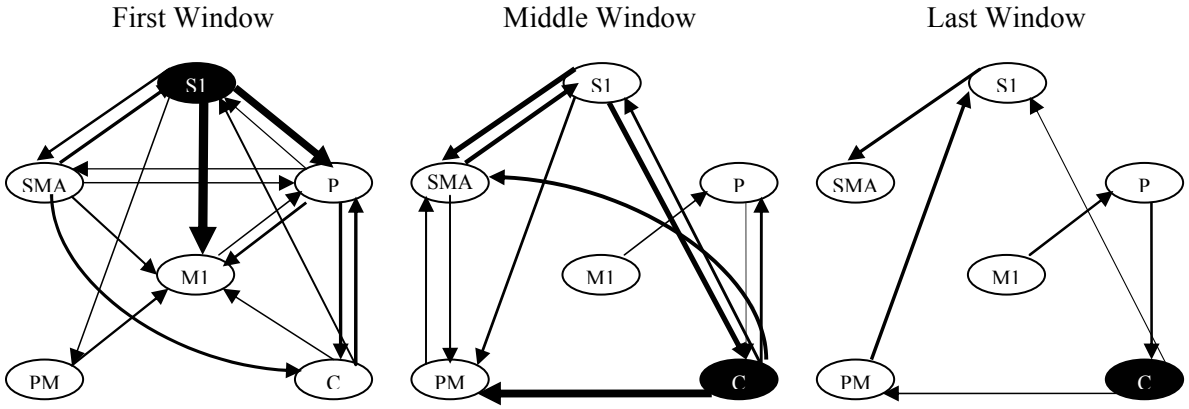

Figure 4.5 A network representation of Fig. 4.4. The significant links are represented as solid arrows and the p-value of the connections are indicated by the width of the arrows. The major node in each window is also indicated as dark ovals

Graph Analysis

Clustering Coefficients

Table 4.1 lists C_{in} and C_{out} for the three windows. In the first window, M1 was predominantly driven while S1 was a strong driver. The other areas had a dual role in the sense that they both received and transmitted information. In the second window, S1 and cerebellum were strong drivers. In the third window, while S1 and cerebellum remained to be the main drivers, the absolute value of the coefficients decreased for all ROIs, indicating a reduction of network connectivity. This reduction, also evident in Fig. 4.5, indicates that as muscles fatigued, the connections in the motor network decreased.

Eccentricity

The primary sensory area was the major node in the first window, while the cerebellum was the major node in the second and third windows. This is schematically represented in Fig. 4.5 where the major nodes are marked in black. This result indicates that S1 wielded

maximum influence on the network in the first window, and the dominance of influence shifted to the cerebellum in the second and third windows.

Table 4.1 Cluster-in and cluster-out coefficients for all ROIs for the three windows

		M1	SMA	PM	S1	C	P
Window-1	C_{in}	19	15	7	9	16	11
	C_{out}	8	13	7	25	10	13
Window-2	C_{in}	15	21	15	9	16	8
	C_{out}	8	14	11	23	18	10
Window-3	C_{in}	11	13	9	9	15	8
	C_{out}	7	8	9	18	14	9

Discussion

The results presented above reflect a gradual shift in connectivity patterns across brain regions during the course of prolonged motor task. During the first time window, the network is highly interconnected as illustrated by Fig. 4.5. A high value of C_{in} for M1 and C_{out} for S1 indicates that the neural network is predominantly driven by feedback mechanisms from the primary sensory cortex. This pattern is consistent with the fine tuning of motor responses with sensory feedback (Solodkin *et al*, 2004). Furthermore, we know that all regions drive the primary motor cortex through both direct (SMA, premotor cortex) and indirect (parietal, cerebellum) anatomical pathways (Passingham, 1988; Strick *et al*, 1999). Structural equation modeling by Solodkin and colleagues (2004) found that the primary sensory cortex weakly drove the primary motor cortex, but did not exert causal influence on other brain regions. However, our results suggest that S1 could have a strong causal influence on M1. The fact that neither C_{in} nor C_{out} dominates each other for the cerebellum and parietal areas points to the existence of bidirectional

connections between these ROIs and the rest of the network and hence the possibility of both top-down and bottom-up mechanisms of influence.

As the motor task progresses into the middle temporal window, regions that guide motor performance – the cerebellum, SMA, and premotor cortex – become more prominent as indicated by their elevated clustering coefficients as compared to those in the first window. These regions are collectively responsible for timing motor responses, response preparation, and sequencing responses (Passingham, 1988; Ivry *et al*, 1989; Deiber *et al*, 1991; Tanji, 1996; Gordon *et al*, 1998). While S1 is the major node in the first window, the cerebellum becomes the major node in the middle window. This shift in the role of the nodes in the network suggests that participants have mastered the motoric components of the task and are now primarily focused on orchestrating these responses. The shift from the primary sensory cortex to cerebellum also implies that participants are less reliant on tactile feedback to guide performance.

The network changes yet again during the final stages of the experiment, but this shift is more subtle than before. The network structure is largely consistent between the middle and last windows. Most striking is the change in *magnitude*; the causal strength of all connections as well as the clustering coefficients decreases. Whereas the middle window most likely reflects learning (manifesting as both the strengthening and paring of connections), the last window only shows the weakening of connections. These results are consistent with fatigue, which we have previously demonstrated to reduce interhemispheric connectivity (Peltier *et al*, 2005a). Although the neural network optimized during the middle window remains largely intact, the interregional causal strengths diminishes as fatigue takes its toll.

The nodes in the network considered here are not intended as an exhaustive account of regions mediating motor behavior. Only the neural regions demonstrating the most significant activation were examined. Thus, subcortical regions such as the basal ganglia and red nucleus were not addressed despite their influence on motor performance (Harrington *et al*, 1998; Liu *et al*, 1999). Likewise, thalamic activity was not modeled, even though most of the corticocortical, corticocerebellar and cerebellocortical anatomical pathways are routed through the thalamus (Jones, 1999).

Besides supporting the existing hypothesis on the neural effects of muscle fatigue, our model demonstrates gradual changes in neural communication patterns in the prolonged motor task. We propose that these changes reflect slowly varying neurophysiological alterations caused by fatigue. In addition to obviating the effect of the hemodynamic response on the predictive model, our use of summary measure enabled us to match the temporal scale of analysis with the temporal scale at which the underlying physiology is likely to evolve.

Since the resulting networks have a complicated topology, a manual perusal of every connection and their interpretation is untenable. Therefore we have employed graph theoretic concepts to unearth possible patterns of communication in the network. This approach gives useful insights about the changes in the connectivity patterns and the contribution of individual and specific groups of ROIs to network behavior. Although we have used only clustering and eccentricity to characterize network topology, several other options exist within the framework of graph theory such as connected components and path length analyses (Skiena, 1990) which could potentially be used to characterize the network.

Apart from integrating coarse temporal scale analysis and graph theoretic concepts with multivariate Ganger causality, we introduced some modifications to the existing literature on multivariate Granger causality analysis which are noteworthy. Unlike previous EEG applications of DTF (Kus *et al*, 2004), we did not normalize the DTF values with respect to the inflows at each node. Normalization makes the value of DTF dependent on the inflow at each node, and hence DTF values corresponding to connections not involving the same receiving node cannot be compared since the inflows into different nodes may be different. While normalization provides an intuitive appeal by rendering the DTF values in the range (0,1), it makes comparisons between connections untenable and the study of dynamic evolution difficult.

Nonlinear Granger Causality

The linear and nonlinear Granger maps for the three subjects after the removal of baseline drift is as shown in Fig. 4.6. Note that these maps are not thresholded. It can be seen that there is drive from the SMA to the primary motor area and pre-motor area. This result is in agreement with previous studies (Abler *et al*, 2006). Also, it is interesting to note that the linear and nonlinear maps are very similar. Fig. 4.7 shows the corresponding Granger maps without the removal of baseline drift. It can be seen that the linear maps are distorted while the nonlinear maps retain the original pattern. In addition, artifacts appear due to CSF which seems to drive SMA. We know that CSF oscillations are not metabolic in origin (Obrig *et al*, 2000) and hence the drive from CSF to SMA is artifactual. From these results, we conclude that while nonlinear Granger causality gives results very similar to the liner model, it is more robust to artifacts caused by baseline drift.

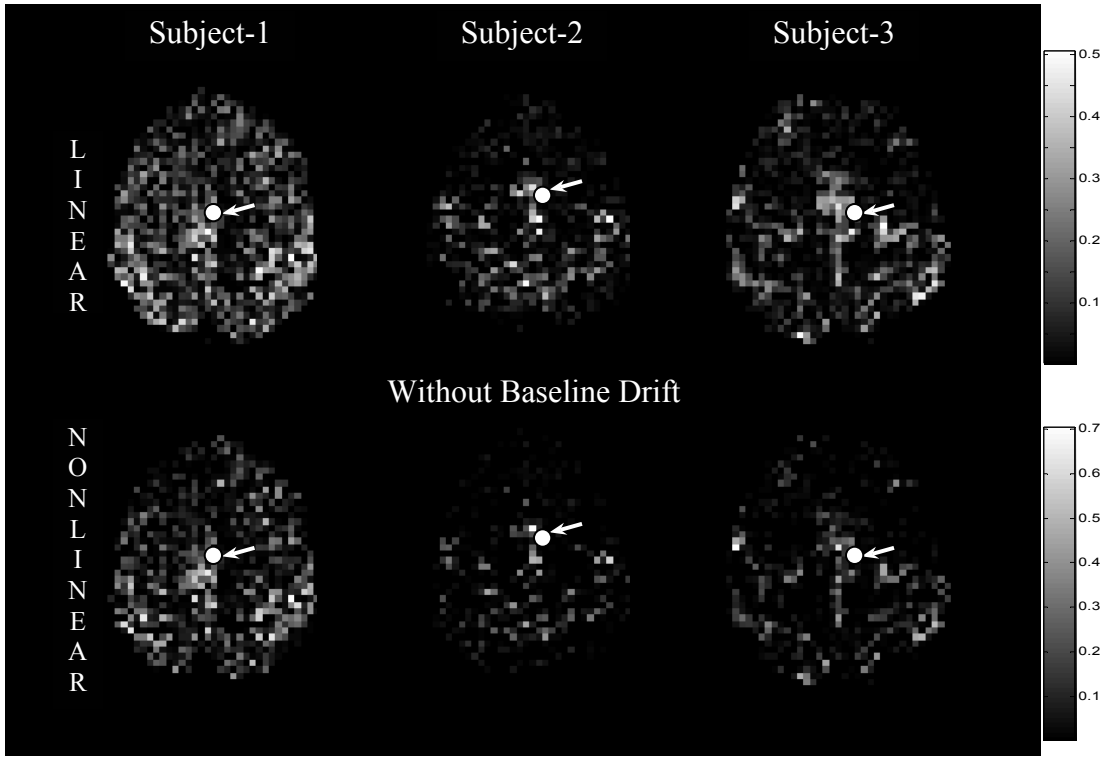

Figure 4.6 Linear and nonlinear Granger causality maps with the removal of baseline drift. White arrow indicates the seed region

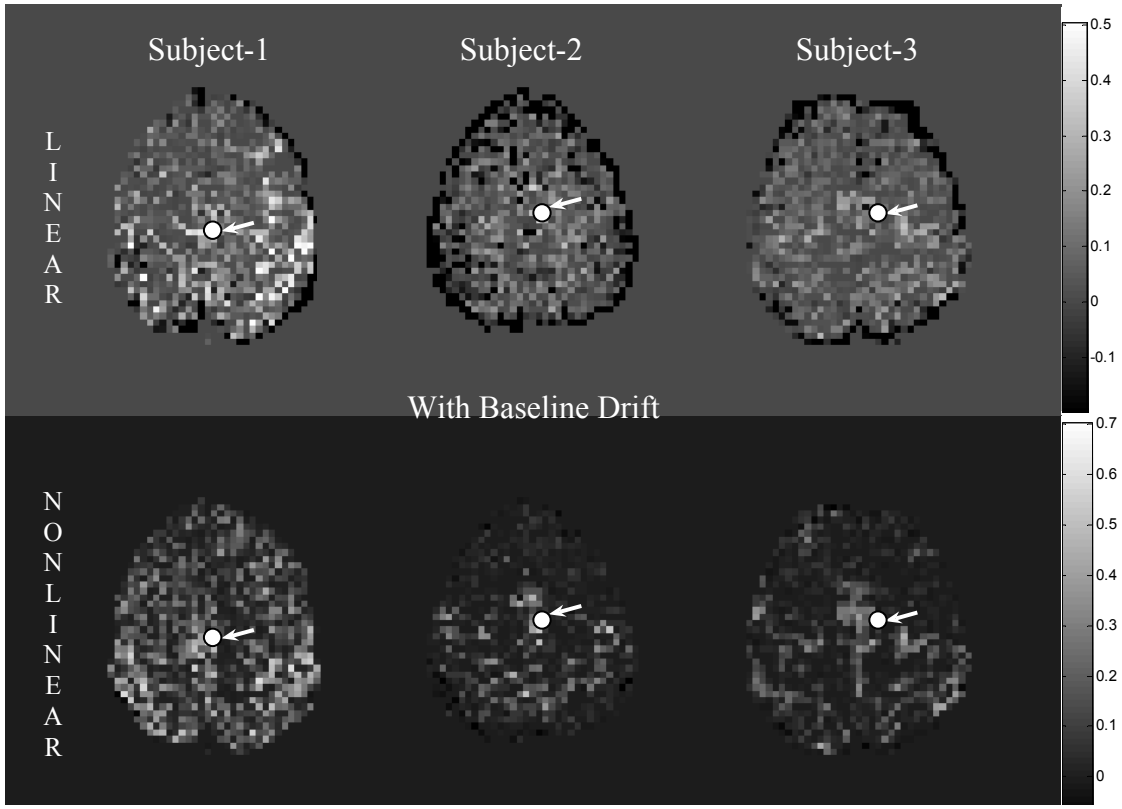

Figure 4.7 Linear and nonlinear Granger causality maps *without* the removal of baseline drift. White arrow indicates the seed region

Conclusions

In this work, we have discussed the linear and nonlinear Granger models of effective connectivity. First, we demonstrated the utility of an integrated approach involving multivariate linear Ganger causality, coarse temporal scale analysis and graph theoretic concepts to investigate the temporal dynamics of causal brain networks. Multivariate granger causality allowed us to factor in the effects of all relevant ROIs simultaneously. The coarse temporal scale analysis obviated the effect of the spatial variability of the hemodynamic response on prediction and permitted us to study slowly varying neural changes caused by fatigue. Subsequently, by applying graph theoretic concepts, we obtained an interpretable characterization of the complicated network topology. We believe that our integrated approach is a novel contribution to the effective connectivity analysis of functional networks in the brain. Application of this approach to motor fatigue data revealed the dynamic evolution of the motor network during the fatigue process and reinforced the notion of fatigue induced reduction in network connectivity. Finally we showed that the results obtained from nonlinear Granger models were akin to the linear ones. However, the nonlinear model was shown to be more robust to artifacts such as baseline drifts as compared to the linear model.

CHAPTER 5

CONNECTIVITY IN LOCAL NETWORKS

Introduction

Functional connectivity (Friston, 1993) between anatomically distributed regions of the brain in resting-state has been well studied using neuroimaging techniques including fMRI. Most functional connectivity studies focus on connectivity between different regions in networks. On the other hand, local coherence carries information regarding localized coordination among neighboring neuronal units and is dependent on the local anatomic structure and homogeneity of neuronal processes. This aspect has been investigated recently by a regional homogeneity (ReHo) measure (Zang *et al*, 2004) derived using Kendall's coefficient of concordance (KCC) (Kendall *et al*, 1990; Baumgartner *et al*, 1999). In their study, Zang *et al.* found significant changes in ReHo in a finger tapping experiment. In a more recent study, Kriegeskorte *et al* showed that improved functional activation maps could be obtained using an information-based approach incorporating the local functional homogeneity but avoiding spatial smoothing (Kriegeskorte *et al*, 2006).

Methodologically, previous studies of local coherence utilized predefined neighborhoods, making the result explicitly dependent on the neighborhood size and implicitly on the spatial resolution. In this work, we introduce a general approach to characterizing local brain coherence by defining a metric, integrated local correlation (ILC), which is the integration of the spatial correlation function for each voxel. In principle, the integration does not require the specification of a finite neighborhood. In

practice, the spatial correlation function becomes negligible beyond the 25-43 mm limit of 'local scale' defined by Bellec *et al* (Bellec *et al*, 2006) except in cases of distributed networks, which were discussed in the previous chapters. Therefore, for the practical implementation of ILC calculation, only a finite neighborhood needs to be considered. While the spatial correlation function for a voxel is a continuous function in principle, it can only be measured discretely in practice at the acquired image resolution. This is a potential problem for ReHo (Zang *et al*, 2004) KCC is dependent on ranking, which is sensitive to the number of voxels in the neighborhood, and hence indirectly dependent on resolution. This problem is negligible for ILC because the integration of the entire correlation function with respect to the physical dimensions is not expected to depend on the sampling resolution significantly.

Resting-state fluctuations in fMRI have gained significant interest because they are thought to carry vital physiological information. In fact, low frequency correlation between distributed regions is being extensively used in examining functional connectivity in networks (Biswal *et al*, 1995, 1997; Lowe *et al*, 1998; Cordes *et al*, 2000; Peltier *et al*, 2003; Hampson *et al*, 2002). Therefore, local coherence in resting state may provide an added measure for understanding the brain. To demonstrate that ILC is a meaningful measure, we examined its tissue specificity and reproducibility in resting state fMRI data. To demonstrate that ILC does not arise primarily from fluctuations due to heart beat and respiration, we also compared ILC derived with and without the removal of physiological noise. Our results show that ILC is tissue-specific, reproducible, has functional relevance, and not greatly influenced by physiological fluctuations. Comparing ILC maps obtained from resting state and a continuous motor task revealed

reduced local coherence in the default mode network during the task thereby demonstrating the utility of ILC for differentiating experimental conditions. Finally, we compared ILC and regional homogeneity (ReHo) by examining their ability to discriminate between gray and white matter in resting state data and found ILC to be more sensitive.

ILC is the integration of the spatial correlation function which is derived based on a linear model. However, it is also of interest to investigate nonlinear connectivity in local networks. To achieve this objective, we extended the concept of phase-space reconstruction introduced in the previous chapters to perform a spatial embedding in the local neighborhood of a voxel. By estimating the spatial largest Lyapunov exponent (SLLE) from the spatially embedded data (Gonzalez *et al*, 2000), we obtained an estimate of the coupling in the local neighborhood. The utility of spatial embedding has been debated in literature, for example in the estimation of correlation dimension of EEG (Pritchard *et al*, 1996, 1999; Pezard *et al*, 1999), but nevertheless its utility has been demonstrated in the analysis of schizophrenic patients using EEG (Lee *et al*, 2001). Moreover the formulation by Gonzalez is very general in nature and presents itself nicely for application to fMRI data.

Finally, we illustrate the neuroscientific utility of local coherence by probing the neurophysiological effects of varying concentrations of the anesthetic agent sevoflurane. The loss and recovery of consciousness and their corresponding neural substrates is the central conundrum in anesthesiology. Network models (Crick *et al*, 2003; Mashour, 2004) attribute the loss of consciousness induced by anesthesia to cognitive unbinding resulting from reduced connectivity of distributed functional networks in the brain.

Accordingly, functional neuroimaging studies have indicated disruption of functional connectivity in thalamo-cortical networks (Ries *et al*, 1999; White *et al*, 2003), inter-hemispheric cortico-cortical networks (Peltier *et al*, 2005) and in the default mode network (Peltier *et al*, 2006) as a result of anesthetic sedation. The "dynamic core hypothesis" hypothesizes a dynamic core network comprising of the limbic system, the thalamo-cortical pathway and the frontal cortex (Tononi *et al*, 1998) to be crucial in mediating alterations of consciousness. According to this hypothesis, consciousness is an emergent phenomenon arising from a resonance between the activity within individual regions and that with the other regions of the dynamic core network. In the light of the above hypotheses, it is important to investigate the local coherence of neural sub-systems in addition to their distributed connectivity with other sub-systems in order to understand the cortical effects of anesthesia. In this work we investigate this aspect by examining the local coherence of the default mode network during graded sedative states induced by varying concentrations of sevoflurane in healthy subjects.

Methods

Integrated Local Correlation

Definition and Calculation of ILC

With local coherence attributed to physical proximity, the temporal correlation of a given pixel with its neighbors is a function that decreases with distance and can be used to characterize the local coherence. In this work, the spatial correlation function is integrated, giving rise to integrated local correlation or ILC, to characterize local

coherence. In the 2-dimensional case considered here, ILC reflects the volume under the spatial correlation function. Given that our measurement of the correlation function is discrete and truncated, it is desirable for any measure of local coherence to be independent of discretization and truncation. Although the definition of ILC suggests this independence, it needs to be experimentally verified. Discretization is dictated by the finite spatial resolution of image acquisition. If the correlation function is sufficiently smooth, the ILC obtained should be independent of the spatial resolution. This hypothesis is tested experimentally with data obtained at two spatial resolutions.

Even though we have considered the 2-dimensional (2D) case in this report, ILC could theoretically be extended to the 3-dimensional (3D) case if we have contiguous slices. These voxels would not need to be isotropic based on our demonstration of insensitivity to voxel size. However with multi-slice imaging, issues of imperfect slice profile and slice timing would have to be considered and may make the ILC calculated in 3D more complicated.

Data Acquisition

In the first experiment, echo planar imaging (EPI) data was obtained from a phantom containing a solution of 3.75 g $NiSO_4$ and 5 g NaCl in 1000 g H_2O, using a 3.0 T Siemens Trio scanner. The scan parameters were: repetition time (TR)= 750 ms, echo time (TE)= 34 ms, flip angle (FA)= 50°, field of view (FOV)= 22 cm, 5 slices with a thickness of 5 mm, 280 volumes per slice and an in-plane resolution of 3.44×3.44 mm^2.

In experiment 2, resting state EPI runs were obtained in three healthy subjects while they were instructed to keep their eyes open, fixate on a central cross, and not

engage in any mental activity. Three consecutive scans were performed with parameters similar to those used in the phantom experiment: TR= 750 ms, TE= 34 ms, FA= 50°, FOV= 22 cm, 10 axial slices 5 mm thick covering the section between the corpus collusum and the top of the brain, 280 volumes per slice and an in-plane resolution of 3.44×3.44 mm^2. In addition, a high resolution resting-state scan was also performed with an in-plane resolution of 2×2 mm^2 and other EPI parameters matched to the first three scans. T1-weighted anatomical images with 1 mm isotropic resolution were acquired using a magnetization prepared rapid gradient echo (MPRAGE) sequence (Mugler *et al*, 1990) with TR/TE = 2600/3.93 ms and FA=8°.

In the third experiment, resting-state data (in-plane resolution of 3.44×3.44 mm^2) were acquired in three subjects using the scan parameters described above, with the difference that only 5 slices were acquired. These slices started at the top of the brain with a voxel size of $3.44 \times 3.44 \times 5$ mm^3. A pulse-oximeter and nasal respiratory cannula were used during data acquisition to obtain cardiac and respiratory pulsations, respectively. T1-weighted axial anatomical images were acquired in the same slices at an image resolution of 512×512 using a spin-echo sequence (TR=534 ms, TE=8.6 ms and FA=90°).

In the fourth experiment, EPI data were acquired in three healthy volunteers with a paradigm consisting of three minutes of a fixation condition (resting state) followed by three minutes of a continuous motor task which required the subjects to continuously perform bimanual finger opposition. The finger opposition was paced at 1 Hz by a number (1, 2, 3 or 4) visually presented, indicating which digit to oppose against the thumb. Scan parameters were: TR= 750 ms, TE= 34 ms, FA= 50°, FOV=22 cm. The

volume imaged consisted of 10 axial slices 5 mm thick covering the section between the bottom of the corpus collusum and the top of the brain. The resting and task periods each consisted of 280 time points. In addition, T1-weighted anatomical images with 1 mm isotropic resolution were acquired using an MPRAGE sequence (Mugler *et al*, 1990) with TR/TE = 2600/3.93 ms and FA=8°.

Data Analysis

The operational procedure for calculating ILC is as follows. Motion correction and slice scan time correction was performed**.** Subsequently**,** detrending was applied to each voxel time series to remove baseline drift. For each voxel in the image, a two dimensional correlation function corresponding to its temporal correlation with neighboring voxels was calculated and integrated to obtain ILC as given in the equation below.

$$ILC(\vec{s}) \cong \sum_{x}\sum_{y} \frac{\sum_{n=0}^{N-1}[a_{\vec{s}}(n).b_{xy}(n)]}{\sqrt{\sum_{n=0}^{N-1}[a_{\vec{s}}(n)]^2 . \sum_{n=0}^{N-1}[b_{xy}(n)]^2}} \tag{5.1}$$

where $\vec{s}$ is the position of the voxel under consideration and $a_{\vec{s}}(n)$ is the time course for that voxel. $b_{xy}(n)$ represents all other neighboring voxels where x and y span the dimensions of the neighborhood. ILC was calculated only for those voxels for which the neighborhood used for the calculation was contained within the image. In addition, as described below, a correction to account for system inherent correlation was determined and applied to the resultant ILC. The ILC was calculated for every voxel in the image to

form ILC maps. The anatomical images were manually segmented into gray matter and white matter using MRIcro (Rorden *et al*, 2000), a freely available medical image processing software package (http://www.sph.sc.edu/comd/rorden/ mricro.html). The segmented images were down-sampled to match the EPI resolution and separate gray matter and white matter masks were obtained and used in assessing the tissue-specificity of ILC.

Characterization of ILC

Inherent correlation in fMRI data and its correction

It is possible that fMRI data contains inherent correlation due to the image acquisition and reconstruction processes. To ascertain the possible inherent correlation in the data and its effect on ILC, the spatial correlation function of the phantom data and the corresponding ILC maps were obtained and examined. Furthermore, the distribution of the phantom ILC was compared to that of a simulated independent Gaussian random field with matching standard deviation using the Wilcoxon rank sum test. It was found that the inherent correlation was small but could not be ignored. To compensate for this effect, the spatial correlation function of the phantom, obtained by averaging the correlation function of all voxels in the phantom, was subtracted from the spatial correlation function of each pixel in the human brain data before ILC calculation.

Discretization and Truncation

To investigate the effect of resolution on the calculated ILC, we used the high resolution EPI data with the matrix size of 128 × 128. The in-plane resolution for this

data set was 2 × 2 mm^2. To obtain ILC maps calculated with low resolution images, the k-space data of the high-resolution images was truncated to a 64 × 64 matrix, zero padded to 128 × 128, and inverse Fourier transformed to form an image that had a resolution of 4 × 4 mm^2 but a matrix size of 128 × 128. This image was divided into four non-overlapping, 64 × 64 sub-images using the simple sub-sampling scheme shown in Fig. 5.1. Each of these sub-sampled images was used to calculate an ILC map, using a neighborhood that has the same physical size as that used for the high resolution image. The resultant maps were combined by reversing the down sampling process, providing a 128 × 128 ILC map for comparison of mean ILCs in gray matter and white matter ROIs. Note that this process allowed us to calculate the ILC map with low resolution images and to perform the comparison at the same high resolution. To examine the effect of truncation, the above process was repeated for neighborhood sizes ranging from 12 × 12 mm^2 to 68 × 68 mm^2 (corresponding to 3 × 3 to 17 × 17 low resolution voxel neighborhoods).

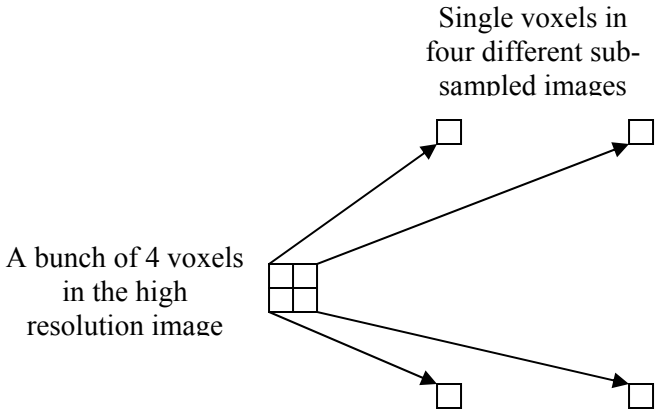

Figure 5.1 A schematic illustrating the sub-sampling scheme used to derive low resolution images from high resolution data

Effect of Physiological Noise

The effect of cardiac and respiratory pulsations on fMRI data has been extensively studied (Hu *et al*, 1995; Kruger *et al*, 2001; Deshpande *et al*, 2006). To test the effect of physiological fluctuations, data from experiment 3 were analyzed with and without physiological noise correction using a retrospective technique (Hu *et al*, 1995). ILC maps were obtained before and after the correction and the significance of the difference was ascertained.

Tissue-specificity

Gray matter and white matter masks were obtained as described in the data analysis section and used to obtain mean ILC values for the gray matter and white matter, respectively. In addition, the ILC maps were up sampled to the resolution of the anatomical image and overlaid on it.

Regional ILC Differences in Gray Matter

Using EPI data obtained from the three subjects in the second experiment, the mean ILC value of gray matter for each of the three runs was calculated. The statistical significance of the difference between the ILC value of each voxel and the gray matter mean ILC was ascertained and displayed as a statistical parametric map. For every subject, the T_1-weighted anatomical images and the statistical parametric maps were spatially transformed to MNI space. The voxels common to the statistical parametric maps from all three runs were overlaid onto that subject's anatomical image for display.

Reproducibility

fMRI data obtained from repeated resting-state runs in the second experiment was used to test the reproducibility of the tissue-specific pattern in 3 healthy subjects. ILC maps were obtained for all three runs, and the correlation coefficient between them was ascertained to assess reproducibility (Strother *et al*, 1997).

Differentiating Experimental Conditions

ILC maps were generated for the resting state (condition 1) and continuous motor (condition 2) separately and the difference between the maps of the two conditions was obtained to assess changes in local coherence. It has been reported that the default mode network is deactivated during the performance of an explicit task as compared to resting state (Raichle *et al*, 2001). Based on this, the difference maps may highlight this network.

Comparison of ILC and ReHo

We performed an explicit comparison of ILC with ReHo by evaluating their tissue specificity and within tissue variance. ILC and ReHo (Zang *et al*, 2004) maps were calculated from the data obtained in the second experiment. Histograms of ILC and ReHo maps were plotted and the statistical significance of the difference between their gray matter and white matter distributions was ascertained. The ability of ILC and ReHo to differentiate between the tissues demonstrates their sensitivities to fMRI physiology and neural processing in the tissues (Deshpande *et al*, 2006; Kruger *et al*, 2001).

Statistical Significance Testing

We subjected the gray matter and white matter ILC distributions to a Jarque-Bera test for goodness-of-fit to a normal distribution (Jarque *et al*, 1980) and found that the distributions were not normal (at 95% significance). Hence we employed the non-parametric Wilcoxon rank sum test (Wilcoxon, 1945) to test for the significance of the difference in tissue specific ILC distributions. This test was employed before and after physiological correction, and for high and low resolution data. For testing the significance of the difference between ILC values of each voxel and the gray matter mean ILC, the gray matter distribution was ascertained. Subsequently, the position of the ILC value of every voxel in the corresponding gray matter distribution was calculated. In order to estimate the p-value of each voxel's ILC, the fraction of gray matter voxels with ILC above it was ascertained. This procedure was adopted instead of the t-test since the gray matter distributions were not normal.

Application to Anesthesia

Data Acquisition

Six right-handed volunteers took part in this study which was approved by the internal review board at Emory University. The study was designed to monitor the graded effects of anesthesia in three states: awake, deep and light anesthesia, in that order. This was achieved by administering 0%, 2% and 1% end-tidal sevoflurane, respectively. The awake state corresponded to a normal resting state scan without anesthesia. The volunteers gargled with 4% viscous lidocaine prior to anesthesia. Single breath technique with sevoflurane in oxygen was used to administer anesthesia (Peltier *et al*, 2005). For

achieving the deep anesthetic state, a laryngeal mask airway was placed with sevoflurane concentration held constant for 15 minutes at 2%. The scans corresponding to the deep state were obtained after brain equilibration was established. Subsequently, the same procedure was repeated with 1% sevoflurane corresponding to the light anesthetic state. Resting state EPI data were acquired on a 3T Siemens Trio for each of the three states. The pulse sequence parameters were: TR= 750 ms, TE= 35 ms, FA= 20°, FOV= 22 cm, 10 axial slices with 5 mm slice thickness, 280 volumes per slice and an in-plane resolution of 3.44mm × 3.44 mm. In addition, T_1-weighted anatomical images with 1 mm isotropic resolution were acquired using a magnetization prepared rapid gradient echo (MPRAGE) sequence with TR/TE = 2600/3.93 ms and FA=8°.

Data Analysis

The motion parameters for all the subjects were reviewed using Brainvoyager™ 2000 (Ver 4.9 © Rainer Goebel and Max Planck Society, Maastricht, The Netherlands. www.brainvoyager.com). One subject was excluded from the analysis due to gross head motion at the beginning of the scan. In the remaining subjects, the regions corresponding to the default mode network were identified in the resting awake state using independent component analysis (ICA) (Greicius *et al*, 2004) and a mask formed. The resting state default mode mask was transformed into MNI (Montreal Neurological Institute) space (Evans *et al*, 1993). The default mode masks in the deep and light states were generated by transforming the mask in the MNI space to the native EPI space of deep and light states, respectively. The transformations between EPI and MNI space were carried out

using SPM2 (Wellcome Department of Cognitive Neurology, London, UK; http://www.fil.ion.ucl.ac.uk).

ILC maps were generated by calculating ILC values corresponding to each voxel within the brain. This procedure was carried out in the native EPI space of the data. The ROI specific ILC values for the default mode network regions - posterior cingulate cortex (PCC), dorsal anterior cingulate cortex (dACC), inferior parietal cortex (IPC) and frontal cortex (FC) - were derived by applying the default mode masks to the ILC maps and calculating the mean ILC values within each ROI. Within each default mode mask, the four ROIs were discriminated based on the evidence of their anatomical location. The frontal ROI consisted of medial and lateral prefrontal regions. The statistical significance of the change in ILC values from awake to deep state and that from deep to light state was ascertained by performing a Wilcoxon rank sum test (Wilcoxon, 1945) between the sample ILC values of each ROI in different states. The non-parametric Wilcoxon rank sum test was employed instead of the t-test since ILC distributions were found to be not normal. It is to be noted that the significance of the change in ILC was calculated for the state transitions that were embedded in the experimental design.

Spatial Largest Lyapunov Exponent

The principle of phase space reconstruction was introduced in Chapter 3 for obtaining estimates of nonlinear connectivity from the joint embedding of fMRI time series. In this chapter, we adopt the same concept of embedding to reconstruct the joint dynamics of multiple fMRI time series in a voxel's neighborhood. However, to obtain the connectivity between multiple time series (unlike bivariate time series in the third

chapter) we measured the divergence rates of nearby orbits in the phase space. This was accomplished by computing Lyapunov exponents. Usually the largest Lyapunov exponent is sufficient to infer the divergence (Kantz *et al*, 1997). For periodic systems, the Lyapunov exponent is zero, is negative for deterministic systems and infinity for a completely stochastic system. However, for systems with deterministic coupling it is a low positive value.

In the following sections, we elucidate the procedure for calculating Lyapunov exponents and suggest a coupled map lattice model to validate the viability of the method for detecting local connectivity.

Computation of SLLE

This section presents an overview of the procedure to compute SLLE. For an *I*-dimensional dynamical system, *I* Lyapunov exponents exist, which was obtained from the Eigen values of the matrix

$$\beta = \lim_{n \to \infty} \left[P(n)^T \bullet P(n) \right]^{1/2n} \tag{5.2}$$

where *P(n)* corresponds to the product of the first '*i*' Jacobians computed along the phase space trajectories (Gonzalez *et al*, 2000) and $(\ )^T$ denotes the matrix transpose. The phase space trajectories were obtained by embedding the fMRI time series in a voxel's neighborhood. The embedding procedure is similar to the one described in Chapter 3. The Lyapunov exponents were defined as the logarithms of the Eigen values β. The largest of the Lyapunov exponents was defined as SLLE.

Coupled Map Lattice Model

Even though we have a broad understanding of low dimensional nonlinear systems (Kantz *et al*, 1997), there is not enough literature on high dimensional spatially extended systems. The addition of a spatial extent to the dynamics produces a complex interplay between the dynamics of individual units and the spatial interactions. The individual units may be discrete or continuous in space. A typical model in the latter case (if time is also continuous) is described by partial differential equations . By discretizing space we obtain a lattice of ordinary differential equations. In the discrete space case, the system can be viewed as a collection of low dimensional dynamical systems coupled together via some spatial rule (Bunimovich, 1995). Examples of this kind of model are widespread in the literature, particularly in the field of solid-state physics where they are used to study the dynamics of interacting atoms arranged in a lattice (Poggi *et a*l, 1997). Here we focus on a third category of extended dynamical systems where not only space but also time is discrete. In such a case the model consists of low dimensional dynamical units with discrete time, arranged in some discrete lattice configuration (Kaneko, 1984) in one or more spatial dimensions. Such models are usually called coupled map lattices (CMLs) as shown in Fig 5.2. We propose to adopt such a model for the fMRI data obtained in a local neighborhood of a voxel.

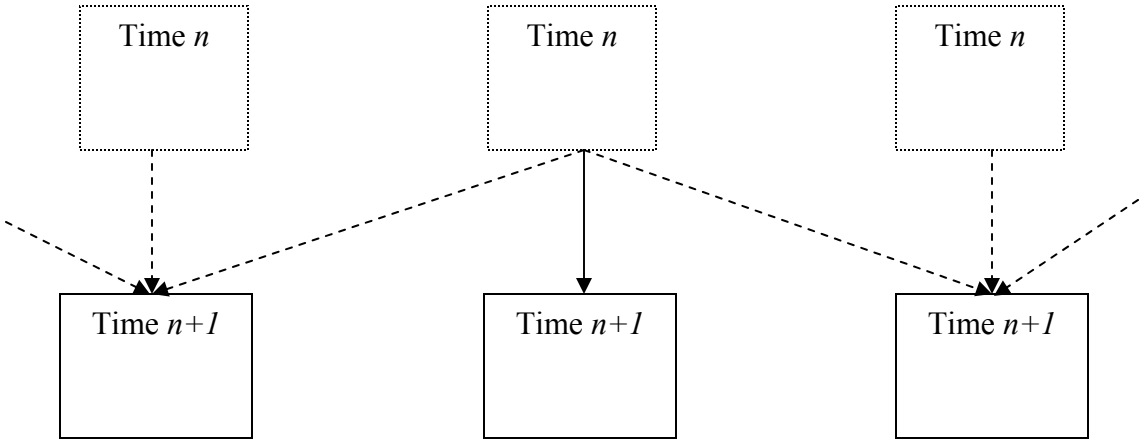

Figure 5.2 A Coupled map lattice model for representing the spatio-temporal dynamics of fMRI

Model Validation Using a Simulated CML and Application to Resting State Data

For simplicity, consider an array of I number of sites (a voxel location in case of fMRI data). At the j^{th} site a discrete time local dynamical unit is introduced whose state at time n is denoted by x_j^n. We assume that all the spatial units are alike. In the simplest case, the local variable x_j^n is taken to be one-dimensional. The dynamics of the CML is then a combination of the local dynamics of individual units and the coupling between the units which is represented by the weighted sum over some spatial neighborhood. The time evolution of the j^{th} variable is thus given by

$$x_j^{n+1} = \sum_k \varepsilon_k f(x_{j+k}^n) \tag{5.3}$$

where f is the coupling function and the range of summation defines the neighborhood. The coupling parameters ε_k are site independent, and satisfy $\Sigma\varepsilon_k=1$. The common choice for the coupling scheme is (Gonzalez *et al*, 2000)

$$x_j^{n+1} = (1-\varepsilon) f(x_j^n) + \frac{\varepsilon}{2}\left[f(x_{j-1}^n) + f(x_{j+1}^n) \right] \tag{5.4}$$

The coupling parameter ε is constrained by the inequality $0<\varepsilon<1$, to ensure that the signs of the coupling coefficients in Eq. 5.4 (i.e., $\varepsilon/2$ and $(1-\varepsilon)$) remain positive. As in Gonzalez *et al*, we used a lattice of size *I=20* and *f(x)=4x(1-x)* with coupling strength ε =0.4. Finally, the Lyapunov exponents were calculated from this simulated system for varying coupling strengths.

Subsequent to validation of the model, SLLE was computed separately for gray matter and white matter regions from the resting state data obtained from healthy volunteers (data acquisition details discussed in the previous section).

Results and Discussion

Integrated Local Correlation

Inherent correlation in fMRI data and its correction

The average spatial correlation functions for the phantom and the brain tissue, respectively, are shown in Fig. 5.3. A re-scaled version of the phantom spatial correlation function is depicted in Fig. 5.4 which shows the *sinc* modulation in the read-out direction. This is likely the result of inherent filtering caused by the interpolation of data sampled on the readout gradient ramps in the EPI sequence. In EPI, a finite time is needed to switch the readout gradient from the positive value to the negative value. Sometimes, as is the case here, data are sampled on the ramps and interpolation has to be performed in the k-space during image reconstruction, leading to the *sinc* modulation in Fig. 5.4.

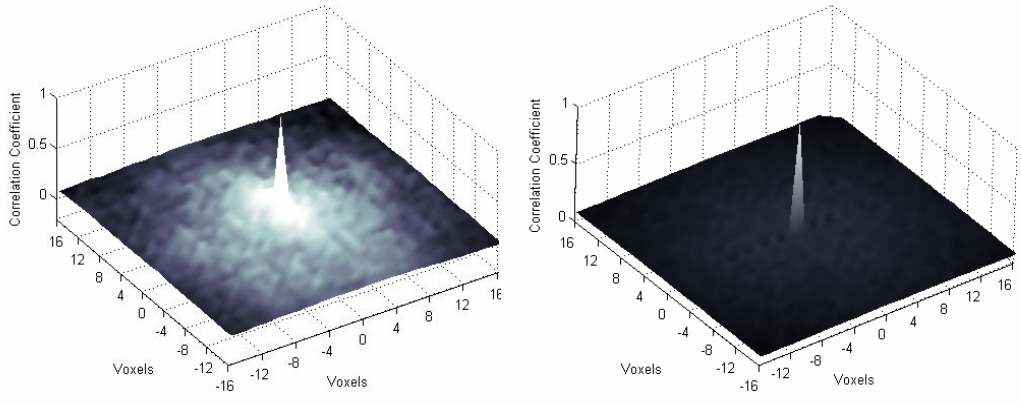

Figure 5.3 Mean spatial correlation functions. Left: brain tissue. Right: EPI phantom

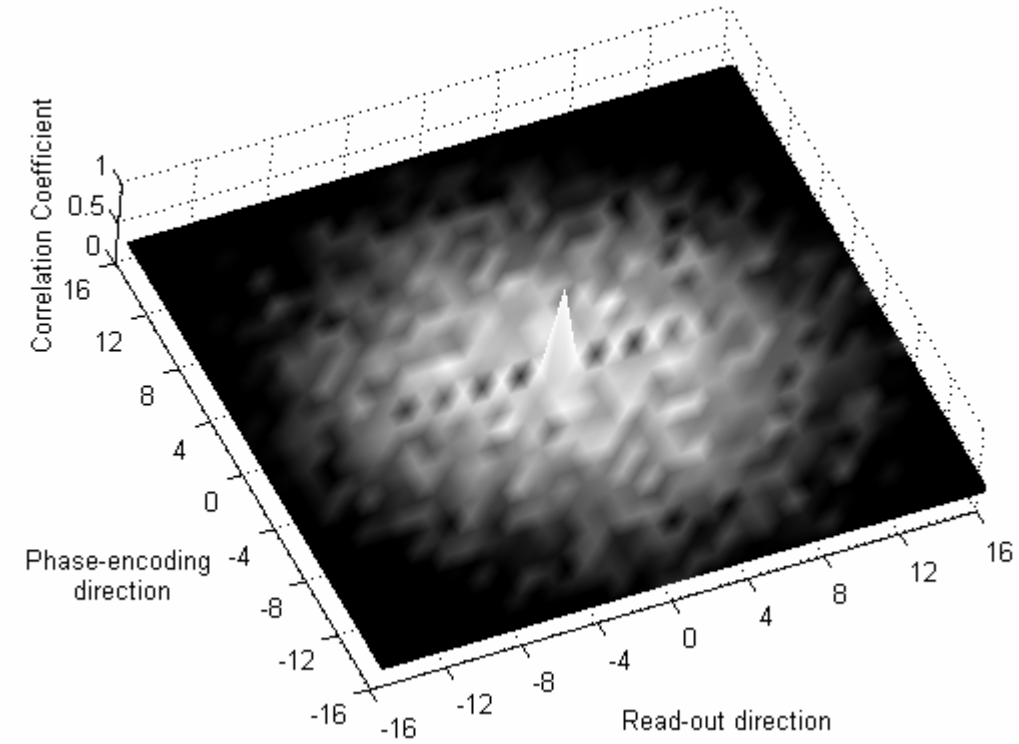

Figure 5.4 Re-scaled spatial correlation function of the phantom showing sinc-modulation in the read-out direction. The original scale (0, 1) is compressed to (0, 0.04) in this figure

The ILC map for the phantom is shown in Fig. 5.5. Although the mean value of phantom ILC is substantially less than that of brain tissue, the distribution of phantom ILC is significantly different from the null distribution (Fig. 5.6), indicating non-negligible inherent correlation. Therefore we subtracted the average spatial correlation function of the phantom from the spatial correlation function of the brain tissue pixels before calculating ILC.

Figure 5.5 Left: EPI phantom image obtained with parameters matched to in vivo data Right: ILC image of EPI phantom plotted on a matched scale

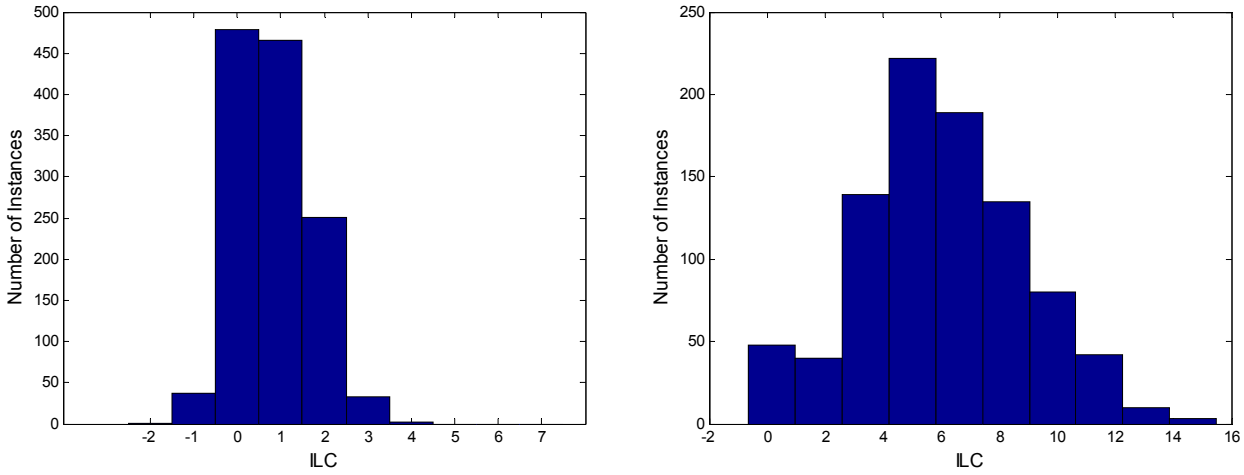

Figure 5.6 Left: ILC null distribution obtained from Gaussian noise matched to the phantom noise level. Right: ILC distribution obtained from the phantom

Discretization

As we explained in the introduction, a major advantage of the ILC method is its independence of the image resolution. Table 5.1 lists the mean gray matter and white matter ILC values calculated by using high and low resolution images. The Wilcoxon rank sum test shows that there is no significant difference between the two resolutions.

Table 5.1 Mean ILC values of gray matter and white matter for high and low resolution data

Subject	Gray Matter			White Matter		
	High Resolution	Low Resolution	p-value	High Resolution	Low Resolution	p-value
1	21.8	21.6	0.7	6.1	6.0	0.7
2	20.5	20.3	0.4	7.9	7.6	0.3
3	23.6	23.2	0.8	7.4	7.2	0.6

Truncation

Fig. 5.7 plots the ILCs, calculated with low and high resolution images, respectively, versus the neighborhood size used. It can be seen that the ILC plateaus at 52×52 mm^2, indicating that correlation beyond this distance is negligible, which is in agreement with a recent work (Bellec *et al*, 2006). This result also indicates that for the calculation of ILC, as long as a sufficiently large neighborhood is used, the result is independent of the neighborhood size. In this work, we employed a 60×60 mm^2 neighborhood. Also, the high and low resolution curves follow each other closely, reinforcing the fact that ILC is independent of image resolution.

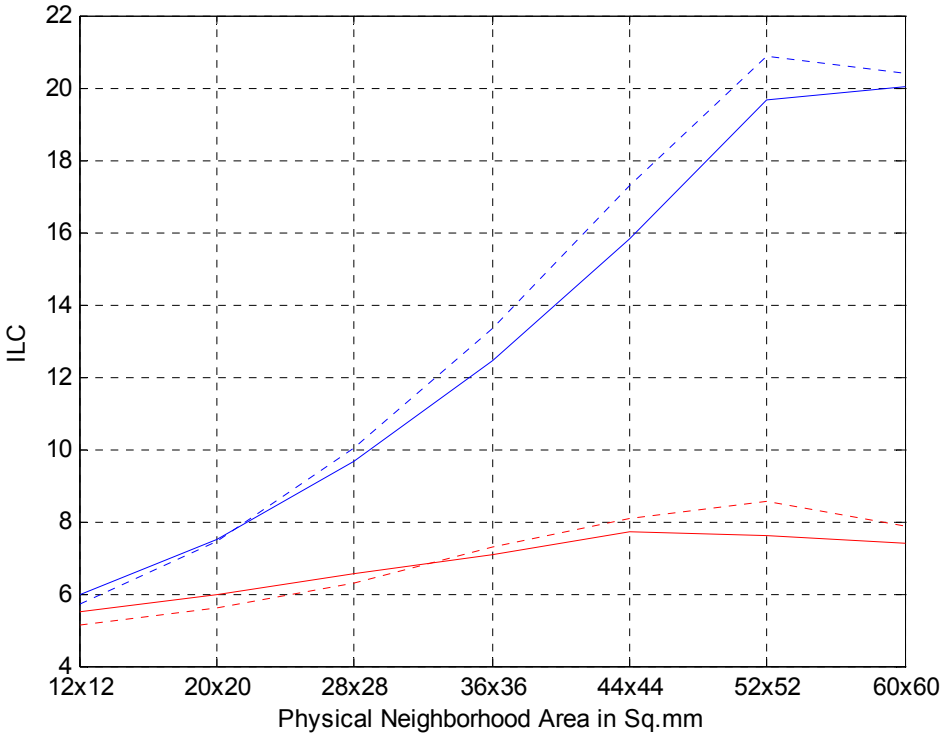

Figure 5.7 Variation of ILC with increasing neighborhood size for both high (dotted line) and low resolution data (solid line). Blue: gray matter. Red: white matter

Effect of Physiological Noise

As shown in both Table 5.2 and Fig. 5.8, the removal of respiratory and cardiac noise did not significantly alter the ILC values in gray matter and white matter. In fact, the Wilcoxon rank sum test showed that the difference in the tissue ILCs before and after correction is not significant. The difference map in Fig. 5.8 shows that most voxels were not affected by the correction, with few voxels in isolated areas in the proximity of large vessels and cerebrospinal fluid exhibiting detectable differences.

Table 5.2 Effect of physiological rhythms on ILC. BC- Before correction for physiological noise. AC- After Correction

Subject	Gray Matter			White Matter		
	BC	AC	p-value	BC	AC	p-value
4	21.7	22.7	0.35	11.4	12.0	0.34
5	27.9	28.1	0.76	11.8	11.7	0.89
6	26.3	26.7	0.59	8.1	8.3	0.66

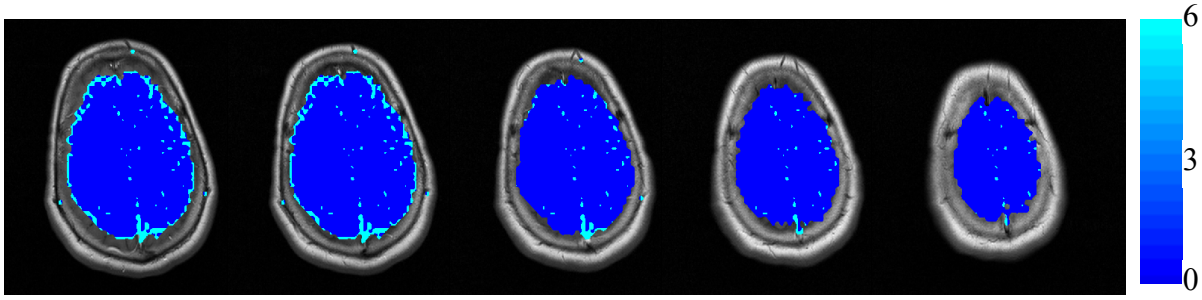

Figure 5.8 ILC difference maps obtained by subtracting the ILC maps before and after correcting for physiological noise for five slices

Tissue-specificity

ILC was found to be tissue-specific as shown in Fig. 5.9 where the gray matter-white matter boundary, obtained from manual segmentation, is overlaid on the ILC image for a representative subject. The corresponding mean ILC values for gray matter and white matter are shown in Tables 5.1 and 5.2. The p-values of the Wilcoxon ranksum test are less than 10^{-20} for all the subjects, indicating that white matter and gray matter ILC

distributions are significantly different. ILC is higher in the gray matter than that in the white matter (a fact also apparent in the gray matter and white matter distributions shown in Fig. 5.10). This difference possibly reflects a combination of neuronal and hemodynamic factors that have been implicated in earlier reports of differences between gray matter and white matter (Kruger *et al*, 2001; Deshpande *et al*, 2006).

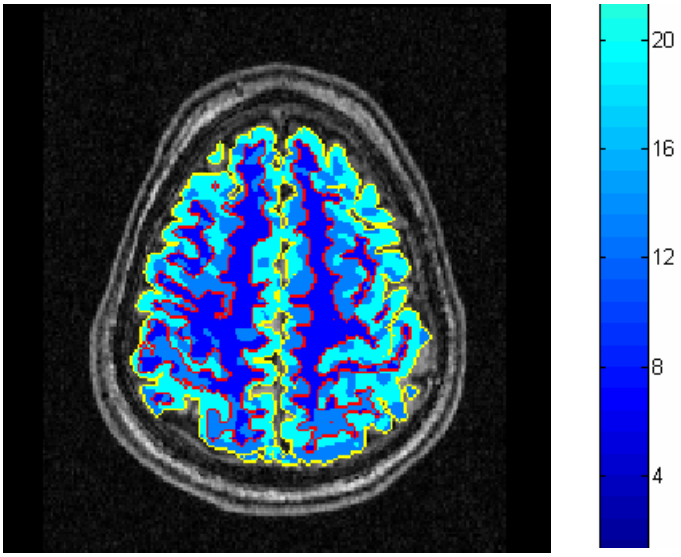

Figure 5.9 ILC map during resting-state with overlaid gray matter-white matter boundary indicating the tissue specificity of ILC

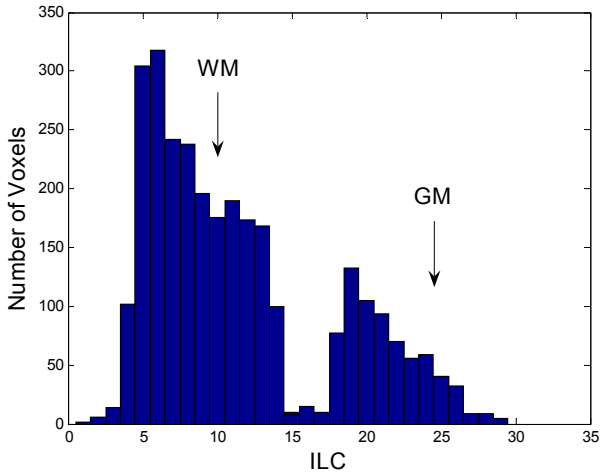

Figure 5.10 Histogram of Fig. 5.9 showing gray matter and white matter distributions of ILC

Regional ILC Differences in Gray Matter

Fig. 5.11 shows the regions having ILC values significantly higher than the mean gray matter ILC for the three subjects from the second experiment. It is evident that the components of the default mode network, particularly posterior and anterior cingulate cortices have significantly higher ILC compared to other gray matter regions. This result is consistent with previous studies which have reported significantly higher regional cerebral blood flow (Raichle *et al*, 2001) and ReHo values (He *et al*, 2004) in the default mode network.

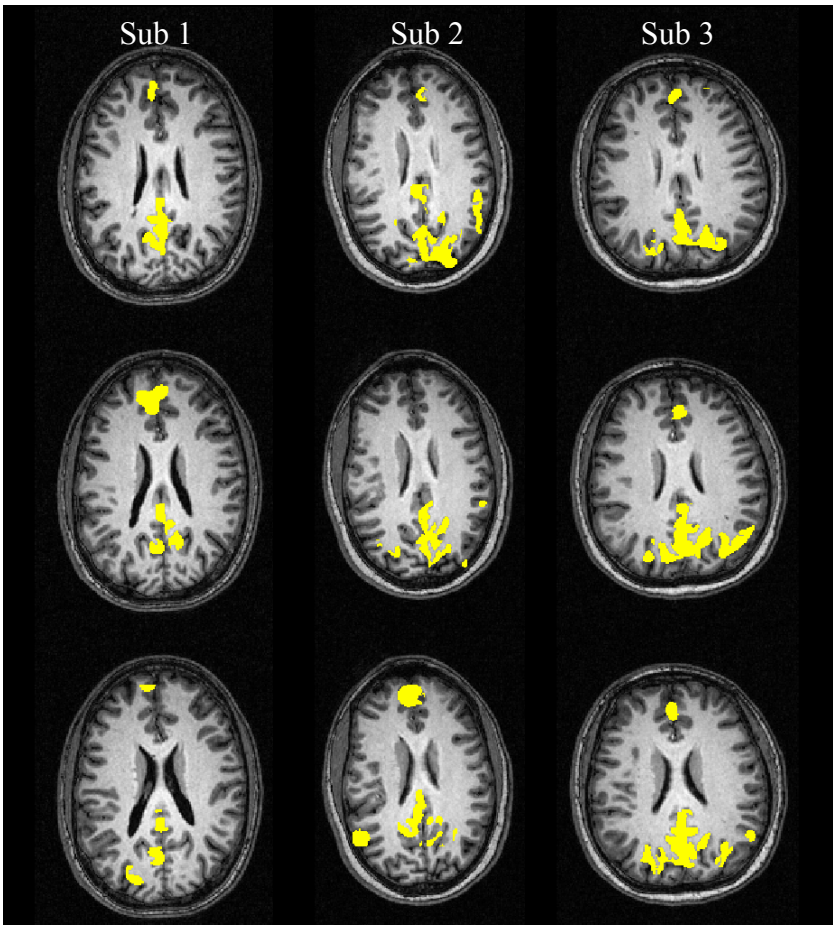

Figure 5.11 Regions having ILC values significantly higher than the mean gray matter ILC for the three subjects. The three slices shown in each subject are those containing the majority of voxels exhibiting significantly higher ILC

Reproducibility

Table 5.3 lists the correlation coefficients between the ILC maps obtained from three repeated runs in three subjects. It is clear that there is a high degree of consistency between them. The resting-state ILC maps for all the three subjects are shown in Fig. 5.12. In these maps tissue-specific patterns are consistent across consecutive resting-state runs. Note that the value and the spatial patterns of the phantom ILC (Fig. 5.5) are significantly different from those shown in Fig. 5.12, confirming that the tissue-specific resting-state pattern is not due to the inherent correlation.

Table 5.3 Correlation coefficient between ILC maps obtained from repeated runs demonstrating reproducibility

Subject	Run 1 and Run 2	Run 1 and Run 3	Run 2 and Run 3
1	0.94	0.94	0.95
2	0.93	0.91	0.94
3	0.84	0.83	0.91

Differentiating Experimental Conditions

It is evident from the ILC difference maps shown in Fig. 5.13 that there is a reduction of local coherence in the default mode network during the continuous motor task as compared to resting state. This is consistent with previous reports of deactivation of the default mode network during the performance of an explicit task as compared to resting state (Raichle *et al*, 2001). This result shows that ILC could be a useful measure to capture ROI-specific changes in local coherence with different experimental conditions. Interestingly, the continuous motor task did not alter the ILC values in the motor network

significantly similar to a lack of change in inter-regional connectivity in the network reported by a previous study (Morgan *et al*, 2004)

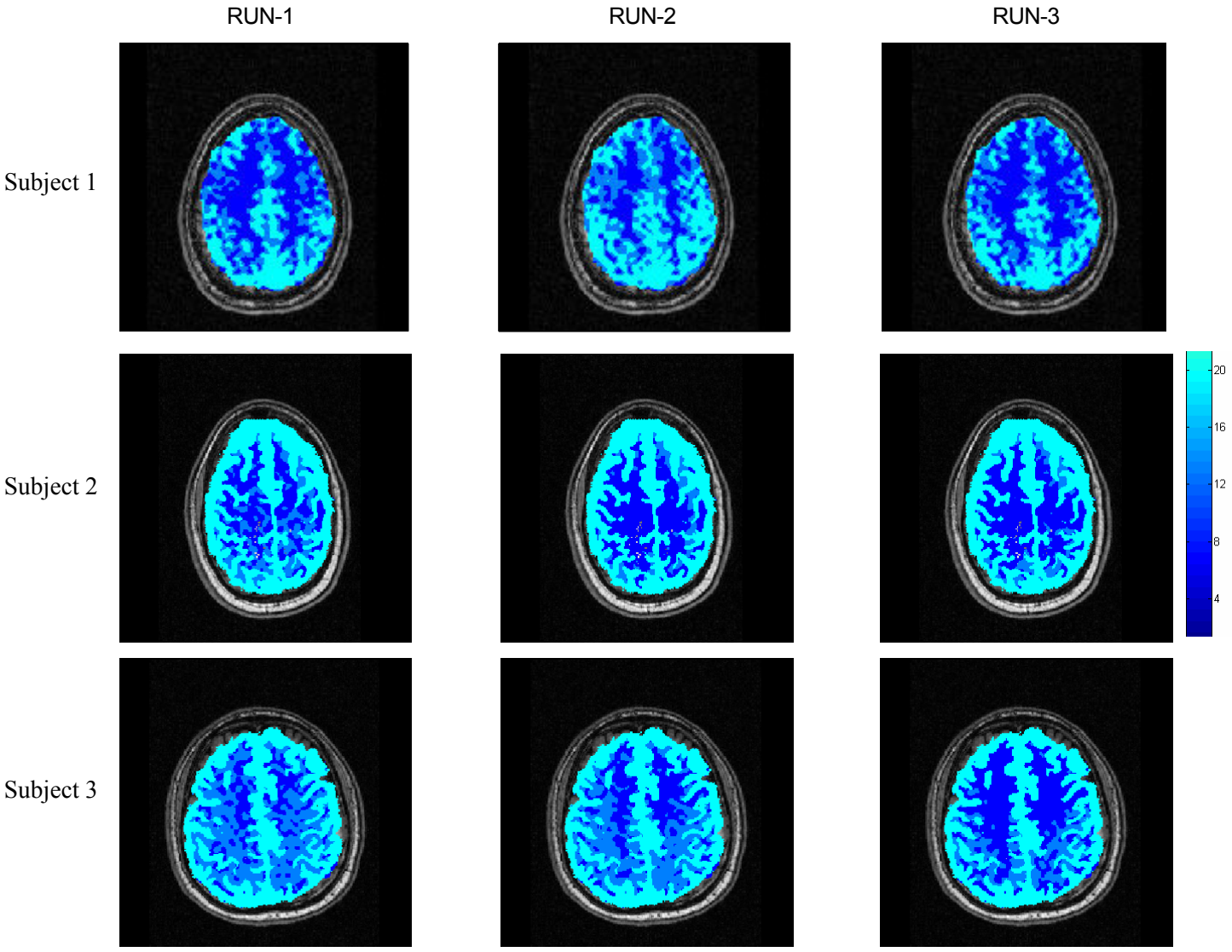

Figure 5.12 ILC maps for three consecutive resting-state runs in healthy individuals

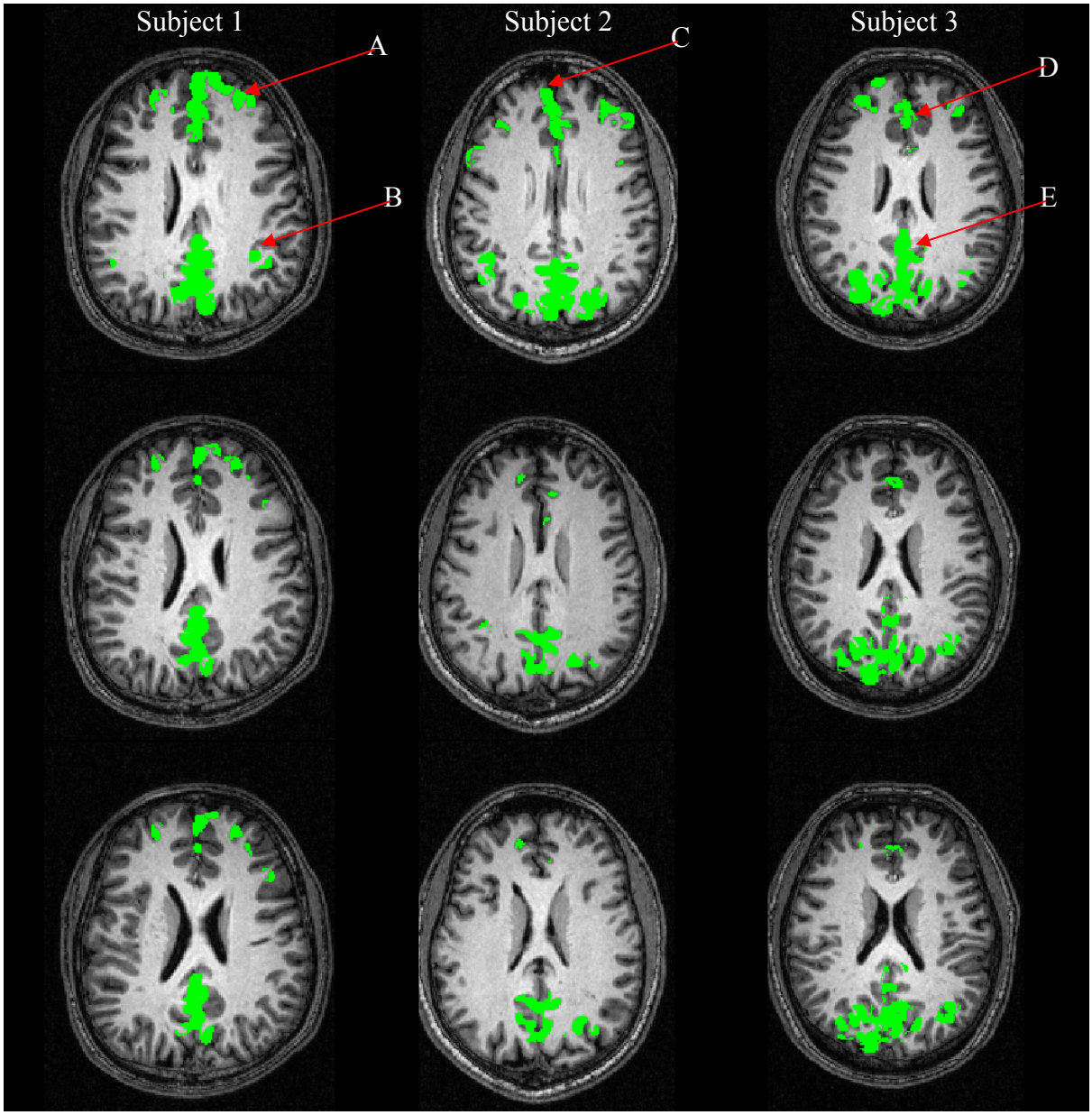

Figure 5.13 ILC difference maps showing the regions having higher ILC during resting state as compared to the continuous motor condition. Note that the maps were thresholded at a p-value of 0.05. The regions indicated are A: Lateral pre-frontal cortex (LPFC), B: Inferior parietal cortex (IPC), C: Medial pre-frontal cortex (MPFC), D: Dorsal anterior cingulate cortex (dACC) and E: Posterior cingulate cortex (PCC) extending rostrally into precuneus. The slices containing the components of the default mode network are displayed for each subject.

Comparison of ILC and ReHo

As shown in Table 5.4, the difference between gray and white matter distributions was only significant in one subject for ReHo while it was significant in all three subjects for ILC. A comparison of gray matter and white matter ReHo distributions shown in Fig. 5.14 with that of the corresponding ILC distributions in Fig. 5.10 confirms the results shown in Table 5.4. Previous studies (Deshpande *et al*, 2006; Kruger *et al*, 2001) have attributed tissue specificity in the brain to differences in fMRI physiology and neural processing. Our results show that ILC may be more sensitive to these differences as compared to ReHo.

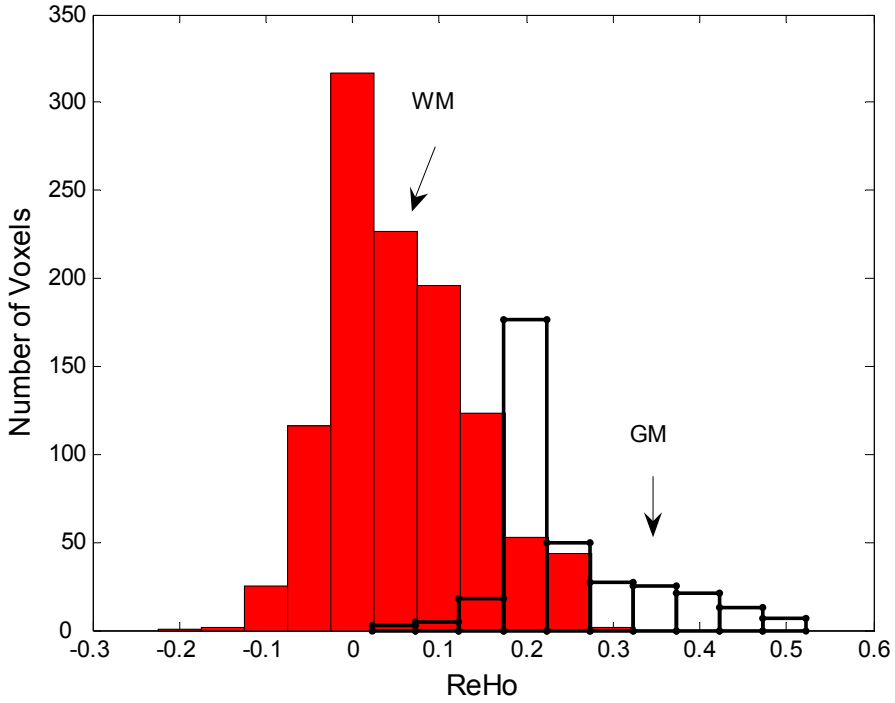

Figure 5.14 Histograms of the ReHo values of the white matter (WM) and gray matter (GM). This histogram is derived from the data of the subject shown in Fig. 5.10. Based on these histograms it is difficult to separate the gray matter from the white matter based on ReHo values

Table 5.4 Mean ILC and KCC values of gray matter and white matter

Subject	ILC			KCC		
	Gray Matter	White Matter	p-value	Gray Matter	White Matter	p-value
1	21.6	6.0	0	0.20	0.04	0.10
2	20.3	7.6	0	0.18	0.05	0.12
3	23.2	7.2	0	0.26	0.05	0.05

Application to Anesthesia Data

The ILC maps in the awake, deep and light states for a representative subject are shown in Fig. 5.15. The ROI specific ILC values for individual subjects are shown in Fig. 5.16. It can be seen that there is a significant decrease in local coherence in the deep anesthetic state in all the regions of the default mode network. The transition from deep to light state is accompanied by an increase in local coherence. The recovery in the light state is partial to complete in posterior cingulate cortex, anterior cingulate cortex and inferior parietal cortex. However in the frontal cortex, ILC does not change significantly between the deep and light states and remains attenuated in the light state.

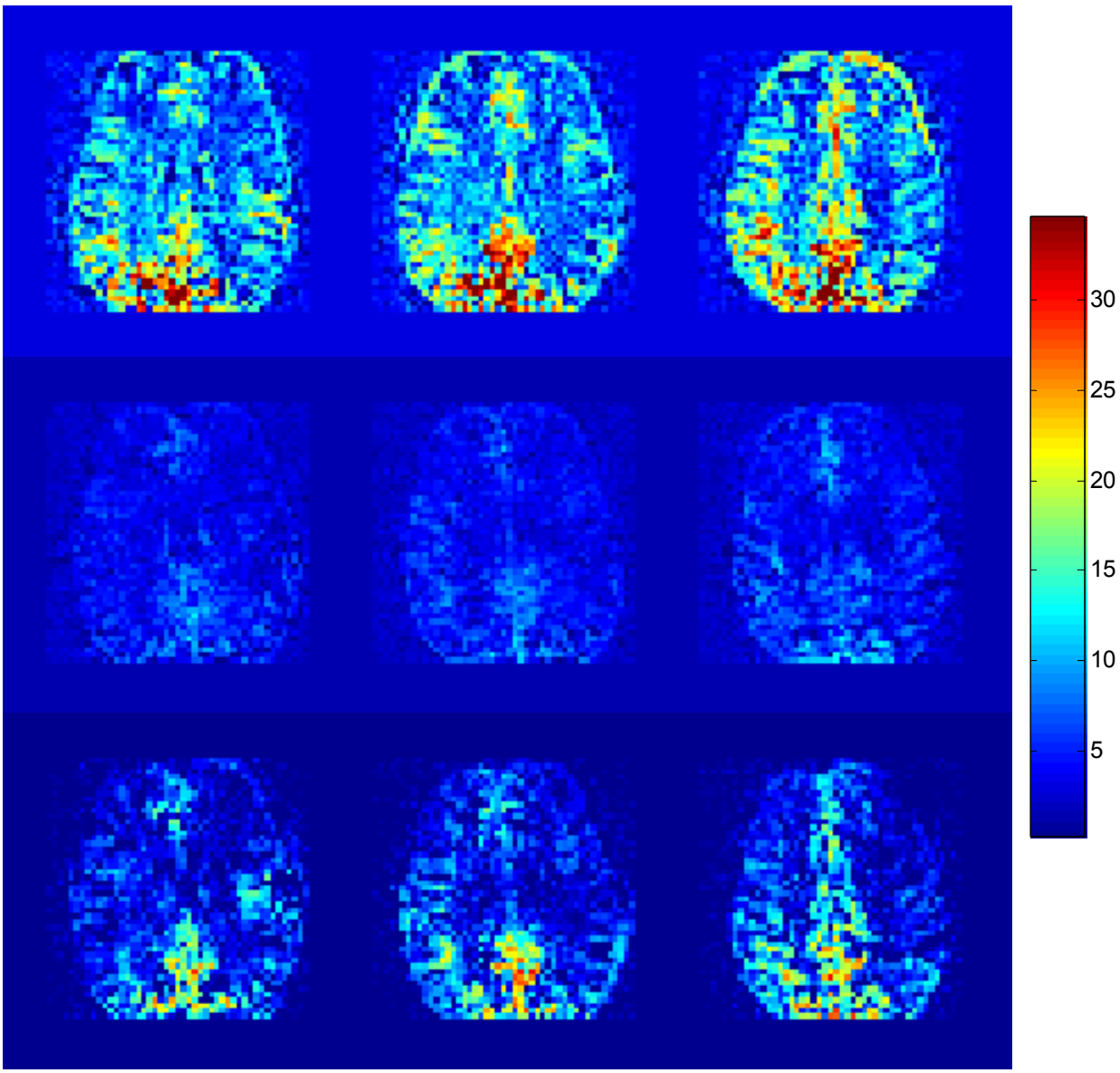

Figure 5.15 ILC maps for the awake (top), deep (middle) and light (bottom) anesthetic states in a representative subject. Slices containing the default mode network are displayed

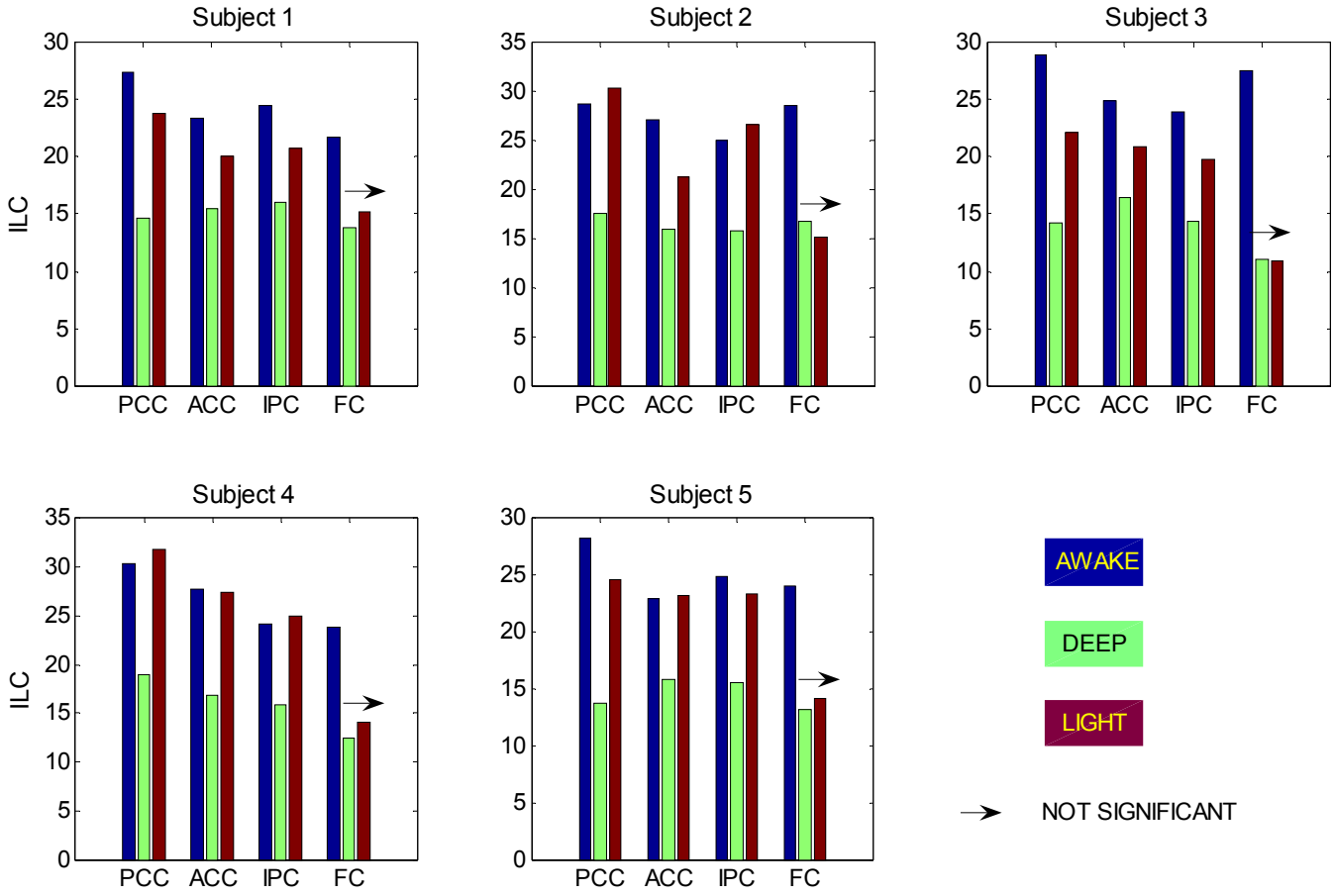

Figure 5.16 ROI-specific ILC values for all the five subjects. Arrow indicates that the corresponding transition was not significant ($p>0.05$). PCC: Posterior cingulate cortex, ACC: Anterior cingulate cortex, IPC: Inferior parietal cortex, FC: Frontal cortex. The color of the bar indicates the anesthetic state. Blue: awake, Green: deep and Red: light

The above results support existing hypotheses regarding the neurophysiological effects of artificially induced anesthesia. In addition, they provide novel insights into local connectivity changes associated with sevoflurane anesthesia. Network models have hypothesized that loss of consciousness due to anesthesia is a result of cognitive unbinding initiated by reduced connectivity of distributed networks (Tononi *et al*, 1998; Crick *et al*, 2003; Mashour, 2004). Previous studies showing reduced thalamo-cortical (Ries *et al*, 1999; White *et al*, 2003) and cortico-cortical (Peltier *et al*, 2005, 2006)

connectivity due to anesthesia, support the above hypothesis. There is preliminary evidence to suggest that distributed connectivity between the regions of the default mode network reduces with higher concentrations of sevoflurance (Peltier *et al*, 2006). Our results indicate that reduced local connectivity may accompany corresponding reduction of distributed connectivity. The fact that local coherence reduces in individual regions of the default mode network in the deep state suggests that ILC may be a useful tool to assess connectivity within individual regions.

The default mode network has been implicated in self-awareness (Raichle *et al*, 2001; Greicius *et al*, 2003). Also, the default mode network has been shown to be having a role during altered states of consciousness such as sleep (Horovitz *et al*, 2006) and meditation (Pagnoni *et al*, 2006). Therefore we hypothesized that the default mode network may be involved in sedation induced by anesthesia. Our results support this hypothesis and suggest that in addition to the dynamic core network proposed by Tononi *et al* (1998), the default mode network may also have a role in loss and recovery of consciousness.

While the attenuation of local coherence in the deep state was uniform, the recovery of ILC in the light state was ROI specific. The fact that the revival was partial to complete in posterior cingulate cortex, anterior cingulate cortex and inferior parietal cortex while it was not significant in the frontal cortex supports the notion that anesthesia is not a uniform entity (Veselis *et al*, 2001) and there may be different end points of interest such as ablation of sensorimotor responses and executive functions. Our results suggest that cortical functionality may be compromised in the frontal areas in the light state while it was not the case with other regions. This supports earlier reports of dose

dependent suppression of cortical function (Antognini *et al*, 1997; Veselis *et al*, 2002) and reduction of regional cerebral blood flow (rCBF) due to anesthesia (Bonhomme *et al*, 2001) and behavioral deficits in psychomotor and cognitive performance (Galinkin *et al*, 1997, Ibrahim *et al*, 2001).

It is to be noted that the results should be viewed within the context of our experiment and not be generalized. Sedatives such as midazolam have been shown to increase the temporal synchrony in fMRI BOLD signal (Kiviniemi *et al*, 2005), an effect contrary to that reported in studies employing sevoflurane as a sedative (Peltier *et al*, 2005). The effect of different sedatives and their mechanism of administration on brain physiology are not properly understood. Also, in the absence of a unified model, the mechanisms involved in anesthesia-induced consciousness alterations have not been established. Moreover, consciousness may not be a monolith and hence its neural substrates could vary depending on whether it is induced artificially (sedatives) or naturally (sleep) (Mashour, 2004). In the light of these facts, our results should be interpreted within the specifics of our experiment.

Spatial Largest Lyapunov Exponent

Simulated Coupled Map Lattice

Fig. 5.17 shows the Lyapunov spectra for a coupled logistic lattice of size I=20 with periodic boundary conditions obtained using the known dynamics (Eq. 5.3). From this figure we can observe that some Lyapunov exponents are positive proving that the system has determinism. Also, a low positive value for the largest exponent indicates the existence of spatial coupling, which in fact is the case. Therefore the simulations indicate

that the CML model shown in Fig. 5.2 could be used to capture the spatiotemporal dynamics of a coupled system and characterize the spatial couplings in such a framework. Thus, the application of this model for real fMRI data is justified.

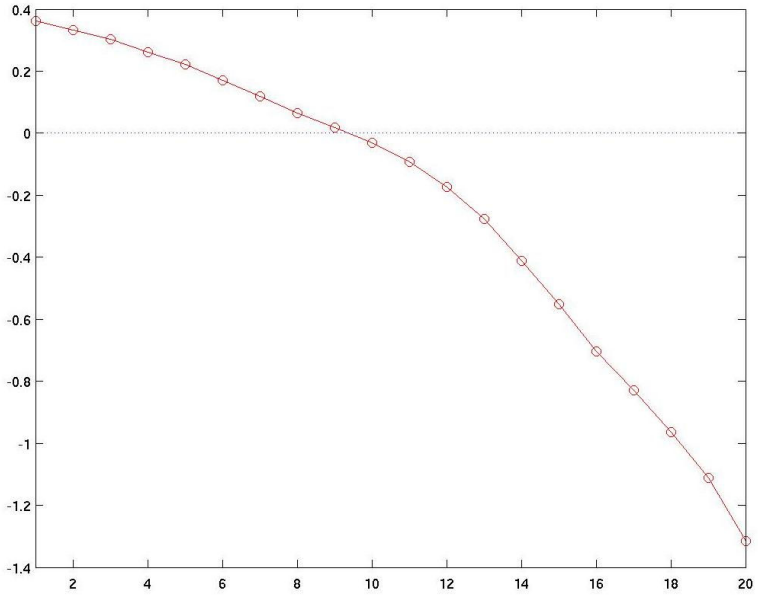

Figure 5.17 Lyapunov spectrum for a CML of N=20 fully chaotic logistic maps f(x)=4x(1-x) with coupling strength ε =0.4

Application to Resting State fMRI Data

Table 5.5 lists the mean SLLE values calculated using a 60×60 mm^2 neighborhood. The neighborhood choice was dictated by the results presented in the previous section which showed that correlation becomes negligible after a 60×60 mm^2 neighborhood. This is also supported by previous studies which investigated spatial correlation (Bellec *et al*, 2006) in the brain. The relatively low positive values of SLLE point to the existence of local coupling as demonstrated by ILC. Also, gray matter exhibits higher local coupling than white matter. Note that a lower value of SLLE indicates lesser divergence and hence higher coupling. These results confirm the results

obtained by ILC and suggest that SLLE could perhaps be used as a complimentary approach while investigating local coherence in the brain. However, SLLE is similar to the ReHo approach in the sense that it utilizes distinct time series in the neighborhood instead of a spatial function as in ILC. Therefore it suffers from the same disadvantages as that of ReHo described before.

Table 5.5 Mean values of SLLE. The difference between gray and white matter SLLE was significant in all subjects ($p<0.05$)

SLLE	Gray matter	White matter
Subject 1	1.30	1.96
Subject-2	0.93	1.68
Subject-3	1.69	1.99

Conclusions

In this work we have introduced and characterized a general measure, ILC, to quantify local brain coherence. We hypothesized and demonstrated that ILC is effectively independent of image resolution and the neighborhood size as long as it is sufficiently large. In addition, we also found that respiratory and cardiac fluctuations do not significantly affect ILC values in brain tissue. Furthermore, the inherent correlation in the data was found to be small but non-negligible, and a correction was introduced. As a demonstration of biological relevance, reproducible, tissue-specific ILC patterns were found in the resting-state fMRI data of healthy individuals and discriminated between gray and white matter. Within the gray matter, the default mode network exhibited higher ILC in resting state. The reduction of ILC in the default mode network during a

continuous motor task as compared to the resting state showed the utility of ILC in discriminating experimental conditions. Also ILC was shown to discriminate between different tissues better than regional homogeneity (ReHo). It is concluded that the ILC measure is a robust tool to assess local brain coherence. Subsequently, we demonstrated the neuroscientific utility of ILC with application to anesthesia. We investigated the changes in local coherence of the default mode network with graded sedation induced by sevoflurane anesthesia. The results indicated that in the deep anesthetic state, local coherence reduced in all the regions of the default mode network. However, the recovery in the light anesthetic state was partial to complete in posterior cingulate cortex, anterior cingulate cortex and inferior parietal cortex while it was not significant in the prefrontal cortex. These results imply that the default mode network, particularly the frontal cortex, has a significant role in the neurophysiological changes induced by anesthesia. Finally, the linear ILC approach was complemented by the nonlinear SLLE approach and we showed that the concept of embedding which we introduced in the earlier chapters could also be used to study connectivity in local networks.

CHAPTER 6

CONCLUSIONS

The Problem Revisited

We briefly discuss the problem we set out to investigate, the path taken and the result of the investigation. The principal motive behind this work was to explore the applicability of nonlinear dynamics and network analysis for characterizing brain function. This motive was driven by the fact that though brain is known to act as a nonlinear system, there has hardly been any effort to explore the applicability of nonlinear analysis techniques to fMRI data. Also, recent trends have suggested that functional localization as a model of brain function is incomplete and that certain sensory, motor and cognitive functions may be carried out by a network of regions rather than individual areas. Given this fact, it is imperative to develop network models in an effort to understand brain function. Therefore this thesis attempts to introduce the twin concepts of nonlinear dynamics and network analysis into a broad spectrum of fMRI data analysis techniques.

Overview of Findings

This work has provided a new thrust towards incorporating the concepts of nonlinear dynamics and network analysis in the repertoire of fMRI data analysis techniques which covers both univariate and multivariate methods.

The second chapter explored the importance of low dimensional determinism in resting state fMRI fluctuations using principles drawn from the concept of embedding and information theory. We showed that fMRI time courses are not produced by a purely stochastic system, and hence used various nonlinear techniques to obtain a new perspective into the underlying system dynamics. The results from the above techniques showed that brain dynamics can be neither characterized by a purely stochastic nor a fully deterministic system. On the contrary, the underlying dynamics seems to be deterministic, produced by a system having roughly ten state variables, exhibiting non-uniform determinism among the different regions of the brain, with gray matter showing more determinism than white matter and CSF. What was previously perceived as higher random fluctuation in the gray matter was actually due to the deterministic nonlinearity of the signal produced by an underlying nonlinear dynamical system. We found that nonlinearity exhibits tissue specificity even after the removal of physiological fluctuations. The possibility of higher noise level in gray matter as the main reason for tissue-specificity of deterministic nonlinearity was examined and ruled out. Therefore, higher nonlinear determinism in gray matter is not due to cardiac/respiratory effects or noise intensity differences, but can potentially be attributed to local differences in fMRI physiology and neural processing.

The third chapter extended the concept of embedding to multivariate analysis allowing us to characterize nonlinear functional connectivity in distributed brain networks during resting state and bimanual continuous movement. A new measure, bivariate nonlinear connectivity index, was introduced and shown to have higher sensitivity to the gray matter signal as compared to linear correlation and hence more

robust to artifacts. Also, sliding window analysis was carried out to investigate the dynamical connectivity changes in the distributed motor network during the bimanual continuous motor task.

The fourth chapter dealt with the extension of functional connectivity to include directional interactions in the brain, which is termed effective connectivity. We investigated both linear and nonlinear Granger models of effective connectivity. First, we demonstrated the utility of an integrated approach involving multivariate linear Ganger causality, coarse temporal scale analysis and graph theoretic concepts to investigate the temporal dynamics of causal brain networks. Multivariate granger causality allowed us to factor in the effects of all relevant ROIs simultaneously. The coarse temporal scale analysis obviated the effect of the spatial variability of the hemodynamic response on prediction and permitted us to study slowly varying neural changes caused by fatigue. Subsequently, by applying graph theoretic concepts, we obtained an interpretable characterization of the complicated network topology. We believe that our integrated approach is a novel contribution to the effective connectivity analysis of functional networks in the brain. Application of this approach to motor fatigue data revealed the dynamic evolution of the motor network during the fatigue process and reinforced the hypothesis of fatigue induced reduction in network connectivity. Finally we showed that the results obtained from nonlinear Granger models were akin to the linear results. However, the nonlinear model was more robust to artifacts such as baseline drifts as compared to the linear model.

The fifth chapter investigated connectivity in local networks. In this work we introduced and characterized a robust linear measure, ILC, to quantify local brain

coherence. This measure is an improvement upon existing linear measures such as ReHo, to measure local coherence in the brain. We hypothesized and demonstrated that ILC is effectively independent of image resolution and the neighborhood size as long as it is sufficiently large. In addition, we also found that respiratory and cardiac fluctuations do not significantly affect ILC values in brain tissue. Furthermore, the inherent correlation in the data was found to be small but non-negligible, and a correction was introduced. As a demonstration of biological relevance, reproducible, tissue-specific ILC patterns were found in the resting-state fMRI data of healthy individuals which discriminated between gray and white matter. Within the gray matter, the default mode network exhibited higher ILC in resting state. The reduction of ILC in the default mode network during a continuous motor task as compared to the resting state showed the utility of ILC in discriminating experimental conditions. Also ILC was shown to discriminate between different tissues better than regional homogeneity (ReHo). Thus it was found that the ILC measure is a robust tool to assess local brain coherence. Subsequently, we demonstrated the neuroscientific utility of ILC with application to anesthesia. We investigated the changes in local coherence of the default mode network with graded sedation induced by sevoflurane anesthesia. The results indicated that in the deep anesthetic state, local coherence reduced in all the regions of the default mode network. However, the recovery in the light anesthetic state was partial to complete in posterior cingulate cortex, anterior cingulate cortex and inferior parietal cortex while it was not significant in the prefrontal cortex. These results imply that the default mode network, particularly the frontal cortex, has a significant role in the neurophysiological changes induced by anesthesia. Finally, the linear ILC approach was complemented by the nonlinear SLLE approach and we

showed that the concept of embedding which we introduced in earlier chapters could also be used to study connectivity in local networks.

Final Thoughts

We conclude this thesis by stating that the concepts of nonlinear dynamics and network analysis have the potential to add great value to the existing fMRI data analysis techniques in aiding us to construct models of brain function at a systemic level. Nonlinear models give some additional insights and were found to be generally more robust to artifacts and more sensitive to signals of biological interest than linear models. But the trade off is that nonlinear models are computationally more intensive and hence if computational complexity is not a concern and we are not able to account for the artifacts separately, then nonlinear linear models may be better.

Network models of brain function give invaluable insights into the working of the brain. While functional localization studies have their own value, we believe that it is incomplete. Our findings confirm the recent reports in the field that evaluating interactions between regions in the brain and studying their dynamics forms an inseparable part of the effort to understand the systems level functional organization of the human brain.

APPENDIX A

ESTIMATION OF MINIMUM EMBEDDING DIMENSION

The technique we have employed to estimate the minimum embedding dimension (MED) of fMRI data is a variant of False Nearest Neighbor (FNN) method and follows the description by Cao (Cao, 1997). The first step in nonlinear dynamical analysis is the reconstruction of the attractor in phase-space using Taken's embedding theorem (Takens, 1980), which ensures that the reconstructed attractor preserves all topological properties of the original attractor.

Given an fMRI time series from a single voxel, $x(i), i = 1,2,.....L$, its time-delay vectors in phase-space are formed as:

$$\boldsymbol{X} = [\boldsymbol{X}_1 \quad \boldsymbol{X}_2 \ldots\ldots\ldots \boldsymbol{X}_N]^{\mathrm{T}} \tag{A.1}$$

where the number of time-delay vectors is given by $N = L - (m-1)\tau$, τ being the time delay and m being the embedding dimension, and each time-delay vector is given by

$$\boldsymbol{X}_i = [x(i+\tau)\ x(i+2\tau)\ \ldots\ldots\ x(i+(m-1)\ \tau]\ ;\ I = 1,2,\ldots\ldots\ L-(m-1)\ \tau \tag{A.2}$$

τ is selected using the autocorrelation function based technique (Tsonis, 1992).

For each phase-space vector, $\boldsymbol{X}_i$, its distance to its nearest neighbor at different values of *m*, *d(i, m),* is computed. The ratio, *d(i, m+1)/d(i ,m),* is calculated and averaged over *i* to derive $E(m)$. $E(m)$ is dependent only on m and τ. In order to see its variation from m to $m+1$, we examine $E_1(m)$, defined the ratio of *E(m+1) to E(m)*. It is found that the $E_1(m)$ approaches a saturation value of 1 when *m* is greater than some value m_o if the time series comes from an attractor.

To determine m_o at which E_1 attains saturation, a nonlinear least-squares fit to E_1 is obtained (Por et al, 2005). The fit is assumed to be of an exponential form given by the equation $b - e^{-m-c}$ where the initial values of b and c are 1 and 0 respectively. The values of b and c corresponding to the closest fit are obtained using the Gauss-Newton method (Por et al, 2005). The residual, which is the error between the fit and the original curve, is the highest at the knee of the curve. Since the saturation point is represented by the knee of the curve, the dimension corresponding to the maximum residual is taken as the MED.

APPENDIX B

PATTERN OF SINGULARITIES IN THE COMPLEX PLANE (PSC) ALGORITHM

The steps for deriving PSC of a given fMRI time series are:

1. Determine the local maxima s_{t_j} and the time at which it occurred, t_j in the fMRI time series, where j is the index for each maximum and assumed to have values *1,2,…….. m*.
2. Define L_o as a global distance measure in the s_t-t space:

$$L_0 = \sqrt{\sum_{j=1}^{m-1} \{(s_{t_{j+1}} - s_{t_j})^2 + (t_{j+1} - t_j)^2\}} \tag{B.1}$$

3. Generate *n* number of surrogates and compute L_o for each surrogate. Gaussian scaled surrogates were generated by rank ordering the fMRI time series in the rank order of the time series obtained from a phase-randomized Gaussian distribution of the same mean and standard deviation as that of the fMRI data (Di Garbo et al, 1998).
4. Determine mean M_L and standard deviation σ_L of these quantities.
5. Determine the measure of significance.

$$S_{psc} = \frac{|L_o - M_L|}{\sigma_L} \tag{B.2}$$

The hypothesis (that the given time series is not different from a linear process) is rejected if this significance is greater than a threshold (for this work, we have chosen the

95% confidence level). Moreover, the significance value is the PSC measure, which can be used as a quantifier to assess the deviation of the fMRI time series from linearity. The larger its value, the more nonlinear is the fMRI time series.

APPENDIX C

LEMPEL-ZIV COMPLEXITY MEASURE ALGORITHM

Lempel-Ziv (LZ) is a complexity measure for assessing the structure of a signal (Zhang et al, 1999) from an information theoretic point of view. The algorithm for calculating this complexity measure *c(n)* for a given fMRI time series *x(i)* of length *n* can be summarized as follows. *x(i)* must be first transformed into a finite symbol sequence *L* with two possible binary values: zero and one. We start by subtracting the mean value of *x(i)* from every data point. We need to find a threshold *T* to transform *x(i)* into a binary sequence. The threshold is found as follows. Positive peak value U_p and negative peak value U_n of *x(i)* are calculated. The number of data points of *x(i)* which satisfy the condition $0<x_i<10\%U_p$.is calculated. Let this number be *A*. Similarly, the number of data points of *x(i)* satisfying the condition $10\%U_n<x_i<0$ is calculated. Let this number be *B*. If (*A*+ *B*) < 40% of *n*, threshold *T=0.* If *(A<B), T = 20% U_p else, T = 20% U_n* . The value of each data point of the fMRI time series *x(i)* is compared with *T* and assigned a value of 0 or 1 depending on whether it's value is below or above *T*. The finite binary sequence *L* is used for further analysis.

Let us consider the sequence $L = s_1,s_2,\ldots,s_n$, where s_i is the character 0 or 1. Let *M* and *N* be two sub-strings of *L* and let *MN* be their concatenation. We will denote *MN′* as the sequence *MN* without its last character. Initially, *c(n)* is set to 1. Therefore *c(n)=1,* $M=s_1$, $N=s_2$, $MN= s_1s_2$ and $MN' =s_1$. If $M = s_1,s_2,\ldots,s_r$ *(1<r<n)* and N= s_{r+1} , then $MN'= s_1,s_2,\ldots,s_r$. The value of c(n) is incremented by one if $N\notin MN'$. $N\in MN'$, then N is a sub-sequence of *MN′* and not a new sequence. Therefore *M* remains unchanged and *N* is

renewed to s_{r+1}, s_{r+2}. The process of appending and comparing N to MN' is continued until $N \not\in MN'$ again. As the whole sequence L is traversed, the value of $c(n)$ is also updated. The final value of $c(n)$ obtained by traversing the whole length of L, is the complexity measure. Normalization of the final c(n) results in the LZ measure. Let $d(n)$ be the value of $c(n)$ in the asymptotic case of an infinitely long random string. Then,

$$d(n) = \lim_{n \to \infty} c(n) = \frac{n}{\log_2 n} \tag{C.1}$$

Finally, the normalized complexity measure, LZ, is given by

$$c(n) \Big/ d(n) \tag{C.2}$$

APPENDIX D

PUBLICATIONS ARISING FROM THIS THESIS

Journal Articles

1. Gopikrishna Deshpande, Stephen LaConte, Scott Peltier, Xiaoping Hu. 2006. Tissue specificity of nonlinear dynamics in baseline fMRI. *Magnetic Resonance in Medicine* 55(3): 626-632.

2. Gopikrishna Deshpande, Stephen LaConte, Scott Peltier, Xiaoping Hu. 2006. Connectivity analysis of human functional MRI data: from linear to nonlinear and static to dynamic. *Lecture Notes in Computer Science* 4091: 17-24.

3. Gopikrishna Deshpande, Stephen LaConte, Scott Peltier, Xiaoping Hu. Integrated Local Correlation: a New Measure of Local Coherence in fMRI Data. *Human Brain Mapping*, *under review*.

4. Gopikrishna Deshpande, Stephen LaConte, George Andrew James, Scott Peltier, Xiaoping Hu. Multivariate Granger Causality Analysis of Brain Networks. *Human Brain Mapping*, *under review*.

Conference Proceedings

1. Gopikrishna Deshpande, Stephen LaConte, Scott Peltier, Xiaoping Hu. 2005. Spatial embedding of fMRI for investigating local coupling in human brain. *Proceedings of SPIE International Symposium on Medical Imaging, San Diego* 5746: 119-125.

2. Gopikrishna Deshpande, Stephen LaConte, Scott Peltier, Xiaoping Hu. 2005. Evaluation of nonlinear functional connectivity using phase-space embedding. *Proceedings of ISMRM 13th Scientific Meeting, Miami* 13: 1598.

3. Gopikrishna Deshpande, Stephen LaConte, Scott Peltier, Xiaoping Hu. 2006. Tissue specificity of nonlinear dynamics in baseline fMRI. *Proceedings of ISMRM 14th Scientific Meeting, Seattle* 14: 533.

4. Gopikrishna Deshpande, Stephen LaConte, Scott Peltier, Chantal Kerssens, Stephen Hamman, Peter Sebel, Michael Byas-Smith, Xiaoping Hu. 2006. Local Coherence as a Measure of Localized Co-ordination in the Brain: An Application to Anesthesia. *Proceedings of ISMRM 14th Scientific Meeting, Seattle* 14: 1100.

5. Gopikrishna Deshpande, Stephen LaConte, Scott Peltier, Xiaoping Hu. 2006. Investigating effective connectivity in cerebro-cerebellar networks during motor learning using directed transfer function. 12th annual meeting of Human Brain Mapping, Florence, Italy. Reference in *NeuroImage* 31 (S40): 377.

6. Gopikrishna Deshpande, Stephen LaConte, Scott Peltier, Xiaoping Hu. 2006. Directed transfer function of fMRI to investigate network dynamics. *Proceedings of 28th Annual International Conference of IEEE EMBS New York*: 671-674.

7. Gopikrishna Deshpande, Stephen LaConte, Scott Peltier, Xiaoping Hu. 2007. Integrated Local Correlation: a New Measure of Local Coherence in fMRI Data. *Proceedings of ISMRM 15th Scientific Meeting, Berlin, Germany* 15: 3480.

8. Gopikrishna Deshpande, Stephen LaConte, Scott Peltier, Andrew James, Xiaoping Hu. 2007. Multivariate Granger Causality Analysis of Brain Networks. *Proceedings of ISMRM 15th Scientific Meeting, Berlin, Germany* 15: 3184.

REFERENCES

Abraham FD. 1993. Chaos in brain function. *World Futures* 37: 41-58.

Abler B, Roebroeck A, Goebel R, Hose A, Schfnfeldt-Lecuona C, Hole G, Walter H. 2006 Investigating directed influences between activated brain areas in a motor-response task using fMRI. *Magnetic Resonance Imaging* 24: 181–185.

Aguirre GK, Zarahn E, D'Esposito M. 1998. The variability of human BOLD hemodynamic responses. *NeuroImage* 8: 360–369.

Akaike H. 1974. A new look at the statistical model identification. *IEEE Trans. Autom. Control* 19: 716.

Ancona N, Marinazzo D, Stramaglia S. 2004. Radial basis function approach to nonlinear granger causality of time series. *Physical Review E* 70: 562211-562217.

Antognini JF, Buonocore MH, Disbrow EA, Carstens E. 1997. Isoflurane anesthesia blunts cerebral responses to noxious and innocuous stimuli: an fMRI study. *Life Science* 61: PL 349–354.

Auer LM, Sayama I. 1983. Intracranial pressure oscillations (B-waves) caused by oscillations in cerebrovascular volume. *Acta Neurochir* 68(1-2): 93-100.

Babloyantz A, Destexhe A. 1986. Low dimensional chaos in an instance of epilepsy. *Proceedings of National Academy of Sciences USA* 83: 3513-7.

Babloyantz A. 1989. Estimation of correlation dimension from single and multichannel recording—A critical view. In Basar E & Bullock TH (Eds.), *Brain dynamics* 1:122-130, Springer-Verlag: Berlin.

Bandettini PA, Wong EC, Hinks RS, Tifosky RS, Hyde JS. 1992. Time course EPI of human brain function during task activation. *Magnetic Resonance in Medicine* 25: 390-398.

Bandettini PA, Jesmanowicz A, Wong EC, Hyde JS. 1993. Processing strategies for time-course data sets in functional MRI of the human brain. *Magnetic Resonance in Medicine* 30(2): 161-173.

Baumgartner R, Somorjai R, Summers R, Richter W. 1999. Assessment of cluster homogeneity in fMRI data using Kendall's coefficient of concordance. *Magnetic Resonance Imaging* 17: 1525–1532.

Bellec P, Perlbarg V, Jbabdi S, Pelegrini-Issac M, Anton J, Doyon J, Benali H. 2006. Identification of large-scale networks in the brain using fMRI. *NeuroImage* 29: 1231 – 1243.

Birn RM, Saad ZS, Bandettini PA. 2001. Spatial heterogeneity of the nonlinear dynamics in the FMRI BOLD response. *NeuroImage* 14(4):817-26.

Biswal B, Yetkin FZ, Haughton VM, Hyde JS. 1995. Functional connectivity in the motor cortex of resting human brain using echo-planar MRI. *Magnetic Resonance in Medicine* 34(4): 537-541.

Biswal B, DeYoe EA, Hyde JS. 1996. Reduction of physiological fluctuations in fMRI using digital filters. *Magnetic Resonance in Medicine* 35(1): 107-113.

Biswal B, VanKylen J, Hyde JS. 1997. Simultaneous assessment of flow and BOLD signals in resting-state functional connectivity maps. *NMR in Biomedicine* 10(4-5): 165-170.

Biswal B, Ulmer JL, Krippendorf RL, Harsch HH, Daniels DL, Hyde JS, Haughton VM. 1998. Abnormal cerebral activation associated with a motor task in Tourette syndrome. *American Journal of Neuroradiology* 19(8): 1509-1512.

Blinowska KJ, Kus R, Kaminski M. 2004. Granger causality and information flow in multivariate processes. *Physical Review E* 70: 50902-50906.

Bokde ALW, Tagamets MA, Friedman RB, Horwitz B. 2001. Functional interactions of the inferior frontal cortex during the processing of words and word-like stimuli. *Neuron* 30(2): 609-617.

Bonhomme V, Fiset P, Meuret P, Backman S, Plourde G, Paus T, Bushnell MC, Evans AC. 2001. Propofol anesthesia and cerebral blood flow changes elicited by vibrotactile stimulation: a positron emission tomography study. *Journal of Neurophysiology* 85:1299–1308.

Broomhead DS, King GP. 1986. Extracting qualitative dynamics from experimental data. *Physica D* 20: 217-236.

Buchel C, Friston KJ. 1997. Modulation of connectivity in visual pathways by attention: cortical interactions evaluated with structural equation modeling and fMRI. *Cerebral Cortex* 7: 768-778.

Bunimovich LA. 1997. Coupled map lattices: Some topological and ergodic properties. *Physica D* 103:1-17.

Butera RJ. 1998. Multirhythmic bursting. *Chaos* 8:274-284.

Cannon RL, Dave JV, Bezdek JC. 1986. Efficient implementation of the fuzzy c-means clustering algorithms. *IEEE Transactions on Pattern Analysis and Machine Intelligence* 8(2): 248-255.

Cao L. 1997. Practical method for determining the minimum embedding dimension of a scalar time series. *Physica D* 110: 43-50.

Cao L, Mees A, Judd K. 1998. Dynamics from multivariate time series. *Physica D* 121: 75-88.

Chen Y, Rangarajan G, Feng J, Ding M. 2004. Analyzing multiple nonlinear time series with extended Granger causality. *Physics Letters A* 324: 26-35.

Cordes D, Haughton VM, Arfanakis K, Wendt GJ, Turski PA, Moritz CH, Quigley MA, Meyerand ME. 2000. Mapping functionally related regions of brain with functional connectivity MR imaging. *American Journal of Neuroradiology* 21(9): 1636-1644.

Cordes D, Haughton VM, Carew JD, Arfanakis K, Maravilla K. 2002. Hierarchical clustering to measure connectivity in fMRI resting-state data. *Magnetic Resonance Imaging* 20(4): 305-317.

Cormen TH, Leiserson CE, Rivest RL. 2001. Introduction to Algorithms, second edition. MIT Press and McGraw-Hill.

Crick F, Koch C. 2003. A framework for consciousness. *Nature Neuroscience* 6:119–126.

Deiber MP, Passingham RE, Colebatch JG, Friston KJ, Nixon PD, Frackowiak RSJ. 1991. Cortical areas and the selection of movement: a study with positron emission tomography. *Experimental Brain Research* 84: 393-402.

Deshpande G, LaConte S, Peltier S, Hu X. 2006. Tissue specificity of nonlinear dynamics in baseline fMRI. *Magnetic Resonance in Medicine* 55(3):626-32.

Deshpande G, LaConte S, Peltier S, Hu X. 2006a. Investigating effective connectivity in cerebro-cerebellar networks during motor learning using directed transfer function. 12th annual meeting of Human Brain Mapping. Reference in *NeuroImage* 31 (S40): 377.

Deshpande G, LaConte S, Peltier S, Hu X. 2006b. Directed transfer function analysis of fMRI data to investigate network dynamics. *Proceedings of 28th Annual International Conference of IEEE EMBS*: 671-674.

Dhamala M, Pagnoni G, Wiesenfeld K, Berns GS. 2002. Measurements of brain activity complexity for varying mental loads. *Physical Review E* 65: 419171-7.

Di Garbo A, Balocchi R, Chillemi S. 1998. Nonlinearity tests using the extrema of a time series. *International Journal of Bifurcation and Chaos* 8: 1831-1838.

Ding M, Bressler SL, Yang W, Liang H. 2000. Short-window spectral analysis of cortical event-related potentials by adaptive multivariate autoregressive modeling: Data preprocessing, model validation, and variability assessment. *Biological Cybernetics* 83: 35–45.

Eddy WF, Fitzgerald M, Noll DC. 1996. Improved image registration by using Fourier interpolation. *Magnetic Resonance in Medicine* 36(6): 923-931.

Edwards D. 2000. Introduction to graphical modeling, 2nd edn. New York: Springer.

Eichler M. 2005. A graphical approach for evaluating effective connectivity in neural systems. *Philosophical Transactions of the Royal Society London B Biological Sciences* 360(1457): 953-67.

Elbert T, Ray WJ, Kowalik ZJ, Skinner JE, Graf KE, Birbaumer N. 1994. Chaos and physiology: deterministic chaos in excitable cell assemblies. *Physiological Reviews* 74:1-47.

Elbert T, Rockstroh B, Kowalik ZJ, Hoke M, Molnar M, Skinner JE, Birbaumer N. 1995. Chaotic brain activity. *EEG Supplement* 44: 441-449.

Elwell CE, Springett R, Hillman E, Delpy DT. 1999. Oscillations in cerebral hemodynamics: Implications for functional activation studies. *Advances in Experimental Medicine and Biology* 471: 57-65.

Evans AC, Collins DL, Mills SR, Brown ED, Kelly RL, Peters TM. 1993. 3D statistical neuroanatomical models from 305 MRI volumes. *Proceedings of the IEEE-Nuclear Science Symposium and Medical Imaging Conference* 1813-1817.

Fallani FDV, Astolfi L, Cincotti F, Mattia D, Marciani MG, Salinari S, Lopez GZ, Kurths G, Zhou C, Gao S, Colosimo A, Babiloni F. 2006. Brain connectivity structure in spinal cord injured: evaluation by graph analysis. *Proceedings of 28th Annual International Conference of IEEE EMBS*: 988-991.

Fiset P, Paus T, Daloze T, Plourde G, Meuret P, Bonhomme V, Hajj-Ali N, Backman SB and Evans AC. 1999. Brain mechanisms of propofol-induced loss of consciousness in humans: a positron emission tomographic study. *Journal of Neuroscience* 19:5506–5513.

Fitzgerald M. 1996. *Registration and estimation of functional magnetic resonance images*. Carnegie Mellon University: Pittsburgh.

Fojt J, Holcik J. 1998. Applying nonlinear dynamics to ECG signal processing. *IEEE Engineering in Medicine and Biology* 17**:** 96-101.

Freeman WJ. 1989. Analysis of strange attractors in EEGs with kinesthetic experience and 4-D computer graphics. In *Brain dynamics* (Basar E & Bullock TH (Eds.)) pp. 512-520. Springer-Verlag: Berlin.

Freeman WJ. 1994. Role of chaotic dynamics in neural plasticity. *Progressive Brain Research* 102:319-33.

Friston KJ, Frith CD, Liddle PF, Frackowiak RSJ. 1993. Functional connectivity - the principal-component analysis of large (PET) data sets. *Journal of Cerebral Blood Flow Metabolism* 13(1): 5-14.

Friston KJ, Holmes AP, Worsley KJ, Poline JP, Frith CD, Frackowiak RSJ. 1995. Statistical parametric maps in functional images: A general linear approach. *Human Brain Mapping* 2:189-210.

Friston KJ, Josephs O, Rees G, Turner R. 1998. Nonlinear event-related responses in fMRI. *Magnetic Resonance in Medicine* 39(1):41-52.

Friston KJ, Buchel C. 2000. Attentional modulation of effective connectivity from V2 to V5/MT in humans. *Proceedings of National Academy of Sciences USA* 13: 7591-7596.

Friston KJ. 2002. Bayesian estimation of dynamical systems: an application to fMRI. *NeuroImage* 16(2):513-30.

Friston KJ, Harrison L, Penny W. 2003. Dynamic causal modeling. *NeuroImage* 19, 1273–1302.

Galinkin JL, Janiszewski D, Young CJ, Klafta JM, Klock PA, Coalson DW, Apfelbaum JL, Zacny JP. 1997. Subjective, psychomotor, cognitive, and analgesic effects of subanesthetic concentrations of sevoflurane and nitrous oxide. *Anesthesiology* 87:1082–1088.

Gautama T, Mandic DP, Van Hulle MM. 2004. A novel method for determining the nature of time series. *IEEE Transactions on Biomedical Engineering* 51(5):728-36.

Giller CA, Hatab MR, Giller AM. 1999. Oscillations in cerebral blood flow detected with a transcranial Doppler index. *Journal of Cerebral Blood Flow Metabolism* 19: 452-459.

Goldberger AL, Rigney DR, West BJ. 1990. Chaos and fractals in human physiology. *Scientific American* 262:42-49.

González RC, Ørstavik S, Stark J. 2000. Quasidiagonal approach to the estimation of Lyapunov spectra for spatiotemporal systems from multivariate time series. *Physical Review E* 62(5): 6429:6439.

Gordon AM, Lee JH, Flament D, Ugurbil K, Ebner TJ. 1998. Functional magnetic resonance imaging of motor, sensory, and posterior parietal cortical areas during performance of sequential typing movements. *Experimental Brain Research* 121: 153-166.

Granger CWJ. 1969. Investigating causal relations by econometric models and cross-spectral methods. *Econometrica* 37(3): 424-438.

Grassberger P, Procaccia I. Characterization of strange attractors. 1983. *Physical Review Letters* 50: 346-349.

Greicius MD, Srivastava G, Reiss AL, Menon V. 2004. Default-mode activity distinguishes Alzheimer's disease from healthy aging: Evidence from functional MRI. *Proceedings of National Academy of Sciences USA* 101(13): 4637:4642.

Guzzetti S, Signorini MG, Cogliati C, Mezzetti S, Porta A, Cerutti S, Malliani A. 1996. Non-linear dynamics and chaotic indices in heart rate variability of normal subjects and heart-transplanted patients. *Cardiovascular Research* 31: 441-446.

Hajnal JV, Myers R, Oatridge A, Schwieso JE, Young IR, Bydder GM. 1994. Artifacts due to stimulus correlated motion in functional imaging of the brain. *Magnetic Resonance in Medicine* 31(3): 283-291.

Hampson M, Peterson BS, Skudlarski P, Gatenby JC, Gore JC. 2002. Detection of functional connectivity using temporal correlations in MR images. *Human Brain Mapping* 15(4): 247-262.

Handwerker DA, Ollinger JM, D'Esposito M. 2004. Variation of BOLD hemodynamic responses across subjects and brain regions and their effects on statistical analyses. *NeuroImage* 21: 1639–1651.

Hansen LK, Nielson FA, Strother SC, Lange N. 2001. Consensus inference in neuroimaging. *NeuroImage* 13: 1212–1218.

Harrington DL, Haaland KY. 1998. Temporal processing in the basal ganglia. *Neuropsychology* 12: 3-12.

Harrison L, Penny WD and Friston K. 2003. Multivariate autoregressive modeling of fMRI time series. *NeuroImage* 19(4):1477-91.

He Y, Zang YF, Jiang TZ, Liang M, Gong GL. 2004: Detecting functional connectivity of the cerebellum using low frequency fluctuations (LFFs). *Lecture Notes in Computer Science* 3217: 907-915.

Hebb DO. 1949. *The organization of behavior*. Wiley: New York.

Hoyer D, Kaplan D, Friedrich S, Eiselt M. 1998a. Determinism in bivariate cardiorespiratory phase-space sets. *IEEE Engineering in Medicine and Biology* 17: 26-31.

Hoyer D, Bauer R, Walter B, Zwiener U. 1998b. Estimation of nonlinear couplings on the basis of complexity and predictability- A new method applied to cardiorespiratory coordination. *IEEE Transactions on Biomedical Engineering* 45(5): 545-552.

Hu X, Le TH, Parrish T, Erhard P. 1995. Retrospective estimation and correction of physiological fluctuation in functional MRI. *Magnetic Resonance in Medicine* 34(2): 201-212.

Hudetz AG, Biswal BB, Shen H, Lauer KK, Kampine JP. 1998. Spontaneous fluctuations in cerebral oxygen supply. *Advances in Experimental Medicine and Biology* 454: 551-559.

Ibrahim AE, Taraday JK, Kharasch ED. 2001. Bispectral index monitoring during sedation with sevoflurane, midazolam, and propofol. *Anesthesiology* 95:1151–1159.

Ivry RB, Keele SW. 1989. Timing functions of the cerebellum. *Journal of Cognitive Neuroscience* 1: 136-152.

Jarque CM, Bera AK 1980. Efficient tests for normality, homoscedasticity and serial independence of regression residuals. *Economic Letters* 6, 255-259.

John ER. 2001. A field theory of consciousness. *Consciousness and Cognition* 10:184–213.

Jones EG. 1999. Making brain connections: neuroanatomy and the work of TPS Powell, 1923-1996. *Annual Review of Neuroscience* 22: 49-103.

Kaminski M, Ding M, Truccolo W, Bressler S. 2001. Evaluating causal relations in neural systems: Granger causality, directed transfer function and statistical assessment of significance. *Biological Cybernetics* 85:145-157.

Kaneko K. 1984. Period-doubling of Kink-antikink Patterns, Quasi-periodicity in Antiferro-like Structures and Spatial Intermittency in Coupled Map Lattices - toward a prelude to a "Field Theory of Chaos". *Progress of Theoretical Physics* 72: 480-486.

Kantz H. and Schreiber T. 1997. *Nonlinear time series analysis*. Cambridge university press, Cambridge, UK.

Kaplan D. 1994. Exceptional events as evidence for determinism. *Physica D* 73: 38-48.

Katok A and Hasselblatt B. 1996. *Introduction to the modern theory of dynamical systems*. Cambridge university press, UK.

Kendall M, Gibbons J. 1990. *Rank correlation methods*. Oxford University Press.

Kennel MB, Brown R, Abarbanel HDI. 1992. Determining minimum embedding dimension using a geometrical construction. *Physical Review A* 45**:** 3403-3411.

Kiviniemi VJ, Haanpaa H, Kantola JH, Jauhiainen J, Vainionpaa V, Alahuhta S, Tervonen O. 2005. Midazolam sedation increases fluctuation and synchrony of the resting brain BOLD signal. *Magnetic Resonance Imaging* 23(4): 531-537.

Kobayashi M, Musha T. 1982. 1/f fluctuation of heartbeat period. *IEEE Transactions on Biomedical Engineering* 29: 456-457.

Kriegeskorte N, Goebel R, Bandettini P. 2006. Information-based functional brain mapping. *Proceedings of National Academy of Sciences USA* 103(10): 3863–3868.

Kruger G, Glover GH. 2001. Physiological noise in oxygenation-sensitive magnetic resonance imaging. *Magnetic Resonance in Medicine* 46: 631-637.

Kruggel F, Zysset S, von Cramon DY. 2000. Nonlinear regression of functional MRI data: an item recognition task study. *NeuroImage* 12(2):173-83.

Kus R, Kaminski M, Blinowska KJ. 2004. Determination of EEG activity propagation: pair-wise versus multichannel estimate. *IEEE Transactions on Biomedical Engineering* 51(9): 1501-1510.

Kwong KK, Belliveau JW, Chesler DA, Goldberg IE, Weisskoff RM, Poncelet BP, Kennedy DN, Hoppel BE, Cohen MS, Turner R, Cheng HM, Brady TJ, Rosen BR. 1992. Dynamic magnetic resonance imaging of human brain activity during primary sensory stimulation. *Proceedings of National Academy of Sciences USA* 89: 5675-5679.

LaConte S, Ngan S, Zhuang J, Heberlein K, Peltier S, Hu X. 2003. Evidence for nonlinear dynamical determinism related to functional connectivity in fMRI baseline time series. *Proceedings of ISMRM* 11:1178.

LaConte S, Peltier S, Kadah Y, Ngan S, Deshpande G, Hu X. 2004. Detecting nonlinear dynamics of functional connectivity. *Proceedings of SPIE International Symposium on Medical Imaging, San Diego* 5369: 227-237.

Lauzon ML, Rutt BK. 1993. Generalized K-space analysis and correction of motion effects in MR-Imaging. *Magnetic Resonance in Medicine* 30(4): 438-446.

Lee YJ, Zhu YS, Xu YH, Shen MF, Tong SB, Thakor NV. 2001. The nonlinear dynamical analysis of the EEG in schizophrenia with temporal and spatial embedding dimension. *Journal of Medical Engineering and Technology* 25(2): 79-83.

Li SJ, Biswal B, Li Z, Risinger R, Rainey C, Cho JK, Salmeron BJ, Stein EA. 2000. Cocaine administration decreases functional connectivity in human primary visual and motor cortex as detected by functional MRI. *Magnetic Resonance in Medicine* 43(1): 45-51.

Li SJ, Li Z, Wu GH, Zhang MJ, Franczak M, Antuono PG. 2002. Alzheimer disease: Evaluation of a functional MR imaging index as a marker. *Radiology* 225(1): 253-259.

Li ZH, Sun XW, Wang ZX, Zhang XC, Zhang DR, He S, Hu X. 2004. Behavioral and functional MRI study of attention shift in human verbal working memory. *NeuroImage* 21(1): 181-191.

Liu JZ, Zhang LD, Yao B, Yue GH. 2002. Accessory hardware for neuromuscular measurements during functional MRI experiments. *Magnetic Resonance Materials in Physics Biology and Medicine* 13: 164-171.

Liu JZ, Huang HB, Sahgal V, Hu XP, Yue GH. 2005. Deterioration of cortical functional connectivity due to muscle fatigue. *Proceedings of ISMRM* 13: 2679.

Lowe MJ, Mock BJ and Sorenson JA. 1998. Functional connectivity in single and multislice echoplanar imaging using resting-state fluctuations. *NeuroImage* 7(2): 119-132.

Lowe MJ, Phillips MD, Lurito JT, Mattson D, Dzemidzic M, Mathews VP. 2002. Multiple sclerosis: Low-frequency temporal blood oxygen level-dependent fluctuations indicate reduced functional connectivity - Initial results. *Radiology* 224(1): 184-192.

Maas LC, Frederick BD and Renshaw PF. 1997. Decoupled automated rotational and translational registration for functional MRI time series data: The DART registration algorithm. *Magnetic Resonance in Medicine* 37(1): 131-139.

Mashour GA. 2004. Consciousness unbound: toward a paradigm of general anesthesia. *Anesthesiology* 100:428–433.

McIntosh AR and Gonzalez-Lima F. 1994. Structural equation modeling and its application to network analysis in functional brain imaging. *Human Brain Mapping* 2: 2-22.

McIntosh AR, Kotter R. 2006. Assessing computational structure in functionally defined brain networks. 12th annual meeting of Human Brain Mapping, Florence, Italy, 2006. Reference in *NeuroImage* 31 (S72): 175.

McKeown MJ, Sejnowski TJ. 1998. Independent component analysis of fMRI data: examining the assumptions. *Human Brain Mapping* 6: 160-188.

Mees AI, Rapp PE, Jennings LS. 1987. Singular value decomposition and embedding dimension. *Physical Review A* 37: 340-346.

Morgan VL, Price RR. 2004. The effect of sensorimotor activation on functional connectivity mapping with MRI. *Journal of Magnetic Resonance Imaging* 22: 1069-1075.

Mugler J, Brookeman J. 1990. Three-dimensional magnetization-prepared rapid gradient-echo imaging (3D MP RAGE). *Magnetic Resonance in Medicine* 15:152-7.

Narayanan K, Govindan RB and Gopinathan MS. 1998. Unstable periodic orbits in human cardiac rhythms. *Physical Review E* 57: 4594-4603.

Obrig H, Neufang M, Wenzel R, Kohl M, Steinbrink J, Einhaupl K, Villringer A. 2000. Spontaneous low frequency oscillations of cerebral hemodynamics and metabolism in human adults. *NeuroImage* 12: 623-639.

Ogawa S, Tank DW, Menon R, Ellerman JM, Kim SG, Merkle H, Ugurbil K. 1992. Intrinsic signal changes accompanying sensory stimulation: Functional brain mapping with magnetic resonance imaging. *Proceedings of National Academy of Sciences USA* 89: 5675-5679.

Passingham RE. 1988. Premotor cortex and preparation for movement. *Experimental Brain Research* 70: 590-596.

Peltier SJ, Noll DC. 2002. T_2^* dependency of low frequency functional connectivity. *NeuroImage* 16: 985-992.

Peltier SJ, Polk TA, Noll DC. 2003. Detecting low-frequency functional connectivity in fMRI using a self-organizing map (SOM) algorithm. *Human Brain Mapping* 20(4): 220-226.

Peltier SJ, Kerssens C, Hamann SB, Sebel PS, Byas-Smith M, Hu X. 2005. Functional connectivity changes with concentration of sevofurane anesthesia. *NeuroReport* 16(3): 285:288.

Peltier SJ, Laconte SM, Niyazov DM, Liu JZ, Sahgal V, Yue GH, Hu XP (2005a): Reductions in interhemispheric motor cortex functional connectivity after muscle fatigue. *Brain Research* 1057: 10-16.

Peltier SJ, Kerssens C, Hamann SB, Sebel PS, Byas-Smith M, Hu X. 2006. Default mode functional connectivity altered by sevoflurane anesthesia. *Proceedings of ISMRM* 14: 3260.

Pezard L., Lachaux J.P., Thomasson N. and Martinerie J. 1999. Why bother to spatially embed EEG? *Psychophysiology* 36(4): 527:531.

Poggi P. and Ruffo L. 1997. Exact solutions in the FPU oscillator chain. *Physica D* 103: 251-272.

Por LT, Puthusserypady S. 2005. Postprocessing methods for finding the embedding dimension of chaotic time series. *Physical Review E* 72: 027204.

Pritchard WS, Duke DW. 1992. Measuring chaos in the brain: A tutorial review of nonlinear dynamical EEG analysis. *International Journal of Neuroscience* 67: 31-80.

Pritchard WS, Krieble KK, Duke D.W. 1996. On the validity of estimating EEG correlation dimension using spatial embedding. *Psychophysiology* 33(4): 362:368.

Pritchard WS. 1999. On the validity of spatial embedding. *Psychophysiology* 36(4): 532:535.

Quigley M, Cordes D, Wendt G, Turski P, Moritz C, Haughton V, Meyerand ME. 2001. Effect of focal and nonfocal cerebral lesions on functional connectivity studied with MR imaging. *American Journal of Neuroradiology* 22(2): 294-300.

Raichle ME, MacLeod AM, Snyder AZ, Powers WJ, Gusnard DA, Shulman GL. 2001. A default mode of brain function. *Proceedings of National Academy of Sciences USA* 98(2): 676-682.

Ries CR, Puil E. 1999. Mechanism of anesthesia revealed by shunting actions of isoflurane on thalamocortical neurons. *Journal of Neurophysiology* 81:1795–1801.

Roebroeck A, Formisano E, Goebel R. 2005. Mapping directed influence over the brain using Granger causality and fMRI. *NeuroImage* 25: 230– 242.

Rombouts SARB, Stam CJ, Kuijer JPA, Scheltens P, Barkhof F. 2003. Identifying confounds to increase specificity during a "no task condition" - Evidence for hippocampal connectivity using fMR1. *NeuroImage* 20(2): 1236-1245.

Rorden C, Brett M. 2000. Stereotaxic display of brain lesions. *Behavioural Neurology* 12, 191-200.

Sakkalis V, Oikonomou T, Pachou E, Tollis I, Micheloyannis S, Zervakis M. 2006. Time-significant wavelet coherence for the evaluation of schizophrenic brain activity using a graph theory approach. *Proceedings of 28th Annual International Conference of IEEE EMBS*: 4265-4268.

Schiff SJ, Jerger K, Duong DH, Chang T, Spano ML, Ditto WL. 1994. Controlling chaos in the brain. *Nature* 370: 615-20.

Sheth SA, Nemoto M, Guiou M, Walker M, Pouratian N, Toga AW. 2004. Linear and nonlinear relationships between neuronal activity, oxygen metabolism, and hemodynamic responses. *Neuron* 42(2):347-55.

Silva AC, Koretsky AP. 2002. Laminar specificity of functional MRI onset times during somatosensory stimulation in rat. *Proceedings of National Academy of Sciences USA* 99: 15182–15187.

Skiena S. 1990. *Implementing discrete mathematics: combinatorics and graph theory with mathematica*. Reading, MA: Addison-Wesley.

Solodkin A, Hlustik P, Chen EE, Small SL. 2004. Fine modulation in network activation during motor execution and motor imagery. *Cerebral Cortex* 14: 1246-1255.

Sprott JC. *Chaos and time series analysis*. 2003. Oxford University Press.

Stam CJ. 2004. Functional connectivity patterns of human magnetoencephalographic recordings: a 'small-world' network? *Neuroscience Letters* 355: 25-28.

Stewart HB. 1996. Chaos, dynamical structure and climate variability. In *Chaos and the changing nature of science and medicine- An introduction* (Eds: Herbert D),

Conference proceedings, **376**: 80-115. American Institute of Physics: Woodbury, New York.

Strick PL, Hoover JE. 1999. The organization of cerebellar and basal ganglia outputs to primary motor cortex as revealed by retrograde transneuronal transport of herpes simplex virus type 1. *Journal of Neuroscience* 19: 1446-1463.

Strother SC, Anderson JR, Schaper KA, Sidtis JJ, Liow JS, Woods RP, Rottenberg DA. 1995. Principal component analysis and the scaled sub-profile model compared to inter-subject averaging and statistical parametric mapping. I. "Functional connectivity" of the human motor cortex studied with [^{15}O] water PET. *Journal of Cerebral Blood Flow Metabolism* 15: 738-753.

Strother SC, Lange N, Anderson JR, Schaper KA, Rehm K, Hansen LK, Rottenberg DA. 1997. Activation pattern reproducibility: Measuring the effects of group size and data analysis models. *Human Brain Mapping* 5: 312-316.

Tabor M, Weiss J. 1981. Analytic structure of the Lorenz system. *Physical Review A* 24: 2157-2167.

Takens F. 1980. Detecting strange attractors in turbulence. In *Dynamical Systems and Turbulence* (Eds: Rand D and Young L) 898: 366-381, Springer-Verlag, Berlin.

Tanji J. 1996. The supplementary motor area in the cerebral cortex. *Neuroscience Research* 19: 251-268.

Theiler J. 1987. Efficient algorithm for estimating the correlation dimension from a set of discrete points. *Physical Review A* 36(9): 4456-4462.

Theiler J, Eubank S, Longtin A, Galdrikian B, Farmer D. 1992. Testing for nonlinearity in time series: The method of surrogate data. *Physica D* 58: 77–94.

Tononi G, Edelman GM. 1998. Consciousness and the integration of information. In Jasper HH, Descarries L, Costelucci VC, Rossignol S (Eds.), *Advances in Neurology* 77: 245–280. Philadelphia: Lippincott–Raven.

Tsonis AA. 1992. *Chaos- From theory to applications*. Plenum Press: New York.

Vazquez AL, Douglas CN. 1998. Nonlinear aspects of the BOLD response in Functional MRI. *NeuroImage* 7: 108-118.

Veselis RA. 2001. Anesthesia – a descent or a jump into depths. *Consciousness and Cognition* 10:230–235.

Veselis RA, Reinsel RA, Feshchenko VA, Dnistrian AM. 2002. A neuroanatomical construct for the amnesic effects of propofol. *Anesthesiology* 97:329–337.

Watts DJ, Strogatz SH. 1998. Collective dynamics of 'small-world' networks. *Nature* 393: 440-442.

White NS, Alkire MT. 2003. Impaired thalamocortical connectivity in humans during general-anesthetic-induced unconsciousness. *NeuroImage* 19:402–411.

Wiener N. 1956. Chapter 8. In *Modern Mathematics for Engineers* (Ed: Beckenbach EF), McGraw–Hill, New York.

Wilcoxon F. 1945. Individual Comparisons by Ranking Methods. *Biometrics* 1: 80-83.

Woods RP, Grafton ST, Holmes CJ, Cherry SR, Mazziotta JC. 1998. Automated image registration: I. General methods and intrasubject, intramodality validation. *Journal of Computer Assisted Tomography* 22(1): 139-152.

Woods RP, Grafton ST, Watson JDG, Sicotte NL, Mazziotta JC. 1998. Automated image registration: II. Intersubject validation of linear and nonlinear models. *Journal of Computer Assisted Tomography* 22(1): 153-165.

Yousry TA, Schmid U, Alkadhi H, Schmidt D, Peraud A, Buettner A, Winkler P. 1997. Localization of the motor hand area to a knob on the precentral gyrus. *Brain* 120: 141– 157.

Zang Y, Jiang T, Lu Y, He Y, Tian L. 2004. Regional homogeneity approach to fMRI data analysis. *NeuroImage* 22: 394-400.

Zhang XS, Zhu YS, Thakor NV, Wang ZZ. 1999. Detecting ventricular tachycardia and fibrillation by complexity measure. *IEEE Transactions on Biomedical Engineering* 46(5): 548-555.

Zhuang J, LaConte SM, Peltier SJ, Zhang K, Hu XP. 2005. Connectivity exploration with structural equation modeling: an fMRI study of bimanual motor coordination. *NeuroImage* 25(2): 462-470.